Technical Report

Project Definition Study of the Use of Assets and Facilities of the Superconducting Super Collider Laboratory

Measurement of the Magnetically-Induced QED Birefringence of theVacuum and An Improved Search for Laboratory Axions

Siu Au Lee, William M. Fairbank, Jr. and Walter H. Toki
Department of Physics, Colorado State University
Fort Collins, Colorado 80523

John L. Hall
Joint Institute for Laboratory Astrophysics
University of Colorado and The National Institute of Standards and Technology,
Boulder, Colorado 80309

Philip F. Kraushaar, Jr. and Tariq S. Jaffery
Superconducting Super Collider Laboratory
Waxahachie, Texas 75165

Submitted to the
U. S. Department of Energy
under Grant # DE-FG05-94ER40880

October 31, 1994

DISCLAIMER

Portions of this document may be illegible in electronic image products. Images are produced from the best available original document.

Measurement of the Magnetically-Induced QED Birefringence of the Vacuum and An Improved Search for Laboratory Axions

Executive Summary

The Colorado State Collaboration has studied the feasibility of a high sensitivity QED birefringence/axion search measurement. The objective of this work is to measure, for the first time, the birefringence induced in the vacuum on a light beam travelling in a powerful magnetic field. The same experimental setup also allows a highly sensitive search for axion or axion-like particles. The experiment would combine custom-designed optical heterodyne interferometry with a string of six SSC prototype superconducting dipole magnets at the N-15 site of the SSC Laboratory. With these powerful laser tools, sensitivity advances of 10^7 to 10^9 over previous optical experiments will be possible. The proposed experiment will be able to measure the QED light-by-light scattering effect with a 0.5 % accuracy. The increased sensitivity for the axion-two photon interaction will result in a bound on this process rivalling the results based on astrophysical arguments.

In the technical report we address the scientific significance of these experiments and examine the limiting technical parameters which control their feasibility. The proposed optical/electronic scheme is presented in the context of a background of the known and projected systematic problems which will confront any serious attempt to make such measurements. Notable challenges arise in the areas of seismic vibration isolation, and the reduction of spurious signals due to background gas contamination and mirror heating. Many delicate choices also must be made for this apparatus to deliver successfully a sensitivity in measuring the change in the index of refraction at the 7×10^{-25} level, a domain which the gravitational wave detector groups regard as probable but not guaranteed. The fundamental advantage of our configuration is that our experiment can be configured to be of differential character, in several aspects, thus elegantly suppressing unwanted sensitivities and noise.

We discuss a five year experimental program, with an initial research phase of two years duration, during which a 3 m test interferometer and large vacuum optical chambers will be

completed and used for testing. Questions to be addressed during this research phase include: investigation of laser power effect on birefringence of mirrors, development of anti-seismic active suspension mirror control system, demonstration of laser locking of sufficient range and accuracy, development of the laser beam-steering and mirror automatic alignment system, configuration of the magnet string and confirmation of viable magnet ramp rates, beam tube vacuum, and investigation of the light scattering problems associated with the rather small bore of the present magnet design. In year 3 the long optical interferometer will be installed on the magnet string. The performance of the laser beam pointing control system for the long interferometer will also be confirmed. Initial experiments on the QED effect will take place in year 4. In the final year precision measurement of the QED effect will be performed and, in the process, an axion search will be conducted.

Fiscally, this project will be run in as small and cost effective operation as possible to enhance efficiency and reduce unnecessary costs. Our report discusses several options and develops approximate budgets under several different siting and funding scenarios.

TABLE OF CONTENTS

1. INTRODUCTION

This report represents the culmination of a three month feasibility study by the Colorado State Collaboration of combining optical techniques with the string of SSC prototype superconducting dipole magnets located at the N-15 site of the former Superconducting Super-Collider Labortory, for a QED/axion search experiment. The goal of the experiment is to measure, for the first time, the magnetically induced QED birefringence on a beam of light travelling in a strong magnetic field. The same experimental setup also allows a highly sensitive search for axion or axion like particles. The proposed experiment will be able to measure the QED light-by-light scattering effect at the 0.5 % level. The increased sensitivity for the axion-two photon interaction will result in a bound on this process rivalling the results based on astrophysical arguments.

During the study, members of the Collaboration visited the SSCL to evaluate the ASST facility at the N15 site, in regards to its suitability for the proposed experiment. We have also visited SLAC to discuss with theorists about the significance of QED and axion search experiments. We have carried out preliminary experiments to demonstrate the capability of our proposed birefringence measurement scheme. In view of the uncertainties now facing the long-term future of the SSCL after the settlement of DOE with the state of Texas, we have also made informal inquiries and initiated preliminary discussions with FNAL to explore the possibility of performing the experiment at FNAL versus SSCL.

2. REVIEW OF THEORY AND SIGNIFICANCE OF THE EXPERIMENT

2.1 Magnetic Birefringence and Dichroism in Vacuum

When a beam of light travels in vacuum in a strong external magnetic field **B**, the vacuum polarization process of QED induces a small change in the index of refraction of the vacuum. This effect may be interpreted as light-by-light scattering between an optical photon of frequency ω and a zero frequency photon from the magnetic field (Fig. 2.1a). For a light beam traveling in a direction perpendicular to the applied B field and linearly polarized at 45° to **B**, this QED effect leads to a phase retardation of the component of polarization parallel to **B**, and results in a small elliptical polarization of the light beam. The interaction of a polarized light beam with axions can also produce a birefringence in the beam (Fig. 2.1b), as well as a rotation of the polarization (Fig. 2.1c). Thus a precision measurement of the optical birefringence and optical rotation of a laser beam in a strong magnetic field can be used to test QED and to search for axion-like particles.

2.1.1 Magnetic birefringence due to QED

The magnetically induced birefringence due to the dominant QED light by light scattering term has been calculated more than twenty years ago[1], and is expected to be observed and measured for the first time in the proposed experiment. The result is [1,2]

$$n_{/\!/}-n_{\perp}=2\frac{\alpha^2B^2}{15m_e^4} \qquad (2.1)$$

where m_e is the electron mass, and $n_{\parallel}$ and $n_{\perp}$ are the indices of refraction for light polarized parallel and perpendicular to the magnetic field. The corresponding induced ellipticity is

$$\psi_{QED}=\frac{(n_{/\!/}-n_{\perp})\,kNl}{2}=N\frac{\alpha^2B^2\omega l}{15m_e^4} \qquad (2.2)$$

where N is the number of passes through the magnetic field, k and ω are the wave vector and angular frequency of the light, and l is the length of the magnetic field region. It is quite obvious that in order to observe ψ_{QED}, the path length l, the number of passes N and the B field should all be as large as possible. The natural Lorentz-Heavyside units (h = c = 1, fine structure constant $\alpha = e^2/4\pi = 1/137$) are used in all the equations in this chapter of the report. In these units a magnetic field of 1 T can be expressed as 195 eV^2 and a length of 1 m as 5.07×10^6 eV^{-1}.

For the conditions of the proposed experiment, $N = 8.88\times10^4$, $B_{eff}^2 = 35$ T^2, $l = 90$ m, and $\omega = 2.33$ eV, Eq. (2.1) and (2.2) give $n_{\parallel}-n_{\perp}=1.4\times10^{-22}$ and $\psi_{QED}= 6.5\times10^{-9}$ rad. The expected sensitivity of the proposed experiment is at or near the shot noise limit for a six hour measurement, $\Delta n_{shot}= 7\times10^{-25}$ and $\psi_{shot}=3.3\times10^{-11}$ rad (see section 3.7). These shot noise limits are 0.5% of the predicted QED effect. Thus a test of QED to the level $\sim\alpha/\pi$, where the next higher order corrections are expected, is anticipated.

2.1.2 Magnetic birefringence and rotation due to photon-axion coupling

The theory of the coherent interaction of photons in a light beam with a strong external magnetic field **B** and low-mass bosons (such as the axion) or leptons has been given by Raffelt and Stodolsky [3]. For brevity, the word "axion" is used loosely in this report to describe all axion-like pseudoscalar particles, and these ideas should be understood to apply more generally. The dominant Feynman diagrams are shown in Fig. 2.1. The Primakoff production term (Fig. 2.1b) leads to a small absorption in the component of the electric field of light parallel to **B**. This may be observed experimentally as a small rotation of the plane of polarization of the light beam. This process occurs only for axion masses m_a less than the photon energy. The virtual axion production process (Fig. 1c) can take place for $m_a > \omega$ or $m_a < \omega$ and leads to a phase retardation rather than an attenuation of the component of polarization parallel to **B**. This effect induces a small elliptical polarization, and hence a birefringence to the light beam. Both effects are maximized if the incident polarization is at 45° to the magnetic field.

For a light beam polarized at 45° to the B field, the magnetically induced rotation and ellipticity due to photon and axion-like particle coupling are [2,3]

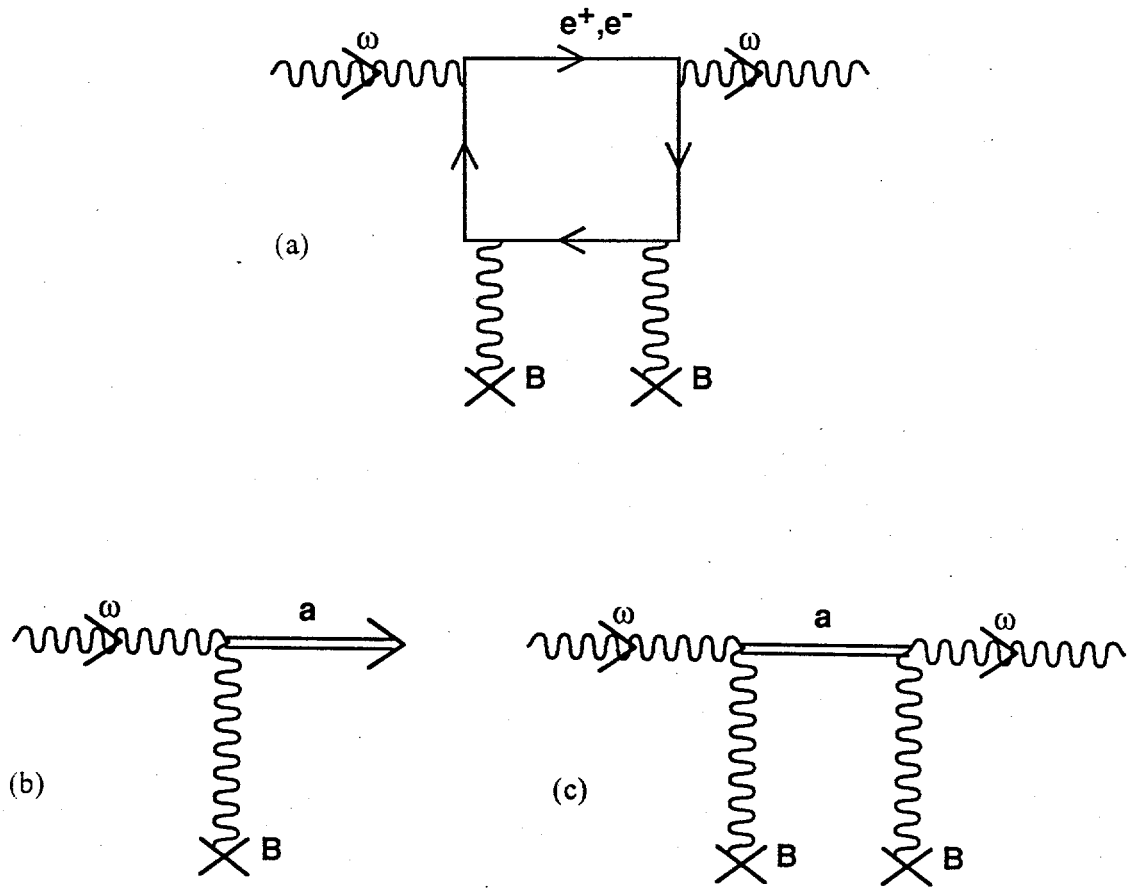

Figure 2.1. Feynman diagrams for (a) QED vacuum polarization or light-by-light scattering producing magnetic birefringence in vacuum and axion-photon coupling leading to (b) magnetic rotation and (c) magnetic birefringence in vacuum.

$$\epsilon_a = N g_{a\gamma\gamma}^2 B^2 \frac{\omega^2}{m_a^4} \sin^2\left(\frac{m_a^2 l}{4\omega}\right), \qquad (2.3)$$

and

$$\psi_a = N g_{a\gamma\gamma}^2 B^2 \frac{\omega^2}{m_a^4} \left[\frac{m_a^2 l}{2\omega} - \sin\left(\frac{m_a^2 l}{2\omega}\right)\right], \qquad (2.4)$$

where $g_{a\gamma\gamma}$ is the axion-photon coupling constant. Both of these effects are linear in N but nonlinear in l because the axions are not reflected with the photons at the mirrors, and because the axion and the photon do not retain exact phase coherence throughout the interaction region since the axion has a mass. Thus it is seen that a longer length l is a substantial advantage at small m_a ($\varepsilon_a \propto l^2$ and $\psi_a \propto l^3$). However, much of the advantage is lost for large m_a ($m_a l/2\omega > \pi$) due to the sine functions in Eqs. (2.3) and (2.4). Note that the axion-induced ellipticity ψ_a can be distinguished from the QED induced ellipticity ψ_{QED} through its different dependence upon l. For representative values of ε_a and ψ_a, consider $g_{a\gamma\gamma} = 2\times10^{-10}$ GeV^{-1}. For $m_a \leq 1\times10^{-4}$ eV, the induced rotation from (2.3) is constant at $\varepsilon_a = 6\times10^{-11}$ rad. From (2.4) we find that ψ_a reaches a maximum value of 8×10^{-11} rad (0.6% of the QED value) at $m_a = 1.7\times10^{-4}$ eV. These values are more than twice the shot noise limits for a 6 hour measurement, $\varepsilon_{shot} = 2.5\times10^{-11}$ rad and $\psi_{shot} = 3.3\times10^{-11}$ rad. Axion-like particles at this level are therefore expected to be detectable.

2.2 Significance of the Proposed Experiments

2.2.1 Test of light-by-light scattering in QED

T. Kinoshita and D. R. Yennie recently summarized the importance of high precision tests of Quantum Electrodynamics. They said, in discussing the relationship of QED to unified field theories, [4]

> "Thus, although QED should ultimately be regarded as a low energy phenomenology to some more fundamental theory, we can in practice often ignore

> that fact and treat QED as a self-contained theory, occasionally incorporating small corrections from the more complete theory, the so-called standard model of electroweak and strong interactions. To the extent that pure QED predictions agree with experiment, the deeper theory has not yet revealed itself in low energy experiments; but it is important to continue to push QED to more and more stringent tests in the expectation that at some point there will appear a genuine conflict between predictions and experiment."

To this end, a number of high precision tests of QED have been made over the last several decades.

The most precise experimental test of QED is the measurement of the anomalous magnetic moment of the electron, $a_e = (g_e-2)/2$. The current experimental accuracy of 4 parts per billion [5] exceeds that of the fine structure constant, α, by an order of magnitude. At the present level of experimental and theoretical accuracy, 6th order diagrams of order $(\alpha/\pi)^3$, including the lowest order light-by-light (LBL) scattering term (Fig. 2a), are tested to the tenths of percent level. Due to the uncertainty in α, 8th order LBL diagrams of order $(\alpha/\pi)^4$ (Fig 2.2b) have not yet been tested, although the experimental accuracy is great enough (Table 2.1).

The anomalous magnetic moment of the muon, $a_\mu = (g_\mu-2)/2$, has been measured to the 10 parts-per-million level [6]. Although the precision is vastly inferior to that for the electron, significant tests of 6th order diagrams, including the LBL term to 4.5%, can be made (Table 2.1). This is because contributions from higher order terms are larger in a_μ than in a_e, due to the larger mass of the muon. The present experimental precision is barely insufficient for a test of 8th order LBL diagrams, but a proposed 30× improvement in the experiment [7] projects an experimental error comparable to the 10th order LBL term (Table 2.1). Of particular interest in those experiments are possibly observable effects or mass limits for "new physics": gauge bosons such as W_R, Z', Higgs, and SUSY particles, muon or gauge boson substructure, and excited leptons. In addition, although not expected, it is always possible that a fundamental breakdown of QED may occur at some level.

Our proposed measurement of ψ_{QED} at the $\leq$0.5% level is an excellent complement to the electron and muon g-2 experiments. The dominant diagram in the magnetic birefringence effect

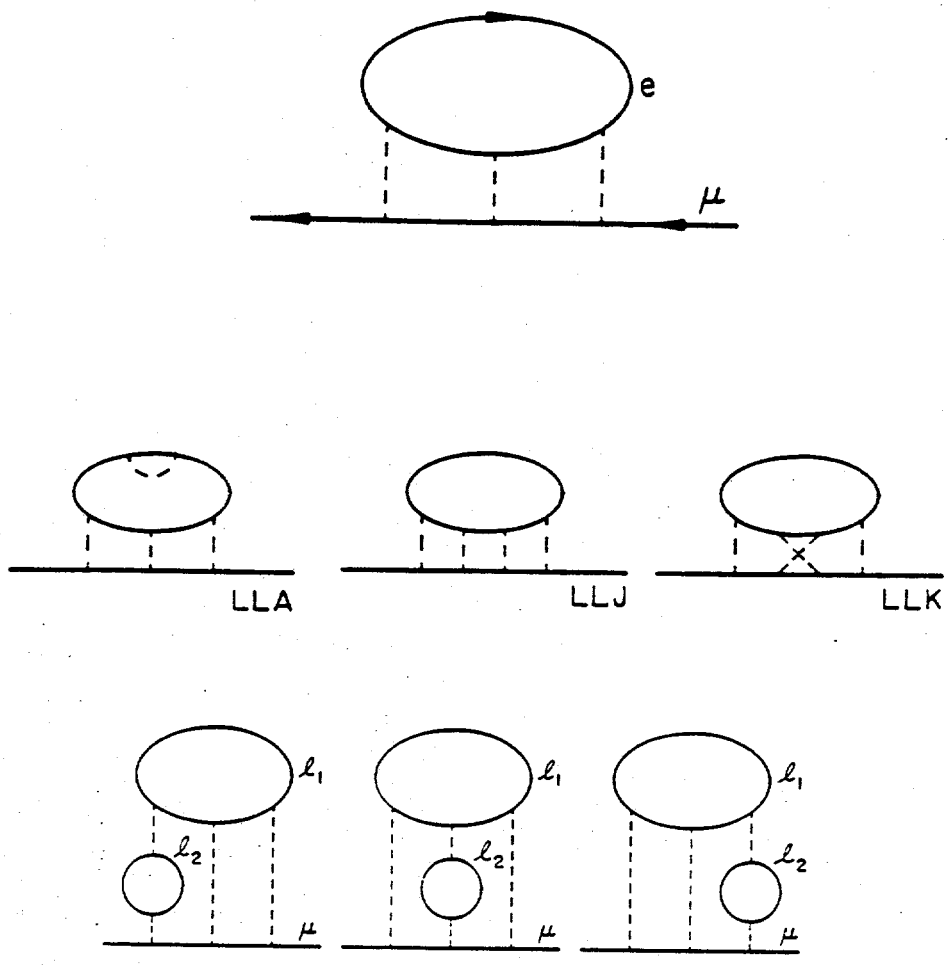

Figure 2.2. Feynman diagrams for (a) sixth and (b) eighth order light-by-light scattering contributions to the electron and muon anomalous magnetic moment.

(Fig. 2.1a) is similar to the 6th order LBL scattering diagram (Fig. 2.2a) which contributes only a small correction to g–2. Thus our experiment provides direct access with comparable precision to LBL terms which are important to know and verify in order to extract "new physics" from g-2 experiments. Although the expected error limit from a six hour measurement (≤0.5%) is just on the level where the next order LBL terms (such as the 8th order g-2 diagrams in Fig. 2.2b) appear, a longer data acquisition period and very careful treatment of systematic effects could conceivably make possible the first experimental test of these diagrams (see Section 7).

Quantity	a_e	a_μ	**Future BNL expt.**
a	1 159 652 188	1 165 926 000	
Δa_{expt}	4.3	12000	400
Δa_{theory}	29 (value of α)	1760 (hadron vac. pol.)	< 400 (better R meas.)
a_{expt}-a_{theory}	48 (29)	4820 (12000)	
6th order LBL	4651 (4)	267 176 (36)	
8th order LBL	-13.8 (4)	3382 (1)	
10th order LBL		570 (140)	
Hadronic LBL		600(40) (quark) 490 (50) (pion)	
$\Delta a / a^{(6)}_{LBL}$	0.6 %	4.5 %	0.15 %
$\Delta a / a^{(8)}_{LBL}$	210 %	350 %	12 %
$\Delta a / a^{(10)}_{LBL}$		2100 %	70 %

Table 2.1. Contributions ($x10^{-12}$) to the anomalous magnetic moment a=(g-2)/2 of the electron and the muon.

The major experiments which test LBL scattering diagrams in QED are summarized in Table 2.2. In addition to the experiments discussed above, Delbrück scattering of MeV photons off the Coulomb electric field of a nucleus (Fig. 2.3a) is another example of a direct LBL

scattering effect which can be measured experimentally. Although often complicated by competing Rayleigh, nuclear and Thompson scattering contributions, a measurement of Delbrück scattering at 2.75 MeV has yielded a test of LBL scattering to 5% [8]. A similar term (Fig. 2.3b) arises as a small correction to the hyperfine structure of muonium. However, the uncertainty in the mass of the muon has precluded a test of this LBL scattering effect [9].

Previous Expt.	**LBL term**	**Expt. Error**	**Error / LBL**
Electron g-2 ($x10^{-12}$)	4637(4)	4.3 (+29 from α)	0.6 %
Muon g-2 ($x10^{-9}$)	271.13(14)	12	4.5 %
Muonium HFS (kHz)	-0.261	0.16 (1.34 from m_μ)	220 %
Delbrück scattering			5 %

Proposed Expt.	**LBL term**	**Expected Error**	**Error / LBL**
Muon g-2 ($x10^{-9}$)	271.13(14)	0.40	0.15 %
This experiment	$6.5x10^{-9}$	$3.0x10^{-11}$	0.5 %

Table 2.2 Summary of previous and proposed experiments which test light-by-light (LBL) diagrams in QED. The column at the right gives the precision to which LBL contributions to the effect are tested. (The largest error limit is used.)

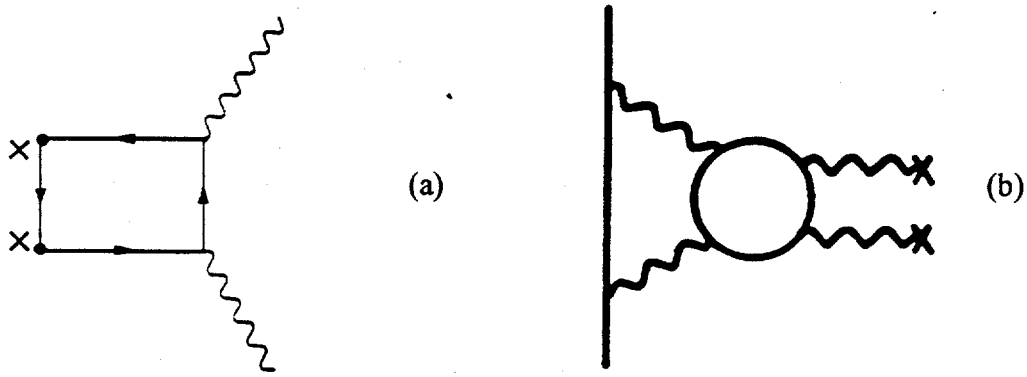

Figure 2.3. Feynman diagrams for (a) Delbrück scattering of a photon off the Coulomb field of a nucleus and (b) the light-by-light scattering diagram for the hyperfine structure of muonium.

Theoretically, our proposed new test of light-by-light scattering is also interesting because the theoretical method used to evaluate LBL diagrams leading to magnetic birefringence is very different from that used for g-2 calculations. In the proposed experiment, the predicted effect (2.1) is derived analytically using the effective Euler-Heisenberg Lagrangian of vacuum polarizability [10]. In contrast, only numerical solutions have been achieved for the light-by-light terms in g-2 [5,6].

2.2.2 Search for Axions and Axion-like Particles

Axions are light, weakly interacting scalar or pseudoscalar bosons which were hypothesized by Peccei and Quinn [11] to solve the strong CP problem. Various types of axions have been proposed, these include hadronic axions, such as the Kim-Shifman-Vainshtein-Zakharov (KSVZ) axions [12], which couple only to quarks, and Dine-Fischler-Srednicki-Zhitnitsky (DFSZ) axions [13], which couple to fermions. In the standard GUT model and also for DFSZ axions, the axion mass, m_a, and its coupling constant to two photons, $g_{a\gamma\gamma}$, have a specific relation [14]:

$$m_a \text{ (eV)} \approx 7\text{x}10^9 \, g_{a\gamma\gamma} \text{ (GeV}^{-1}\text{)} \qquad (2.5)$$

For hadronic axions, the relationship is the same, except the proportionality constant is $2.7\text{x}10^9$ [14]. Although theoretical interest [15] at present centers primarily on axions near the GUT line specified by Eq. (2.5) on a $g_{a\gamma\gamma}$ vs. m_a plot, it is important to investigate experimentally as large a region of the $g_{a\gamma\gamma}$ vs. m_a phase space as possible in order to exclude or find axion-like particles which may or may not have been theorized to date.

The proposed experiment is projected to be able to measure, at the shot noise level in a 6 hour measurement period, optical rotation and birefringence as low as $\varepsilon_{min}=2.5\text{x}10^{-11}$ rad and $\psi_{min}=3\text{x}10^{-11}$ rad respectively. These values of experimental sensitivity correspond to the expected limits for $g_{a\gamma\gamma}$ which are plotted in Fig. 2.4. For $m_a < 10^{-4}$ eV the limit from the optical rotation experiment is constant at $g_{a\gamma\gamma} = 1.3\text{x}10^{-10}$ GeV^{-1}. For the optical birefringence experiment the projected limit reaches this same value for $m_a=1.8\text{x}10^{-4}$ eV, and

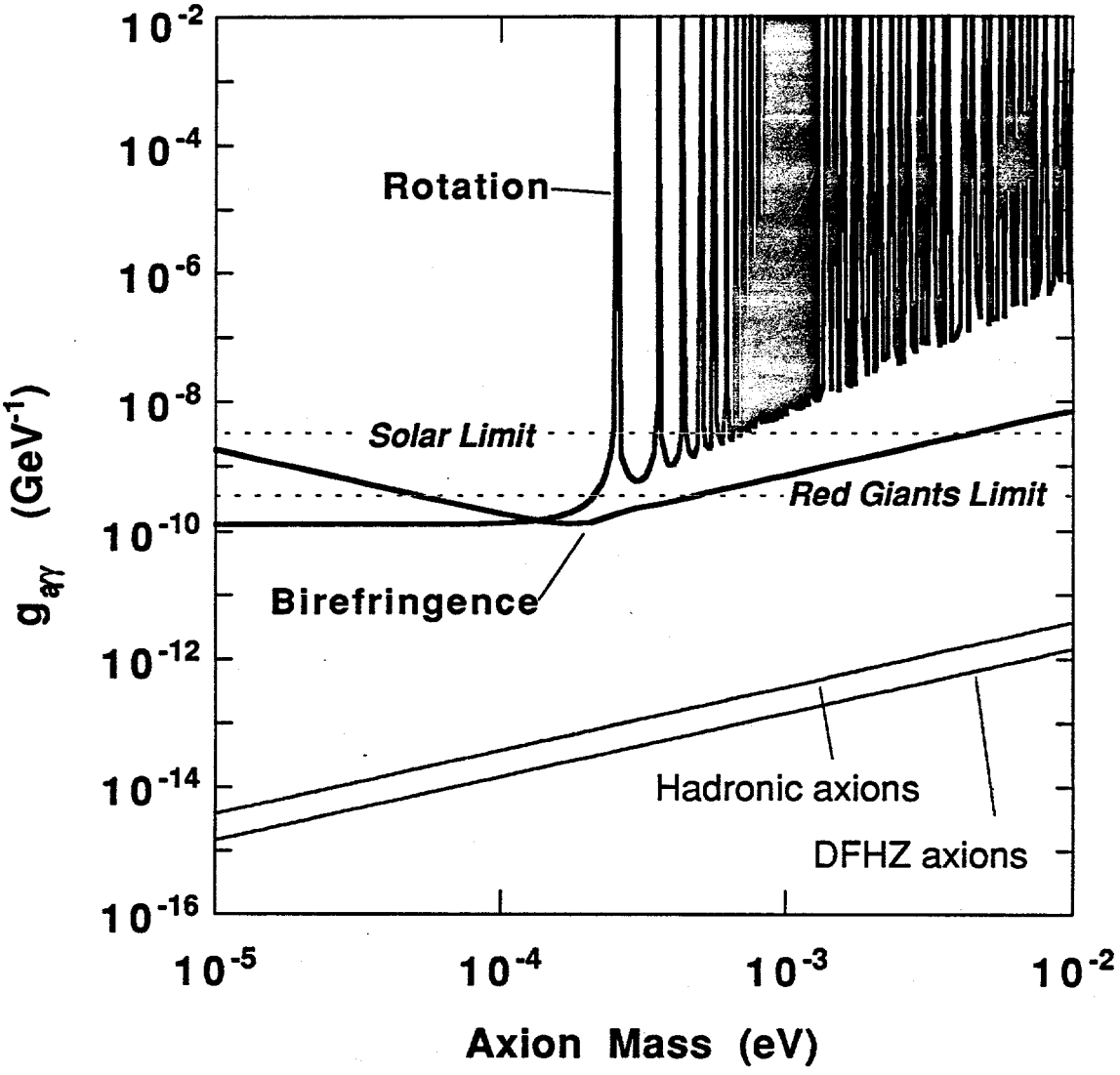

Figure 2.4 The limit on axion mass and axion-two-photon coupling expected in the proposed experiment. For reference, two comparable limits from astrophysical analyses are also presented.

becomes less sensitive on both sides of this mass. Clearly, the present experiment will not reach the GUT lines representing DFSZ and hadronic axions. Nevertheless, the sensitivity for $g_{a\gamma\gamma}$ is improved by more that three orders of magnitude compared to previous laser experiments (due to improvements of $>10^7$ in ε_a and ψ_a) and is comparable to the bounds established from analysis of the evolution of red giant stars [16], $g_{a\gamma\gamma} < 2.4\times10^{-10}$ GeV^{-1} for hadronic axions and $g_{a\gamma\gamma} < 10^{-10}$ GeV^{-1} for DFSZ axions (Fig. 2.4).

A summary of limits from previous searches for axion-like particles is given in Fig. 2.5. While astrophysical arguments rule out GUT axions satisfying Eq. (2.5) for most of the mass range $m_a>10^{-3}$ eV, only two types of laboratory experiments have had sufficient sensitivity to reach the GUT axion line. These are the telescope search [18], which covers a narrow range 3 eV$<m_a<$8 eV, and particle decay experiments [15], which rule out GUT axions for $m_a>6$ keV. The microwave cavity experiments of the University of Florida group [19] and the Rochester-Brookhaven-Fermilab group [20], which search for axions in the galactic halo come the next closest (about a factor of 50 from the GUT axion line). Van Bibber et al. [21] have proposed an improved cavity experiment to reach the GUT axion line in this region. The previous laser experiments cover a broader axion mass range, but are many orders of magnitude from the GUT axion line. One recent experiment which is missing from Fig. 2.5 is the search for axions produced in the Sun by Lazarus et al. [22]. This experiment rules out a roughly rectangular region with $g_{a\gamma\gamma}<4\times10^{-9}$ and $m_a<0.1$eV.

Our proposed experiment will probe a substantial amount of phase space on the $g_{a\gamma\gamma}$ vs. m_a plot (Fig. 2.5), which has not been investigated by laboratory means. This includes the region $m_a<2\times10^{-4}$ eV, where we expect to establish the limit $g_{a\gamma\gamma}<2\times10^{-10}$ GeV^{-1}, and also most of region 2×10^{-4} eV$<m_a<$100 eV, where the limit from the birefringence measurement will improve on previous work. The solid line drawn in by hand in Fig. 2.5 represents the expected limits for the proposed experiment (see also Fig. 2.4).

2.3 Improvement in the Proposed Experiment over Previous Laser Experiments

In order to understand clearly the enormous increase in sensitivity of the proposed

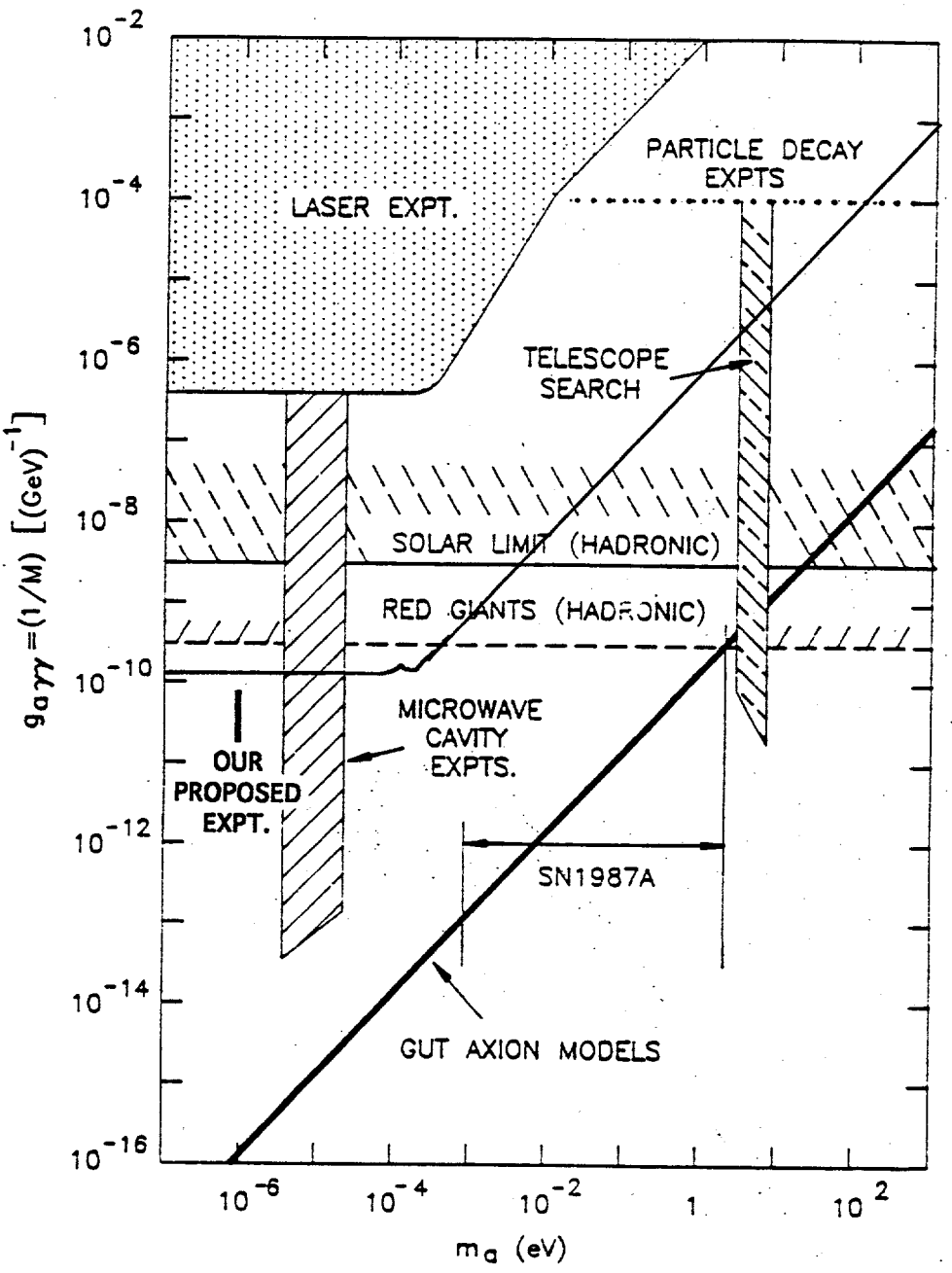

Figure 2.5 Limits on axion mass and axion-two-photon coupling from other experiments and astrophysical considerations. The heavy solid line is the predicted relationship between $g_{a\gamma\gamma}$ and m_a for axions imbedded in GUT models. This figure is reproduced from Ref. 17.

experiment over previous optical birefringence and rotation experiments in a magnetic field, it is useful to discuss the best previous experiment in more detail. That is the multipass experiment of the Rochester-Brookhaven-FNAL-Trieste (RBFT) collaboration [2,17]. In that experiment a Herriott optical delay line cavity is used to reflect the optical beam back and forth many times through the magnetic field region. This method avoids the problem of maintaining resonance conditions in interferometric multipass configurations such as the Fabry-Perot cavity of our proposed experiment. However, the number of passes is not high, the required magnet bore size is large, and reflection spots on the mirrors of the Herriott cavity often come close to the input and exit holes. The latter two problems make that method susceptible to systematic errors associated with scattered light and movement of the mirrors or beam tubes.

The important parameters for our proposed experiment and the RBFT experiment are compared in Table 2.3. The ratios of these parameters, raised to the power that they contribute to ψ_{QED}, ψ_a and ε_a, are listed in the last three columns. The total enhancement factors for the proposed experiment over those of the RBFT collaboration are listed at the bottom and range from 10^7 to 10^9. It can be seen that the improvement derives mostly from increased signal, rather than more sensitive angle measurements. In fact, the shot noise limit in the RBFT experiment, 4.3×10^{-11} rad, is comparable to that of the proposed experiment. The most significant factors are the large increase in N, arising from the use of a high-finesse Fabry-Perot cavity, and the 10x longer length of the magnet string, made possible by the availability of the SSC magnets. A somewhat larger B field and reduced systematic effects in the birefringence and rotation measurements also contribute significantly to the improvement.

The sensitivity of the RBFT experiment for birefringence was nearly four orders of magnitude short of the predicted QED signal. With an enhancement of 2×10^7 in this experiment, the QED signal will not only be observable, but it can be measured with <0.5% precision. The expected improvements in the limits for axion-photon coupling, $g_{a\gamma\gamma}$, are the square root of the birefringence and rotation enhancement factors in the last two columns of Table 2.3. The total predicted improvement of 3-4 orders of magnitude in $g_{a\gamma\gamma}$ is consistent with the more detailed calculations in Fig. 2.4.

Parameter	Previous Experiment	Proposed Experiment	Enhancement Factors for ψ_{QED}	ψ_a	ε_a
N_ψ	34	8.87×10^4	2600	2600	
N_a	254	1.33×10^5			520
B^2 (T^2)	4	35	8.8	8.8	8.8
l (m)	8.8	90	10	1100	100
ψ_{min}	2×10^{-9}	3×10^{-11}	67	67	
ε_{min}	6×10^{-10}	2.5×10^{-11}			24
Total enhancement factor:			**2×10^7**	**2×10^9**	**1×10^7**

Table 2.3. Important parameters for the previous (RBFT) and proposed optical birefringence and rotation experiments. In both cases the number of passes N and the minimum measurable angle are different between the birefringence and rotation experiments. Thus separate numbers are listed. In columns 4-6 the enhancement factors associated with each parameter are listed (for small m_a). The total at the bottom is a product of individual enhancement factors for each experiment. The improvement factor for $g_{a\gamma\gamma}$ in axion searches is the square root of the listed enhancement factors.

2.4 References

[1]. S. L. Adler, Ann. Phys. (N. Y.) **67**, 599 (1971).

[2]. Y. Semertzidis, R. Cameron, G. Cantatore, A. C. Melissinos, J. Rogers, H. J. Halama, A. Prodell, F. Nesrick, C. Rizzo and E. Zavattini, Phys. Rev. Letters **64**, 2988 (1990).

[3]. G. Raffelt and L. Stodolsky, Phys. Rev. D**37**, 1237 (1988).

[4]. T. Kinoshita and D. R. Yennie, "High Precision Tests of Quantum Electrodynamics- An Overview" in T. Kinoshita, *Quantum Electrodynamics* (World Scientific, Singapore, 1990) p. 2.

[5]. T. Kinoshita , "Theory of the Anomalous Magnetic Moment of the Electron - Numerical Approach", in T. Kinoshita, *Quantum Electrodynamics* (World Scientific, Singapore, 1990) p. 218-321.

[6]. T. Kinoshita and W. J. Marciano, "Theory of the Muon Anomalous Magnetic Moment ", in T. Kinoshita, *Quantum Electrodynamics* (World Scientific, Singapore, 1990) p.

419-478.

[7]. Proposed muon anomalous magnetic moment experiment at Brookhaven National Laboratory.

[8]. P. Rullhusen, W. Muckenheim, F. Smend, M. Schumacher, G. P. A. Berg, K. Mork and L. Kissel, Phys. Rev. **C23**, 1375 (1981).

[9]. T. Kinoshita and M. Nio, Phys. Rev. Letters **72**, 3803 (1994).

[10]. W. Heisenberg and H. Euler, Z. Physik **38**, 314 (1936).

[11]. R. D. Peccei and H. Quinn, Phys. Rev. Letters **38**, 1440 (1977).

[12]. J. E. Kim, Phys. Rev. Letters **43**, 103 (1979); M. A. Shifman, A. I. Vainshtein and V. I. Zakharov, Nucl. Phys. **B166**, 493 (1980).

[13]. M. Dine, W. Fischler and M. Srednicki, Phys. Letters **104B** 199 (1981); A. Zhitnitsky, Sov J. Nucl. Phys. **31**, 260 (1980).

[14]. R. Stryonowski and A. R. Zhitnitsky, "Axion search with optical technique", preprint SMU-HEP-94-12.

[15]. M. S. Turner, "Windows on the Axion", Brookhaven 1989, Proceedings, Cosmic Axions.

[16]. G. G. Raffelt and D. S. P. Dearborn, Phys. Rev. **D36**, 2211 (1987).

[17]. R. Cameron, G. Cantatore, A. C. Melissinos, G. Ruoso, Y. Semertzidis, H. J. Halama, D. M. Lazarus, A. G. Prodell, F. Nesrick, C. Rizzo and E. Zavattini, Phys. Rev. **D47**, 3707 (1993).

[18]. M. A. Bershady, M. t. Ressell and M. S. Turner, Phys. Rev. Letters **66**, 1398 (1991).

[19]. C. Hagmann et al., Rev. Sci. Instrum. **61**, 1076 (1990).

[20]. S. DePanfilis, A. C. Melissinos, B. E. Moskowitz, J. T. Rogers, Y. K. Semertzidis and W. U. Wuensch, Phys. Rev. Letters **59**, 839 (1987); Phys. Rev. D40, 3153 (1989).

[21]. K. Van Bibber et al., "A proposed search for dark matter axions in the 0.6-16 μeV range", LLNL preprint UCRL-JC-106876 (March 1991).

[22]. D. M. Lazarus, G. C. Smith, R. Cameron, A. C. Melissinor, G. Ruoso, Y. K. Semertzidis and F. A. Nezrick, Phys. Rev. Letters **69**, 2333 (1992).

3. THE OPTICAL INTERFEROMETER

A simplified scheme of the proposed optical interferometer for the QED/axion experiment is shown in Fig. 3.1. The output of a Nd:YAG laser is frequency-doubled and sent into an ultrahigh-finesse Fabry-Perot cavity. A strong magnetic field exists in most of the length of the cavity. The input laser polarization is at 45° to the B field. Reflected light from the cavity will be used for birefringence measurements, and transmitted light will be used for rotation measurement. Each of the polarization components parallel and perpendicular to the B field direction is separately locked to its own cavity resonance using the reflected beam. The phase difference between the two polarization components will be measured as a direct readout of the small frequency difference between them. A new scheme of phase measurement is developed by this collaboration and will be discussed in Section 3.4. Preliminary results obtained during the course of this study will be presented in Section 3.5.

The improvement of the present scheme over previous optical searches of axion will come from an increase in the number of reflections through the use of the Fabry-Perot cavity ($N \sim 10^5$ instead of 254), a larger magnetic field (effective $B^2 = 35\ T^2$ instead of $4\ T^2$), a longer field region ($l = 90$ m instead of 8.8 m), a longer averaging time (2×10^4 s instead of 655 s), and careful elimination of systematic effects such as mirror motions through active-feedback control and passive isolation via suspension. In the following we will outline the different parts of the optical interferometer and the considerations that go into selecting the parameters.

3.1 The high finesse Fabry-Perot cavity

A Fabry-Perot cavity, formed by two mirrors, allows a light beam to reflect back and forth many times through the cavity. The interference between the multiply reflected beams produces the sharp frequency resonances allowed by the cavity. It is important for the proposed experiment that the incoming laser light is in resonance with the cavity. In the Pound-Drever-Hall locking scheme [1], the incoming laser light is frequency modulated such that the fundamental mode is in resonance with the cavity, but the modulation sidebands are reflected by the cavity. The reflected beams are demodulated to provide a feed-back signal for keeping the

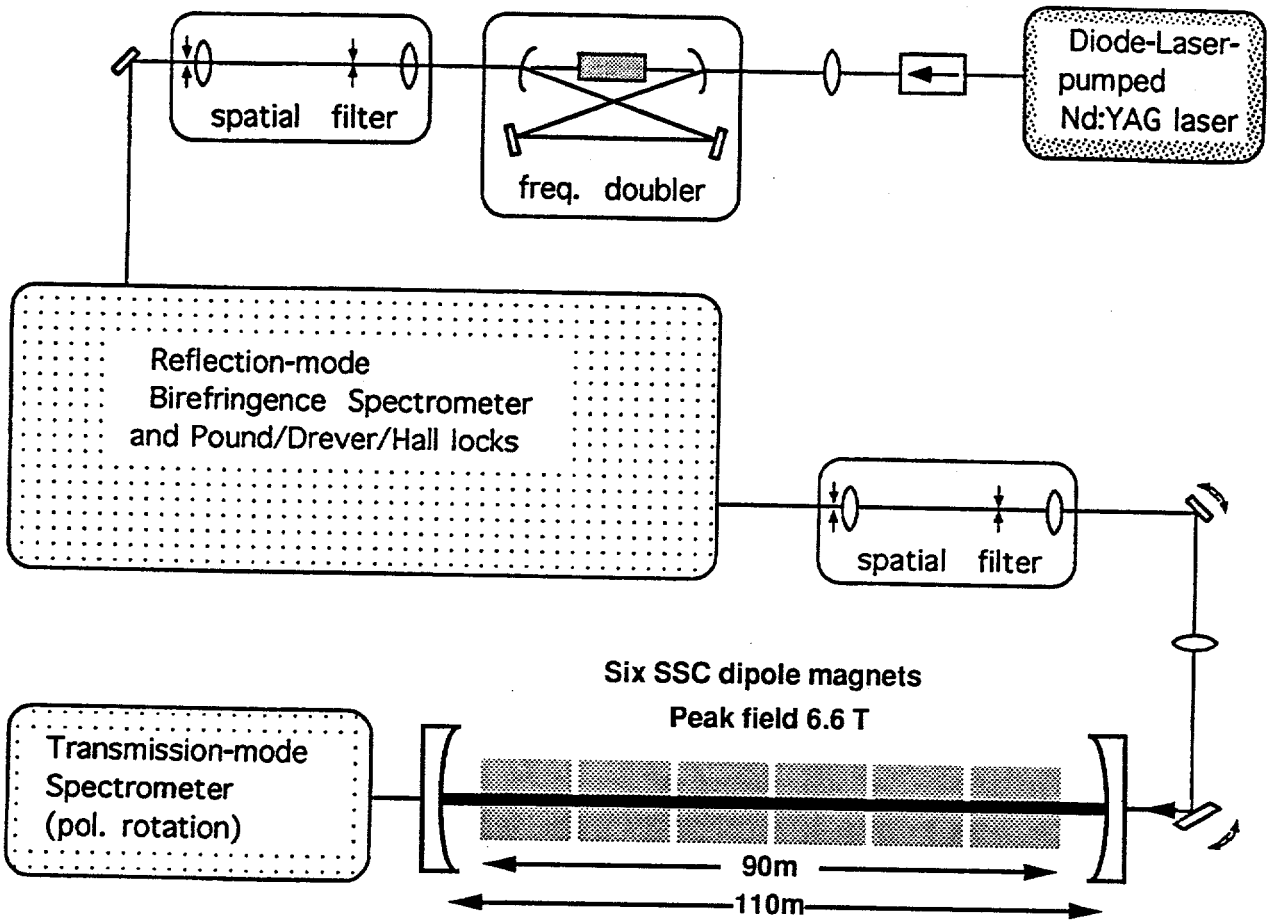

Fig. 3.1 Schematic optical configuration of the proposed experiment. The magnetically induced birefringence due to QED effects will be measured with a reflection-mode spectrometer, while rotation of the polarization of the light from possible axion induced effects will be measured with a transmission mode spectrometer.

laser in resonance. The Fabry-Perot resonance condition is given by:

$$\frac{2\pi}{\lambda} nL+\phi_c=2m\pi \qquad (3.1)$$

where m is an integer, n is the index of the medium in the cavity, L is the length of the cavity, λ is the vacuum wavelength of the light, and ϕ_c is any other accumulated phase shift such as due to mirror reflection phase shift and birefringence or laser higher spatial order modes. There is an additional constant phase due to diffraction. The resonance condition basically states that the phase increment acquired by one round trip through the cavity should be equal to an integer number of 2π's.

On resonance, both the transmitted beam out of the back mirror and the reflected beam from the front mirror carry the phase information of the multipassed light beam. In the proposed experiment, the light will be polarized at 45° to the magnetic field direction. Since the // and the $\perp$ polarizations will have different refractive indices due to possible axion and QED induced birefringence, the two polarizations will have slightly different resonance conditions. In addition, measurements by this collaboration show that the intrinsic and mounting-stress induced birefringence in the mirrors will contribute a DC birefringence on order of a few Hz. If the cavity is in resonance with, say, the // polarization beam, then we find that the ellipticity (defined as 1/2 the phase difference between the two polarizations) of the reflected beam is

$$\psi=\psi_1\cdot(2\cdot\frac{F}{\pi})\cdot\beta \qquad (3.2)$$

where F is the finesse of the cavity (defined as $\pi\sqrt{R}/(1-R)$, R being the mirror reflectivity), ψ_1 is the ellipticity acquired in a single pass through the magnetic field, and β is a constant ≈ 1 and dependent on measurable mirror coating parameters. Eq (3.2) is written in such a form as to illustrate that the equivalent number of reflections in a Fabry-Perot cavity is

$$N\approx 2\frac{F}{\pi} \qquad (3.3)$$

Thus the reflectivity of the mirrors must be exceedingly high to achieve large number of passes. At the same time the scatter and absorption losses must be small enough to allow enough

transmission through the cavity.

Considerable progress has been made in recent years in the development of high quality super-polished substrates with surface roughness at the Angstrom level, and in the growth of extremely low-loss thin-film dielectric coatings. Interferometer mirrors with total scattering and absorption losses below 5×10^{-6} are now commercially available [2]. To maintain such low losses, a clean environment is needed during the assembly of the Fabry-Perot interferometer. In custom-made, super-polished mirrors with specially fabricated dielectric coatings, the loss is measured to be as low as 1.6×10^{-6}. A Fabry-Perot interferometer with finesse of 10^6 has been demonstrated with these custom-made mirrors, but for a small beam radius of 84 μm [3]. Similar performance should be possible for a long interferometer, provided that the vibration noise of the mirrors relative to the laser wavelength can be reduced sufficiently to maintain such a finesse. However, for the initial design of the interferometer, we will choose a loss figure of 5 ppm for the mirrors. As more experience is obtained with the operation of large cavities, we anticipate that this loss figure may be improved in the future to the 1ppm level.

The parameters chosen for our proposed Fabry-Perot interferometer are listed below:

Total length of interferometer L	110 m
Total magnetic field region *l*	90 m
Mirror reflectivity R expressed as 1-R	15 ppm
Mirror transmission T	10 ppm
Finesse F	2.09×10^5
Free spectral range	1.36 MHz
Cavity fringe full width half max	6.51 Hz
Intracavity circulating power	5 kW
Mirror radius of curvature	100.5 m
Confocal parameter z_o	50 m
Minimum waist radius at 532 nm w_o	2.91 mm
Mode radius at mirror w	4.33 mm
Mirror diameter	5 cm (2")

The mode size of the laser in the cavity is chosen to minimize the mode size at the entrance and exit ends of the magnet bore. This will reduce the stray light scattering problem, which will be discussed in Section 7.2. The mode size dictates the radius of curvature of the mirrors. The mirror diameter is then determined from consideration of diffraction losses around the edges of the mirror. For the proposed interferometer, the diffractive loss for a TEM_{00} laser beam is estimated to be less than 10^{-9} for a 3 cm aperture [4]. Standard 2" diameter mirror substrates are more than adequate. The finesse of the cavity is chosen to be sufficiently high to allow detection of QED induced birefringence and from considerations of state of the art mirror technology as mentioned above. The free spectral range of this cavity is 1.36 MHz and the resonance peaks have a full width at half maximum of 6.5 Hz. Thus it is imperative that the laser source should be pre-stabilized in frequency and that ground vibrations are isolated. The vibration isolation of the interferometer mirrors and the associated optics of the birefringence and rotation spectrometers will be discussed in Sections 3.3 and 5.2.

We have found in our laboratory that the intrinsic and stress-induced birefringence in the mirror coatings may be several orders of magnitude larger than the effects that we plan to measure. Indeed this static birefringence is expected to produce a slight offset of ~Hz in the resonance frequencies of the // and the $\perp$ polarization components. An important question to investigate is how stable are the value and the eigen-directions of the intrinsic birefringence. The problems associated with static mirror birefringence and its power dependence will be discussed in more detail in Section 3.3. The rationale for limiting the intracavity circulating power to 5 KW will be discussed in Section 3.4.

The magnetically induced birefringence and dichroism in the coatings and the substrates are predominantly linear in the B field, and can be basically eliminated by magnetic shielding. As a precaution, any remaining effects can be subtracted out by reversing the direction of the B field. The SSC magnets are yoked so the stray field is quite small to begin with, and the mirror chambers are far away enough so that very little field from the magnets is present near the optics. Nevertheless, we consider it good practice to shield the stray B field to about 1 μG in the mirror chamber. The induced magnetic birefringence and rotation effects (the Cotton-Mouton and Faraday effects, respectively) due to the residual gas in the magnet bore will be considered in

Section 7.1.

3.2 The laser source

Important considerations for the choice of a laser source are the available power, the wavelength, and the stability of the output power, frequency, and beam-pointing direction. In general, mirror coatings are much better regarding absorption and scattering losses in the visible region than in either the UV or IR regions. A larger laser power is desirable for a better shot-noise limited signal-to-noise ratio. Unfortunately high power lasers (>> 1 W) are fairly noisy and do not operate in the shot-noise limited regime. Furthermore, using too high a power in the Fabry-Perot cavity will cause heating of the mirror, resulting in degradation of the mirror performance. Diffraction loss, arising from the finite size of the vacuum beam pipe and mirror diameter, scales exponentially with the laser wavelength and is substantially less important for visible wavelengths as compared to infrared radiation.

Our laser of choice is a 700 mW diode-pumped Nd:YAG continuous wave laser, frequency-doubled to the visible at 532 nm. The Nd:YAG "MISER" laser is commercially available [5], easy to operate, relatively low cost, and operates near the shot-noise limited regime. Doubling efficiency of 69% has been reported in lithium-rich lithium niobate crystal, using a resonant external cavity for second harmonic generation [6]. In our laboratory we are currently operating at a doubling efficiency above 50%, so after accounting for the associated losses in the various optics used for preparation and modulation of the laser beam, it is reasonable to expect delivering a total of 150 mW of 532 nm light to the input of the Fabry-Perot cavity.

In our collaboration, we have developed the techniques [7] and have demonstrated that the frequency of such a frequency-doubled "MISER" laser can be accurately pre-stabilized to tens of milli-Hertz [8] using a resonator-cavity with the comparatively high bandwidth of 12 kHz. This pre-stabilization is more than sufficient to allow locking the laser to the large Fabry-Perot cavity.

3.3 Seismic isolation and control of the optical interferometer

The unmitigated seismic motion would contribute to a frequency noise of more than 1 MHz, therefore some seriously powerful suppression of this *a priori* seismic noise will be essential as its value corresponds to more than 10^5 resonance linewidths of our cavity. the first step is to use passive isolation. The approach here is along the ones developed by the gravitational wave community and in investigations carried out in our laboratory. All the birefringence and rotation measuring optics will be mounted on inertial platforms which are vibrational isolated from the ground and the interferometer vacuum chamber by stacks of rubber/steel plate isolation mounts. The cavity mirrors are suspended from the platforms to allow independent control of the tilt and axial motions of the mirrors. The passive seismic isolation ensures that rapid ground motion is not communicated to the mirror. Although we are left with rather large motions still, the rates are vastly reduced by the pendulum which acts as a mechanical low-pass filter. Next we can actively damp the pendulum motion to keep the cavity in near resonance with the optical frequency. At this point the mirror motion corresponds to ~ 4 cavity linewidths, and there is no easy way to do better on the mechanical side.

Current suspension techniques used in the gravitational wave LIGO project, using both passive isolation and active controls, are such that a noise level of $\sim 10^{-18}$ m/$\sqrt{\text{Hz}}$ has been achieved for frequencies above 500 Hz [9, 10]. In our own work we focussed on passive and active vibration control, using active first stages of isolation to remove the large amplitude excursions present in a less than ideal situation. A factor of $>10^3$ reduction in the vertical motion has been achieved in one system, and a factor of 100 reduction in all six degrees of freedom has been obtained in another setup by our colleagues. The tilt noise (from the twisting motion of the mirrors) will cause a degradation of the cavity finesse. We estimate that a 0.1 μm displacement of the beam in each transit is just tolerable to maintain the finesse. The mirror tilt angle will be controlled to better than a nano-radian with the use of active feedback, using either of two recently published approaches [11, 12].

3.4 Birefringence measurement

This experiment generates unrivalled demands for measurement precision, far beyond that attainable with the best contemporary or even futuristic atomic clocks. The closest previous effort is that associated with the gravitational wave detection projects approaching construction phase in the US (the LIGO project [11]) and in several overseas collaborations. Like these experiments, we must be sensitive to exquisitely small effective optical phase shifts, $\approx 10^{-13}$ rad. Additionally, in our experiment we need a concept which is robust against seismic perturbations because it would be difficult to modulate the superconducting magnets at kilohertz rates. It is useful to contrast our interferometer design with the laser interferometer design for gravitational wave detection. In our proposed experiment, the slow magnet modulation means that we can use ultra-high reflectivity mirrors and consequent long effective path lengths. In the gravitational wave detector, the signal to be sought is intrinsically of kHz, thus requiring low storage time (i.e., low finesse) and high optical power.

The most important difference between this experiment and the LIGO project, and the previous RBFT [13] optical experiment is that we will have enough sensitivity to accurately measure a non-zero physical quantity, namely the magnetically-induced birefringence due to the QED effect, in the presence of an irreducible background birefringence associated with the mirror fabrication and mounting: Our projected accuracy is about 10^{-9} of this background. So it is clear that *only frequency-based approaches* will have the necessary dynamic range and intrinsic calibration stability for this demanding application.

The basic scheme of the birefringence spectrometer is shown in Fig. 3.2. The incoming laser light is split into two paths with orthogonal polarizations. Two acousto-optic modulators (AOM1 & 2) shift the frequency of the two channels independently. Each channel is frequency modulated with electro-optic modulators (EOM1 & 2) which operate at different modulation frequencies. The two beams are recombined, sent through a rotating half-wave plate, and mode-matched into the high finesse Fabry-Perot cavity. Additional optics and modulator are used to provide optical isolation and to ensure the proper polarization states for the laser beam when entering the cavity.

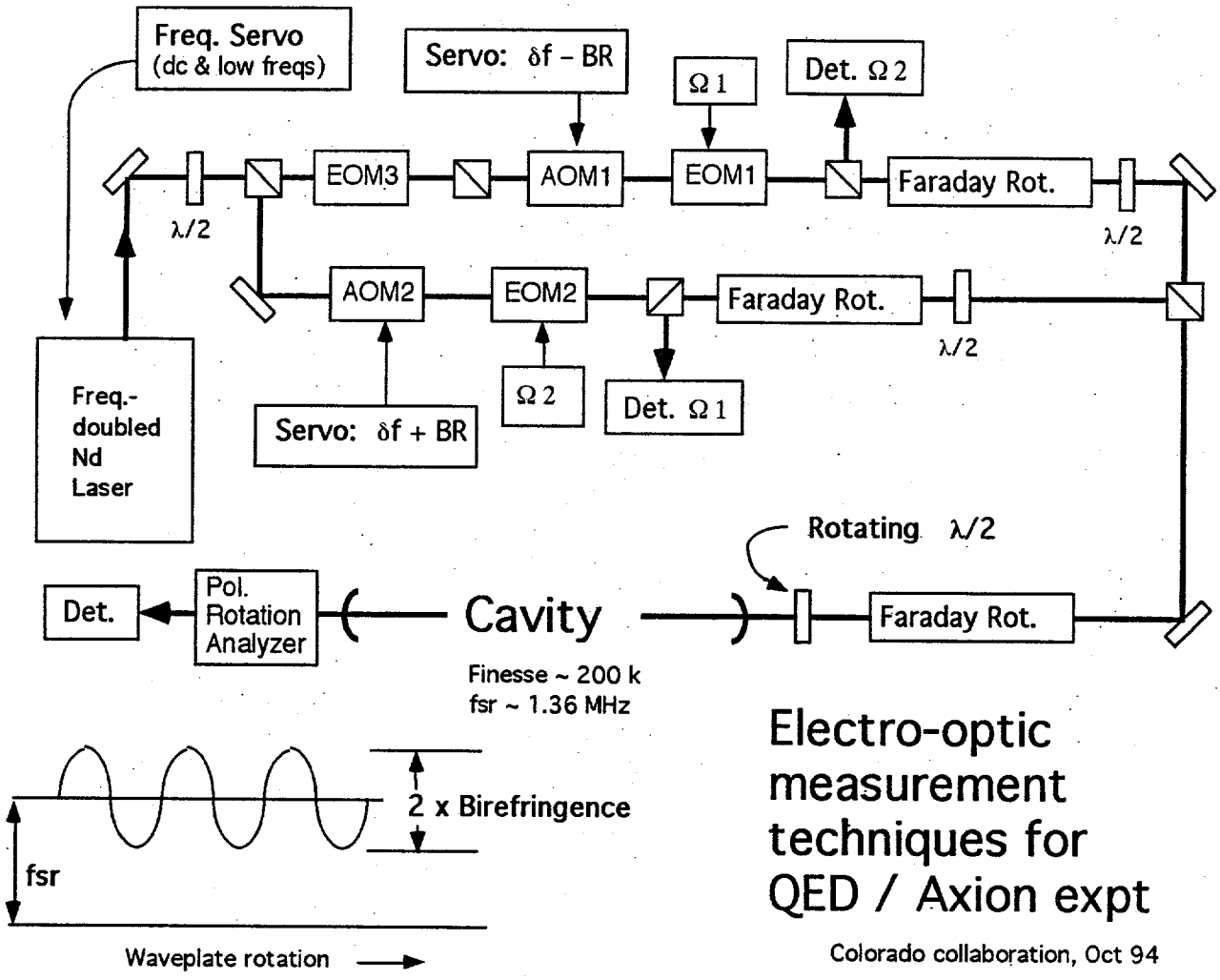

Fig. 3.2 The electro-optical measurement techniques for the proposed experiment. A direct measurement of the frequency difference between two orthogonal polarization directions of the laser light gives the QED/axion induced birefringence due to passage of light through a strong magnetic field region in the high finesse Fabry-Perot cavity

The frequency of each polarization component is separately locked to be on resonance with the Fabry-Perot cavity via the Pound-Drever-Hall FM locking scheme [1]. The frequency difference between the two polarizations is directly proportional to the birefringence, as can be seen from Eq. (3.1)

$$\nu_{\perp}-\nu_{/\!/}=\frac{c}{2n_oL}\left(\frac{\Delta n}{n_o}+\frac{\Delta\phi}{2\pi}\right) \qquad (3.4)$$

Here n_o is the average index of refraction of the two polarizations, $\Delta n = n_{/\!/} - n_{\perp}$, and $\Delta\phi_c$ is predominantly due to the birefringence of the mirror. The quantity $c/2n_oL$ is the free spectral range of the cavity.

An important attribute of the QED and axion signatures is that they can be configured to produce an optical phase (or intensity) difference between two orthogonal optical polarizations. Suppose the mirrors of our high finesse cavity are arranged so that they have their principal axes of birefringence to be basically parallel (or perpendicular) to the magnetic field direction to an accuracy of a few degrees. Then the two polarization modes will have slightly different resonance frequencies because of the mirror birefringence. For example, in studies carried out in our laboratory with a 27.7 cm long cavity, the mirrors introduce a phase difference of 3.4 μrad which corresponds to a 300 Hz difference frequency between the two polarization eigenmodes for this short cavity. This work will be described in Section 3.5. Similar quality mirrors to be used in the proposed 110 m long interferometer would yield a difference frequency of ~ 3/4 Hz. Our task is to read this ~ Hz beat frequency to an accuracy of < 1 nHz, and to measure the 30 nHz QED induced birefringence changes caused by the magnetic field sweep.

The good news is that because the cavity resonance frequencies of the two polarizations are so nearly equal, any effects due to uncompensated seismic perturbations will be strongly suppressed. However, in Section 3.3, we have found that local opto-mechanical seismic controls will still leave the cavity mirrors with a residual motion of ~ 4 cavity linewidths. Accordingly, we turn to the possibility of shifting the laser wavelength rapidly enough to maintain the

resonance accurately enough for the QED or axion birefringence measurement.

We will do this frequency-shifting using two acousto-optic modulators (AOM1 and AOM2 of Fig 3.2), one for each of the two polarization components. In order to satisfy the common-mode suppression of seismic noise, we must shift these two frequencies by exactly the same amount. We also must have these frequencies different as they must match their separate cavity eigen frequencies extremely precisely. The appropriate method to escape this dilemma is to synthesize the rf drive frequencies for the AOMs from a common stem, which includes full seismic compensation of the error signals which are common in the two channels -- this is the seismic signal. The gain of this loop begins at ~100 kHz in our present loops, and tracks out the seismic perturbations to 10^{-4} linewidths with only a pure integrating servo. Using a loop rising faster than 1/f toward lower frequencies leads to an additional factor ~10^3 which is fully sufficient for our measurement, when we recall its differential character.

Tracking the difference in the polarization eigenmode frequencies is an interesting challenge because of the dynamic range and precision requirements already mentioned. Only frequency methods can suffice. We must choose between reading out a servo-defined frequency or generating a precise frequency modulation by Direct Digital Synthesis (DDS), and then testing whether we have chosen the correct amount to match the sum of mirror plus QED birefringence. This is our method, in which a measurement iterates with a trial change of the DDS frequency offset, basically forming a stepwise servo system. Because the full birefringence signal has been precisely suppressed nearly exactly (the Hertz level BR signal is reduced to within the μHz step size of the DDS), the remaining signal can be digitized comfortably (12 bits is more than sufficient). Calibration of the analog scale is readily accomplished by offsetting the DDS by a few μHz and noting the analog response. The QED signal then manifests itself as a field-dependent change in this BR readout signal, amounting to a peak to peak frequency difference of 60 nHz .

We now turn to addressing the problems that are likely to arise. In projecting to measure a birefringence change of some 10^{-9} of the mirror's intrinsic birefringence, which in itself is about 1 ppm of an optical wavelength, it is sure that some essential problems with drift will occur. For

one, the mirror's birefringence is observed to be inhomogeneous spatially, changing by a few percent across a 1" sample. To hold this change to the size of the QED signal implies that the light beam centroid should be unmoving relative to the mirror with a tolerance ~50 nm. This requirement obviously leads to the need for an active angle-steering capability for the cavity illumination. Remembering that the mirrors are mounted via a pendulum suspension, we see that this position servo will need appreciable bandwidth (~ kHz).

An important compromise is involved in the choice of intra-cavity circulating power. Higher power reduces the random noise of the measurement by $\sim 1/\sqrt{P}$, but leads to heating and consequent birefringence due to power absorbed at the ppm level in the mirror coatings. Experience shows that good performance is still possible with circulating power in the 5 kW range, and this is our design point. As better mirrors become available it will be useful to revisit this choice.

As described so far, we would have two optical frequencies applied to the mirror, with a frequency splitting in the Hz range or below. Taken in conjunction with the heating response problem noted above, this small frequency difference clearly will not be a suitable actual choice for doing the measurement. In fact we have also observed interesting polarization-mode interactions already at low intracavity powers (< 1W), which we are presently attributed to photorefractive-type responses at a very low level. So it is necessary to do the locking and data readout with a much larger frequency interval between the two polarization modes. A natural choice is to shift the frequency of one of the polarization by exactly the 1.36 MHz cavity free-spectral range (FSR) splitting of the long interferometer. This is judged to be an adequate solution with regard to the mirror-heating problem, but costs tremendously in the required performance of the anti-seismic controls. Basically the residual physical motion of the pendulum-suspended mirror now maps into slightly different phase excursions for the two beams, according to their 2.4×10^{-9} difference in wavelengths. An elegant solution to this situation is incorporated into our design, whereby one of the polarized beams is split into two equal components, separated by 2 cavity FSRs, one upshifted, the other down-shifted relative to the reference frequency for this polarization. Now the Pound-Drever-Hall lock system produces a cavity-lock signal free of seismic noise. The exact frequency supplied to EOM3 is not critical (~1 Hz) and can be refined

by measurements in an additional rf detection channel as described by DeVoe et al. [14].

3.5 Results of birefringence data measured with preliminary spectrometer

A preliminary investigation of measuring small phase differences in a high finesse Fabry-Perot cavity was carried out in our laboratory. The cavity was a 27.7 cm fixed cavity with a finesse of 4.5×10^4. The optical scheme of this work is similar to that of Fig. 3.1. In this preliminary experiment, a frequency-stabilized He-Ne laser was used and the transmitted beam of the Fabry-Perot cavity were used for locking. The optical frequency of the laser was servo-controlled to bring the vertical polarization component to be in resonance with the cavity. The frequency of the horizontal polarization component was brought into precise resonance, however, with the next cavity order by shifting its AOM frequency. (Thus for this study, the seismic contribution was not common mode and remained an important noise source.) Since there was a small birefringence of ~3.4 μrad present in the mirror coatings, the optical frequencies of the two polarization components differed by 304 Hz (+ one FSR of 541 MHz). Therefore the rf frequencies of the AOMs must change to maintain both resonances as the slowly rotating half-wave plate exchanged the two polarization states in the cavity. The recorded change in the rf frequency is shown in Fig. 3.3(a). The data show the sinusoidally varying phase changes as the polarization of the incoming light is being rotated relative to the birefringent axes of the cavity.

The available optical power was < 20 μW for one polarization, which corresponds to ~ 6.4×10^{13} photons/s. The relative fluctuations is then expected to be approximately 1.3×10^{-7} with 1 s of integration. In terms of spectral density, analysis leads to a theoretical shot noise limited precision of 1.8×10^{-7} /$\sqrt{\text{Hz}}$. With a cavity linewidth of 12 kHz, this theoretical limit is 2 mHz/$\sqrt{\text{Hz}}$. These first data have a noise level that are many times this theoretical limit, due mainly to problems of inadequate optical isolation and excessive acoustic noise in our laboratory. These problems should be easily remediable. The Fourier distribution of the measured birefringence is shown in Fig. 3.3 (c) for frequencies near the proposed magnet modulation frequency (5 mHz). The present sensitivity is about -80 dB relative to the mirror birefringence of 304 Hz, giving an index of refraction measurement sensitivity $\Delta n/n$ of 6.5×10^{-17}. It is interesting to extrapolate this result to the proposed interferometer. The proposed interferometer

(a)

(b)

(c)

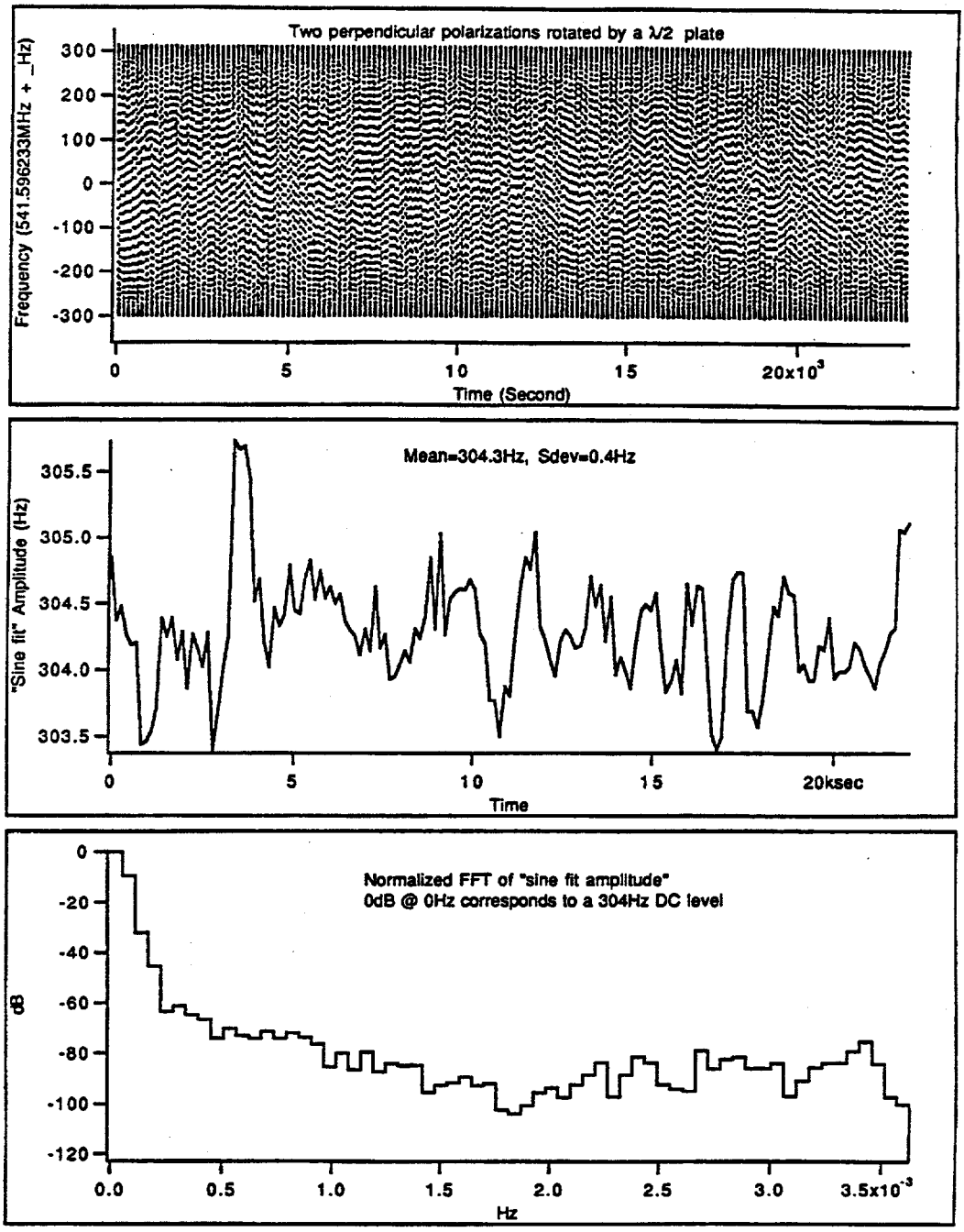

Fig. 3.3 Birefringence data measured with preliminary spectrometer.
(a) Time series showing 160 cycles of sinusoidal frequency change between two different cavity eigenfrequencies, dependent upon the rotation of the input linear polarization relative to the cavity birefringence axes.
(b) Amplitude of sinusoid fit to data. Plotted data are fitted cycle-by-cycle, and averaged over four cycles, corresponding to a full 360° rotation of the half-wave plate.
(c) Fourier distribution of measured birefringence. Near our projected magnet modulation frequency, the present sensitivity is about -100 dB relative to the mirror birefringence and is limited by a number of remediable systematic effects.

will have a cavity linewidth of 6.5 Hz instead of the current 12 kHz. This improves the sharpness of the phase discrimination by a factor of 1.8×10^3. The power detected will be about 50 mW instead of 20 μW, giving a factor of 50. The combined improvements results in $\Delta n/n$ measurement precision of 7×10^{-22}. The expected QED Δn is 1.4×10^{-22}. This very rough extrapolation shows that the present result is not that far off from our expectation for the proposed interferometer.

3.6 Rotation measurement - a means to search for the axion

In the presence of a strong magnetic field, an axion creation event would lead to a small absorption of the laser field component polarized parallel to the static magnetic field. If the light beam is polarized at 45° to the magnetic field direction, such a preferential absorption of one polarization component would lead to a small rotation in the polarization vector of the recombined beams. In the RBFT experiment [13], the rotation was searched for by using an analyzer whose transmission axis was orthogonal to the original polarization axis of the main beam. A small rotation ε in the polarization leads to a small transmission of intensity ε^2 through the crossed analyzer. In other words the small rotation has "uncrossed" the analyzer. A Faraday cell was used before the analyzer to introduce a much larger, time-dependent rotation $\eta(t)$. Heterodyne detection produces a useful interference term $\eta\varepsilon$ in the intensity which is linear in ε. As in that previous experiment, it is desirable for us to "uncross" the polarization analyzer in an ac manner to produce an ac signal. Our experiment will be enormously more sensitive and a factor of 10^7 improvement is anticipated. See Table 2.3.

When we examine the transmitted light beam through the cavity, the experimental configuration described above for the QED measurement will produce light beams of very slightly different frequencies for the parallel and perpendicular polarizations to the magnetic field direction. Because of this frequency difference, the recombined beam at +45° will show a slow beating, with the photocurrent of the form $1 + \cos\delta\omega t$, where $\delta\omega \sim 2\pi \times 3/4$ Hz is the angular frequency between the two laser beams. The perpendicular choice for the analyzing prism will yield $1 - \cos \delta\omega t$. So the "crossed" analyzer does not stay crossed and it is clear that we lose the option to take both birefringence and polarization rotation data simultaneously.

In a dedicated axion search experiment then, we will follow the RBFT's method of supplying a single optical frequency polarized at 45° to the magnetic field. Now the crossed polarizer is really crossed and we can employ a magnetic or other polarization dither scheme to achieve the desired heterodyne detection at some frequency of a few hundred Hz as employed by RBFT. One minor difference in our experiment is that the cavity finesse is very high and the two polarization modes will have slightly different eigenfrequencies. So the phase of the two transmitted polarization components will be differentially delayed by ~ 2 $\tan^{-1}$ (0.75 Hz/6.5 Hz) = 6.6° or about 0.11 rad. However, a stable phase compensator system, such as a Babinet-Soleil compensator, will restore the perfect phase equality, and hence we will still have the very dark null when looking through the crossed analyzer.

3.7 Evaluation of the shot noise limited performance of the interferometer

Due to mirror birefringence effect as discussed in Section 3.4, a circulating power of 5 kW inside the Fabry-Perot cavity is chosen as our design point of the interferometer. With mirrors of transmission $T = 1\times10^{-5}$ and loss $L = 5\times10^{-6}$, the transmitted power P_t = (5 kW)(T) = 50 mW. The incident power needed to maintain this circulating power is calculated based on the Pound-Drever-Hall (PDH) modulation scheme, and is found to be P_i = 128 mW. These power values corresponds to $N_t = 1.3\times10^{17}$ photons/s and $N_i = 3.4\times10^{17}$ photons/s, respectively. In general we expect the statistical fluctuations to be on order of $\sqrt{N}$ for a counting type experiment.

To estimate the shot noise for the PDH scheme, we suppose that the incident laser beam is frequency modulated at frequency Ω with a modulation index m, then the electric field may be written as

$$E=E_i\,[J_o(m)\cos(\omega t)+J_1(m)\cos(\omega+\Omega)\,t-J_1(m)\cos(\omega-\Omega)\,t] \qquad (3.5)$$

where ω is the optical frequency, the J(m)'s are Bessel functions with argument m. Higher order harmonics are neglected in the above equation. The FM frequency Ω is chosen such that, on resonance, only the fundamental frequency (the J_0 term) is transmitted into the cavity and the side bands are reflected. In other words, Ω should be >> the cavity linewidth.

3.7.1 Birefringence measurement shot noise limit

For the QED birefringence experiment, measurements will be made with the reflected beams. On resonance, the reflected fundamental beam is destructively interferred, so the photodiode sees a background light mostly due to the sidebands only, ~ $2J_1^2N_i$. Since the PDH scheme is a heterodyne detection scheme, the birefringence signal (measured as a phase in radians) is proportional to the cross term, $2J_oJ_1N_i$. As a first approximation we take the signal-to-noise (S/N) ratio as simply S/N ≈ $J_o(N_i\tau)^{1/2}$, where τ is the integration time of the experiment. Using a modulation index of 0.5, this corresponds to a birefringence sensitivity (defined as N/S) of 1.8×10^{-9} rad/$\sqrt{\tau}$. The total QED induced birefringence phase shift is calculated from Eq. (2.2) as 1.3×10^{-8} rad. (Note the ellipticity of Eq. (2.2) is defined as half the birefringence phase shift. The equivalent number of passes for the proposed interferometer is 8.89×10^4 for the reflected beams.) Therefore this first approximation indicates that a 0.5% QED experiment will require about 800 s of integration, if the system is statistically limited.

However in an actual experiment we are measuring the current in a photodetector when light is incident on it. The statistical fluctuations due to the random emission of photoelectrons (shot-noise) produce a noise current given by

$$i_n = \sqrt{2eI\Delta B} \qquad (3.6)$$

where i is the photodetector current, e is the charge of the electron, and ΔB is the bandwidth of the detection circuit. A typical conversion factor η between power and photocurrent at 532 nm is 0.3 mA/mW. Thus for reflected beam on resonance, $i = \eta(P_r)$, where P_r is the reflected power. Nominally $P_r = 2J_1^2P_i$, but in reality the fundamental mode "fringe" is not completely dark, and there are also higher order harmonics that are reflected. The slope of the PDH discrimination curve provides a conversion from signal photocurrent to phase change. A signal current of $\eta(2J_oJ_1P_i)$ is equivalent to a single round trip cavity phase change of $(\pi/F)(1-R)/T$ radians. Therefore the phase detection sensitivity is

$$\left(\frac{S}{N}\right)_{BR} = \left[\frac{\pi}{F}\frac{1-R}{T}\right]\frac{\sqrt{2e\eta P_r}}{2\eta J_o J_1 P_i} rad/\sqrt{Hz} \qquad (3.7)$$

Note that the above equation is the shot-noise limit for the phase shift of a single round trip. We can identify the quantity in the first bracket as (effective number of round trips in the reflection mode)$^{-1}$ when comparing the result to Eq. (3.3). We also note that the incident power is split equally between the two polarizations. We need to keep track of them separatively, and add their shot noise contributions in quadrature. In terms of spectral density, our analysis shows that the shot noise limited sensitivity in the total birefringence is 2.4×10^{-8} rad /$\sqrt{}$Hz. With a six hour integration time (2×10^4 s), the shot-noise limit is 3.3×10^{-11} rad, which is 0.5% of the calculated QED value.

Improvements of the birefringence shot-noise limit, aside from going to longer integration time or larger intracavity power, are possible by the use of an asymmetric mirror cavity. In this configuration the transmission and the reflectivity of the two cavity mirrors are purposely chosen to be unequal. If T_1 and L_1, and T_2 and L_2, are the transmission and loss of the input and output mirrors respectively, then the reflected fundamental mode on resonance is completely dark when $T_1 = T_2 + L_1 + L_2$. For example, choosing $L_1 = L_2 = 5 \times 10^{-6}$ and $T_2 = 1 \times 10^{-5}$ as before, the transmission of the input mirror should be chosen as 2×10^{-5}. Keeping the same 5 kW internal power, the shot noise limit is improved by a factor of 2. In fact the finesse of this asymmetric cavity, 1.57×10^5, is less than the symmetric case, and the incident power required is also less, 113 mW. This indicates the power of a completely dark fringe in improving the signal-to-noise of the measurement.

3.7.2 Rotation measurement shot noise limit

The rotation measurement uses the transmitted beam. Since the scheme of the measurement method is similar to that of the RBFT experiment, the shot noise performance of the system should be similar also. The shot-noise limit calculated in ref. 14 was 4×10^{-9} rad/$\sqrt{}$Hz. However, in our case the transmitted beam has only a power of (50 mW)(J_1^2) = 44 mW as

compared to their 200 mW. Therefore we expect that our shot noise will be some 2x higher, and the rotation sensitivity will be ~8.5 x 10^{-9} rad/$\sqrt{Hz}$. Detailed analysis of our system gives a shot-noise of 9.2x10^{-9} rad/$\sqrt{Hz}$. The sensitivity improvement of the present experiment comes not from shot noise considerations, but from the vastly increased number of passes, a longer B field region and higher field strength, as was discussed in Table 2.3.

3.8 References

[1]. R. W. P. Drever, J. L. Hall, F. V. Kowalski and J. Hough, G. M. Ford, A. J. Munley and H. Ward, Appl. Phys. B **31**, 97 (1983).

[2]. Research Electro-Optics Inc., Boulder, Colorado 80301.

[3]. G. Rempe, R. J. Thompson, H. J. Kimble and R. Lalezari, Opt. Lett. **17**, 363 (1992).

[4]. H. Kogelnik and T. Li, App. Opt. **5**, 1550 (1966).

[5]. Lightwave Electronic Co., Mountain View, Calif., model 122-1064-700F.

[6]. D. H. Jundt, M. M. Fejer, and R. L. Byer, R. G. Norwood and P. F. Bordui, Opt. Lett. **16**, 1856 (1991).

[7]. Ch. Salamon, D. Hils and J. L. Hall, J. Opt. Soc. Am. B **5**, 1576 (1988).

[8]. J. L. Hall, to be published.

[9]. A. Abramovici et al., Science **256**, 325 (1992).

[10]. A. Gillespie and F. Raab, Phys. Lett. A **178**, 357 (1993).

[11]. K. Kawabe, N. Mio and K. Tsubono, Appl. Opt. **33**, 5498 (1994).

[12]. N. M. Sampas and D. Z. Anderson, Appl. Opt. **29**, 394 (1990).

[13]. R. Cameron, G. Cantatore, A. C. Melissinos, G. Ruoso, Y. Semertzidis, H. J. Halama, D. M. Lazarus, A. G. Prodell, F. Nezrick, C. Rizzo and E. Zavattini, Phys. Rev. D **47**, 3707 (1993).

[14]. R. DeVoe et al., Phys. Rev. A **37**, 1802 (1988).

4. MAGNET SYSTEM

4.1 Magnet String Requirements

The previous sections have discussed the dependence of the QED/axion experiment on the magnetic field magnitude and the integrated field length. The superconducting high field dipole magnets that are available have been operated as a system at the ASST but under conditions different than those required by the proposed experiment. The ASST test group has operated a magnet string which included ten dipoles at currents up to 7000 A successfully. The general operational issues are well understood as are the requirements and procedures necessary to assemble and operate a magnet string. Since the magnets already exist, their operational envelope will define limits under which this experiment can be performed. The operational questions that need to be answered involve at what rate the magnets can be ramped, and over what range of current values can they be operated at a given ramp rate. The maximum ramp rate the ASST magnet string was operated at was 4 A/s and then only for one cycle at a time. During single magnet testing, data were taken on the performance of the individual magnets at ramp rates up to 250 A/s. This data were used in defining the proposed operational parameters for the string as discussed below. For this experiment, a six magnet string has to be specified to be ramped at 100 A/s from 1000 A to 6000 A and back, cycle at a nominal inlet temperature of either 3.8 or 4.35 K. The ramping cycle will be trapezoidal in shape, with 50 s up and down ramps, and 50 s plateaus at minimum and maximum currents. The final ramp frequency is 5 mHz.

The question of at what maximum field the cycle should go to has been complicated by the vacuum that can be achieved in the beam tube. The Cotton-Mouton effect, discussed in Section 7.1, from the residual H_2 in the beam tube becomes the limiting factor for the magnetic field. The CM effect has the same B^2 field dependence as the effect we wish to observe. Therefore, vacuum quality in the beam tube is what will determine the upper limit of the magnetic field. This problem may be helped by lowering the operating the temperature of the magnets, but since the CM effect of H_2 increases with decreasing temperature, the gain may not be apparent.

In principle it is advantageous to go to higher ramp rates to help reduce the stability requirements in all aspects of the experiment. However, the low ramp rate proposed in the present experiment is partially mitigated by the optical detection scheme, in which the slow magnet modulation appears as sidebands of a higher frequency, in this case by modulating the incoming polarization of the light. Considering the technical difficulties associated with increasing the ramp rate by even a factor of three, there is no compelling reason to do so at this point. Once the concept of this optical measurement technique is proven, any advances in magnet technology that permits higher ramp rates and higher maximum fields can certainly be taken advantage of.

At this point, given that the magnets already exist, the interferometer and the vacuum systems become the two areas where significant improvements can be made that will impact the outcome of this experiment. What should be stressed here is that this is not a magnet system experiment. The experimental requirements on the magnet system do not present any technical demands that are not well understood and solvable given existing technology. As discussed below, the optimum magnets will be selected and the operational envelope for the resulting system will be defined by test. The one parameter that can be varied is the operating temperature of the string. This will be discussed below.

In order to produce the desired magnet field for the proposed QED/axion experiment, we plan on using six of the many (~21) prototype SSC Collider Dipole magnets that are available in the existing inventory of magnets. A conceptual design of a string of 6 magnets is presented in this section. The magnet system requirements and characteristics are listed in Table 4.1.

4.2 Magnet Selection Criteria

The desired ~90 meter length of magnetic field will be achieved by forming a string of six 15 meter SSC prototype dipole magnets. It is necessary to select a set of six magnets based on test performances and to evaluate the cryogenic requirements that can meet the desired ramp rate and field modulation. The main criteria are the quench performance, the ramp rate behavior, and the AC losses. These issues will be discussed in the following sections.

Table 4.1 The magnet system requirements

Six Magnet String Parameters	
Dipole Magnet Length (end plate to end plate)	15.256 m
Desired Field Length	89.7 m
Field Modulation	1 to 6 Tesla
Desired Ramp Rate	75 to 100 A/s
String Operating Temp.	3.8 K or 4.35 K
Dipole Field Measurement Accuracy	≤ 0.1 %
Beam Tube Clear Aperture	> 38 mm
String Inlet Temperature	~3.8 K
Interconnect Region Length (end plate to end plate)	1.159 m
Inductance per Magnet	≈76 mH
6-Magnet String Inductance	≈ 456 mH
Power Supply Output Current	≥8000 Ampere
Power Supply Output Voltage	>100 V

4.2.1 Quench Performance of Magnets:

For the purposes of this experiment we need magnets that can be ramped at ≥ 100 A/s and have the highest field possible without reaching quench current. The quench current is a function of the ramp rate and operating temperature, i.e., Iq= Iq(dI/dt, T). Figs. 4.1 and 4.2 show the ramp rate dependence of the quench current at 4.35 K for the prototype dipole magnets built at BNL and FNAL. The BNL magnets typically show less sensitivity to the dI/dt ramp rate, which may be due to the different cooling conditions used at BNL. This was a cross flow helium circulation scheme which provided a significant mixing of helium in the cold mass and the annular region between the coil and the beam tube. The He flow rate used at BNL was also higher, 100 g/s, as compared to 50 g/s at FNAL. The Fermilab magnets did not have any crossflow cooling mechanism. All prototype magnets built either at BNL or FNAL were tested at the ramp rates between 4 and 250 to 350 A/s at 4.35 K. Almost all the magnets were successfully tested for up to 300 A/s for their down-ramp behavior.

4.2.2 Ramp Rate Behavior of Magnets

During current ramping of a magnet, the changing magnetic field ($d\mathbf{B}/dt \propto dI/dt$) causes eddy currents to flow in the conductor. Large eddy currents can be produced due to lower (≤ few μΩ) interstrand resistance in the cable The eddy currents can cause heating of the cable and thus lowering the quench current. The ramp rate studies and ac loss measurements on these magnets showed two distinct types of behavior. The concave down curves represent type-A behavior and the concave up curves represent type-B behavior. Typically type-A magnets had higher AC-losses than type-B. For both A and B types, there seems to be a threshold near a ramp rate of 50 A/s for higher rate of degradation in quench current, and for the location of the quench origin to move to the multi-turn section of the inner coils where the field component is perpendicular to the wide face of the cable and higher heat generation is expected. Multi-turn section is also the place which gets the least amount of cooling through conduction by the He stream. In Figs. 4.1 and 4.2, the quench current for Type-A magnets shows a lower gradient for dI/dt ≤ 50 A/s but has a larger slope for high ramp rates. Typical type-B magnets have a lower gradient in the high ramp rate region but still show a decrease in their quench currents at the edge of the low ramp

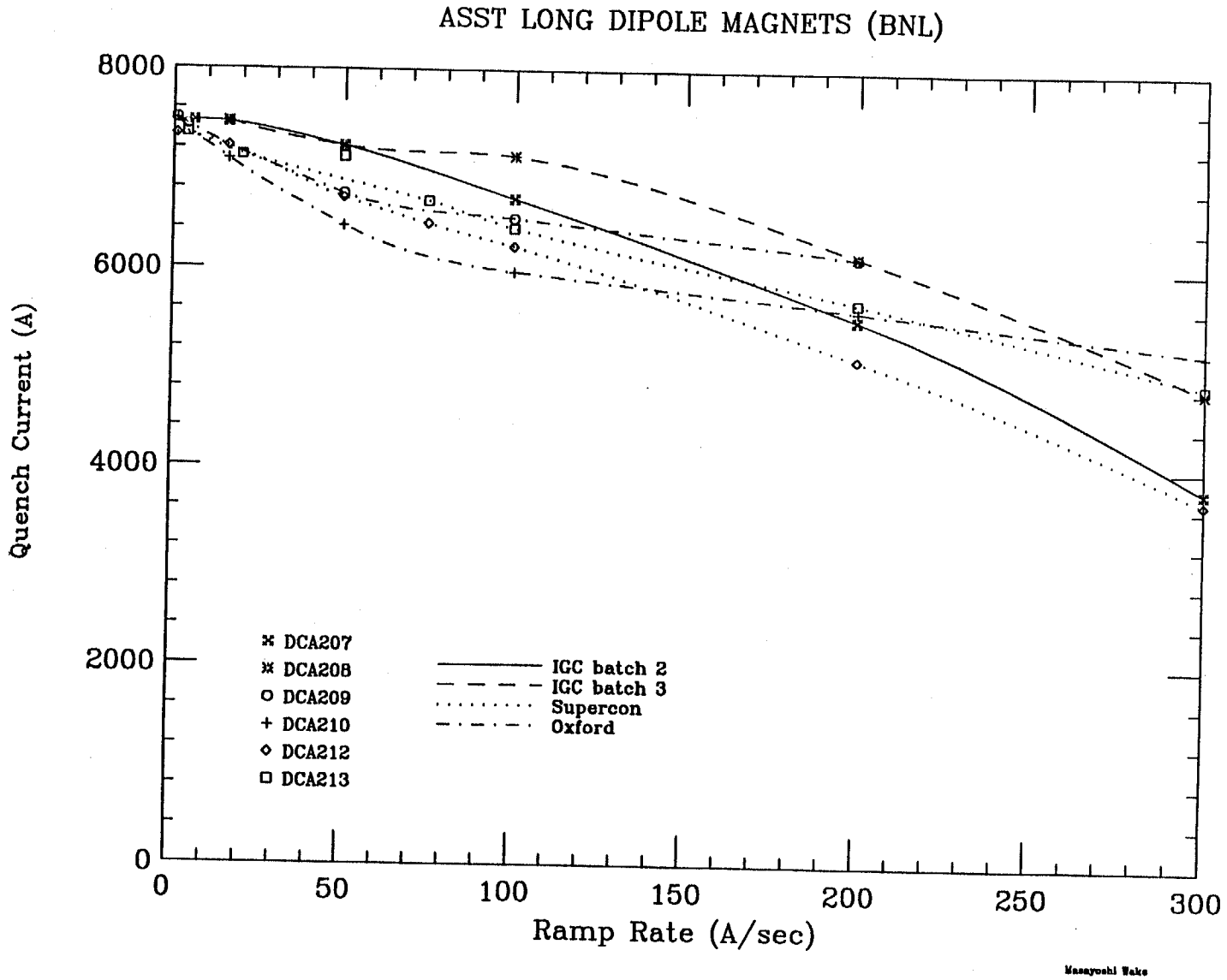

Fig. 4.1 Quench current versus ramp rate for ASST long dipole magnets (BNL)

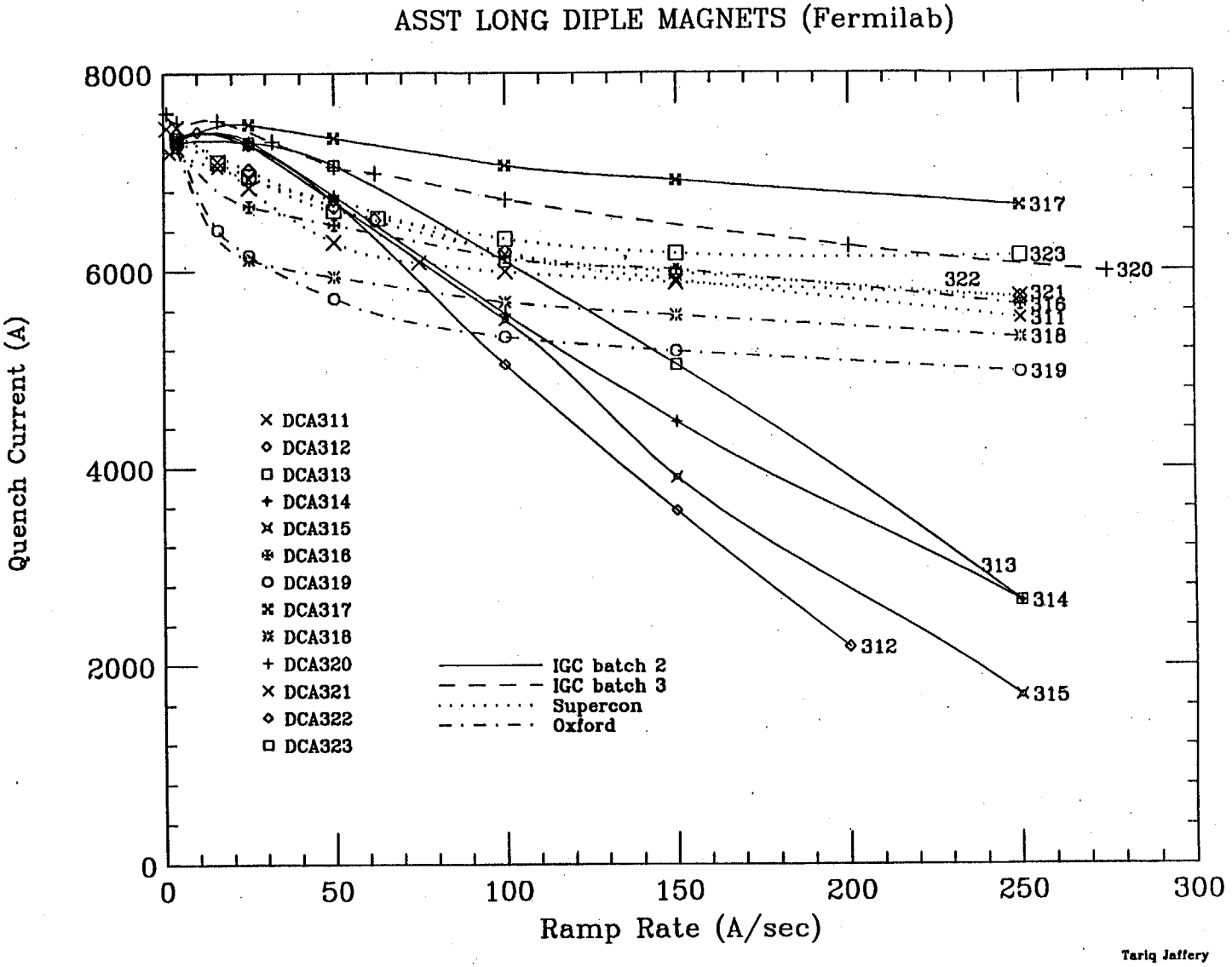

Fig. 4.2 Quench current versus ramp rate for ASST long dipole magnets (FNAL)

rate region. The exceptions are DCA317 and 320, which are improved type-A magnets that behave as type-B. The performance of these two magnets is not expected to degrade over time. It is even possible that the quench performance may improve, due to the increased oxidation of superconductor over time, which can increase the interstrand resistance and reduce the eddy current generation [1].

Therefore the magnets of choice should have sufficient quench current margin above 6000 A and the quench currents do not fall off rapidly in high dI/dt region. Type-B magnets, which exhibit low sensitivity at high ramp rates, in general satisfy these conditions. However, some type-A and improved type-A magnets which show low overall sensitivity to ramp rate can also meet these criteria.

4.2.3 AC Loss Measurements

A measurement of the total energy deposited in the magnet during current ramping can characterize the behavior of a magnet. AC losses are due to the superconductor hysteresis losses, yoke material, copper wedges, and eddy current heating in the magnet coil. AC loss measurement results as a function of dI/dt are shown in Fig. 4.3. Type-A magnets in general have higher eddy current losses (higher heating) than type-B magnets. The agreement among all magnets for hysteretic losses was quite good. The quench current gradient, i.e., dIq/d(dI/dt) as a function of eddy current loss (J/A/s)) for the region above 100 A/s shows that higher eddy current generation results in lower quench current [2]. In other words, this kind of behavior in the high ramp rate region is due to eddy current heating which is a thermal phenomenon. There is a clear correlation between the dI/dt dependence of quench current and the ac losses of magnets. Therefore the dI/dt dependence of the quench current and the AC loss are two main performance criteria for selecting magnets for our purposes. Table 4.2 shows the measured hysteresis and eddy current losses for most of the selected magnets. The AC loss as a function of ramp rate is given by the following:

$$\text{AC loss} = \{ \frac{\text{hysteresis loss} + (\text{eddy current loss per cycle} \times dI/dt)}{\text{time length of cycle in seconds}} \} \text{ Watts}$$

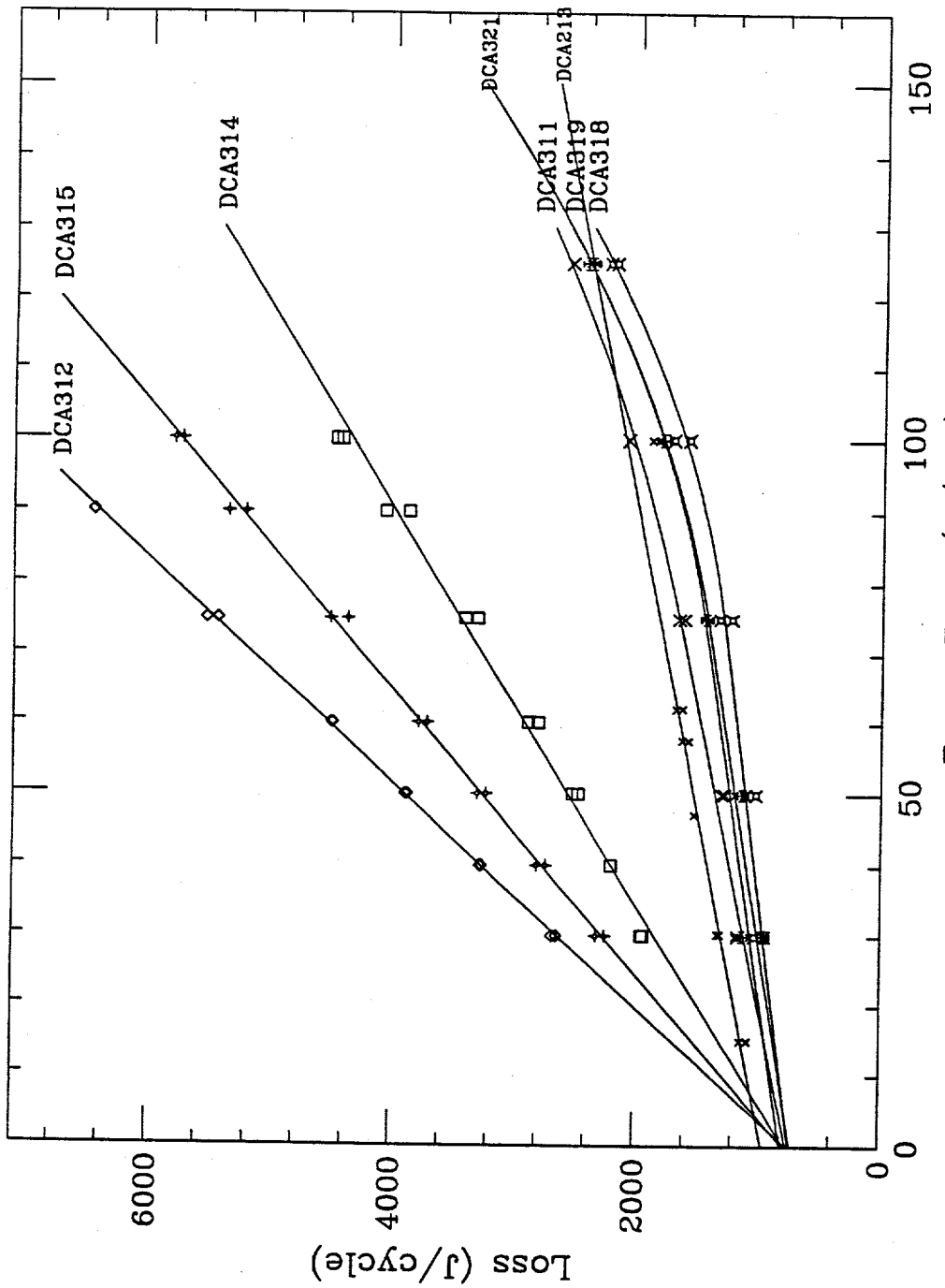

Fig. 4.3 The AC loss versus ramp rate of some of the dipole magnets.

Table 4.2 AC Loss Summary

Magnet Name	Cable in/out	L_0 (mH)	Eddy Loss J/(A/sec)	Hysteresis Loss Joules
DCA311	S/I	75.9	12.0	744.
DCA312	I/I	75.9	63.0	739.
DCA314	I/I	75.9	35.7	759.
DCA315	I/I	75.9	49.7	769.
DCA317	S/S	75.9	~7.0	~800.
DCA318	O/K	75.9	7.46	723.
DCA319	O/O	75.9	9.36	713.
DCA320	I/S	75.9	11.2	738.
DCA321	O/S	75.9	9.95	795.
DCA322	O/S	75.9	19.7	780.
DCA323	O/S	75.9	11.5	731.
DCA213	S/S	75.9	11.5	946.
DCA211	S/S	75.9	11.5	946.

(S: Supercon, I: IGC, O: Oxford, K: Outokumpu)
DCA series are full size 15m magnets.

where hysteresis loss is given in Joules/cycle (sec), eddy current loss in J/A/sec and dI/dt in A/s. The AC loss measurements were done at varying ramp rates for a monopolar cycle of 500-5000-500 ampere at 4.35 K at 1-atm.

4.2.4 List of Selected Magnets

Based on the selection criteria described above, i.e., we have selected six magnets and some spares for the proposed experiments. These magnets, listed in decreasing order of their quench performance at a ramp rate of 100 A/s, are shown in Table 4.3.

4.2.5 Thermal Effect on Magnet Performance

The temperature dependence of quench current for these magnets is about 18% / K [3]. The measured difference in plateau quench current (ΔIq) were well above the predicted value based on short sample magnet performance, in the normal temperature range $\geq$ 3.8 K. Thus,

Table 4.3 Desirable Magnets In Order of Decreasing Preference

Magnet	Quench Current (Ampere)		AC loss in Watts	Bus Type	AC lossType
DCA	**@ 100A/s**	**@ 150 A/s**	**100 A/s**		
208	7125	6126	26.27	cw	A→B
317	7060	6904	--	cw	A(I2)→B
320	6987	6244	20.64	cw	A(I3)→B
207	6698	5499	--	cw	A
209	6502	6128	--	cw	B
213	6403	5671	23.29	cw	B
323	6322	6170	20.9	ccw	B
212	6222	5100	--	ccw	A
322	6185	5980	30.55	cw	B
311	6170	5901	--	--	--
316	6126	6004	--	ccw	B

variation of operating temperature, in any direction can change the operating envelope of these magnets. The formula to compute Iq at a given temperature is :

$$I_q(3.8K \le T < 4.35K) = I_q(T=4.35K)\ [1+.18(\Delta T)]$$

For example for DCA208, Iq(4.35K) =7125A, but when the temperature is lowered to 3.8 K the magnet quench current may increase by roughly 700A. Thus we may see an Iq (3.8 K) = 7125 + 705.4 = 7830.4 A.

4.3 Magnetic Field Issues

4.3.1 Transfer function

The field of a magnet is a function of its coil current. The transfer function to convert current to magnetic field is given in Table 4.4. Between 2 and 5 kA the transfer function 1.044 is almost linear. Around 5 T the iron yoke becomes magnetically saturated and there is a degradation in the magnetic field. At 6 T the transfer function is lowered by ~2%.

4.3.2 Magnetic field harmonics

Field harmonics are also a function of the ramp rate [4] The field harmonics are defined as the expected values of harmonics when the effect of iron saturation and persistent current in the coil can be neglected. The harmonics for these magnets are measured in "unit" which is defined as 10^{-4} of the fundamental field measured at a 1 cm radius. The harmonics are typically a few units and are of no consequence to our proposed experiment

Table 4.4: Field Measurement Values at Different Currents

Magnet Current (kA)	**B** Field (Tesla)	Transfer Function
2.0	2.090	1.045
3.0	3.135	1.045
4.0	4.176	1.044
4.5	4.694	1.043
5.0	5.21	1.042
6.0	6.158	1.026

4.3.3 Mechanical Behavior of SSC Magnets

The proposed string of six magnets will be modulated between 1 and 6 T. However, the mechanical design of the collider dipole magnets for the SSC was meant for operations at 6.6 T, at a temperature of 4.35 K. However, almost all the magnets being considered for the proposed string have been previously ramped to fields >7 T at 4.35 K.

The stainless steel collars in a magnet serve to position the superconductor coil and to provide restraint against motion excitation which might change the field shape or cause premature quenching of the magnet. The collars precompress the coils by an amount larger than the sum of the Lorentz (I x B) forces on the conductors, and they have sufficient bending stiffness so that the deflections are limited to < 0.1-0.2 mm under excitation. Approximately 50% of this prestress is lost upon cooldown due to differential contraction between the coils and the collars. The yoke provides additional support to the collars near the horizontal mid-plane, to limit deflections under the horizontal Lorentz force. The stainless steel cold mass shell is pretensioned by weld shrinkage to 200-250 MPa at room temperature to firmly clamp the yoke around the collared coil. The thermal contraction of the shell is larger than the yoke, so the shell pretension grows to 350-400 MPa with cooldown and provides adequate clamping to restrain the Lorentz force up to fields well above the design operating point. With the collars supported by the yoke, the coil deflections under excitation are limited to ~0.02 mm [5,6].

The average azimuthal coil stress has a smooth monotonic dependence on the square of the magnet excitation current. With excitation, the Lorentz force compresses the coil in the azimuthal and radial directions, thus reducing the prestress. Test results have shown that the coil stress remains positive and there is no sign of unloading even at 7.5 kA [3, 7]. The end force measured between the coil end clamp and the end plate increases in proportion to current squared. The longitudinal force in the end is estimated [3] at 3 kN / (kA)2. This is a small fraction of the total electromagnetic force in the coil, as most of the axial force is transferred to the shell through friction between coil and the support structure.

Several magnets have been tested successfully at 3.8 K and some magnets were also tested

at 1.8 K. Most of the magnets have gone through at least one or two thermal cycles, where they were warmed up to room temperature and then were tested again at He temperatures. There is sufficient data to convince us that the mechanical design of these magnets is sufficiently robust and the quench performance of these magnets has not been affected by thermal cycles, repeated excitation and quenching at high currents. It is highly unlikely that continuous ramping of the magnets between 1 and 6 kA will have any ill effects on the mechanical structure of the magnets. Although there may be some thermal cycle fatigue effect in the coil and end piece composites, these are probably not significant enough to cause any mechanical failures in the magnet structure. After all, these magnets were designed to survive 25 years of synchrotron radiation exposure.

4.4 Cryogenics Considerations

The measured hysteretic and dynamic losses for each magnet under consideration are shown in Table 4.2. Average AC losses for Type-B magnets are ~22 W per magnet and static losses are 1.5 W for each magnet. Total heat load on the refrigerator is approximately 151 W at 4 K and 44 W in the 20 K line.

4.4.1 Heat Load

If all of the AC loss is transferred to He, the total temperature drop across a magnet/string is given by:

$$Q = m\ Cp\Delta T$$

where Q is the heat load in W (due to AC loss etc.), m is the flow rate of He in gm/sec, Cp is the heat capacity for He (in J/gm-K) and varies with the He bath temperature, and ΔT is the temperature drop across the magnet/string. The total temperature drop across one magnet at different flow rates is listed below (assuming Cp=3.95J/gm-K).

Q (watts)	flow rate (gm/s)	ΔT (mK)
24	130	47
24	100	61
24	50	122

If the inlet temperature of He at the feed end can is 4.35 K, then the total temperature rise across a 6-magnet string will vary in accordance with the above approximation depending on the He flow rate. For m=50 and 100 gm/sec, the ΔT across the string is 0.5 K and 1 K, respectively.

For a He inlet temperature of 4.35 K and a flow rate of 100 gm/s, Table 4.5 gives the outlet temperature of He across each magnet in a 6-magnet string (assuming dI/dt = 100 A/s). Table 4.6 lists the heat loads for a 6-magnet string.

Table. 4.5 Temperature changes across each magnet in a six magnet string. He mass flow rate = 100 gm/sec

Inlet Temperature = 4.35 K		Inlet Temperature = 3.8 K	
Outlet Temp (w/o recooler)	Outlet Temp (with recooler)	Outlet Temp (w/o recooler)	Outlet Temp (with recooler)
4.41	4.41	3.88	3.88
4.47	4.47	3.96	3.96
4.53	4.53	4.04	4.04
4.59	4.41	4.11	3.88
4.64	4.47	4.18	3.96
4.7	4.53	4.25	4.04

Table 4.6 **Heat Loads for a 6-magnet String (all magnets are 50 mm aperture SSC prototype).**

	Liquif.	4 K ASST	20 K measured	80 K values
	g/s	Watts	Watts	Watts
String Static Heat Load				
Single Dipole	0	(1.5)	(5.6)	(37)
6 Dipoles (entire string)	0	9.0	34	222
Feed End Can	N/A	5*	5*	-
Return End Can	N/A	5*	5*	-
Total Static Heat Load	N/A	19	44	222
String Dynamic Heat Load				
Single Dipole	0	(22)	0	0
6 Dipoles (entire string)	0	132	0	0
Total Dynamic Heat Load	0	132	0	0
String Total Heat Load	**~5†**	**151**	**44**	**222**

Calculation for six magnet string is based on measured values obtained during ASST testing.
*These values are based on Fermilab experience with tests on 40mm SSC string test at E-4R.
† Estimated value.

4.4.2 Recooler

The thermal energy produced by each magnet due to the induced AC losses is a characteristic of the magnet and cannot be changed. Whereas He flow rate and the inlet temperature to the string can be controlled. By increasing the flow rate we can limit ΔT across the string. If flow rate is a limiting factor then the inlet temperature of He can be adjusted to achieve the desired temperature in the last magnet of the string in order to have an adequate quench current margin. A recooler can be installed in the string to keep the string at an optimum operating temperature. As a contingency plan for the proposed experiment, a recooler capable of removing 100 W could be installed between the third and fourth magnet to lower the He temperature and allow us to gain sufficient operating temperature margin.

4.5 Power System Requirements

The accumulated operating experience with the ASST style magnets in both full cell and half cell configurations has been at low ramp rates (< 4 A/s) and without cyclic operations. This experiment requires high ramp rates (about 100 A/s) and continuous cyclic operations between about 1000 to 6000 amps over periods of time of up to one month with a high degree of reliability (a minimum of 5 days continuous operations without a power supply related trip or failure.) The present ASST power supply built, by Dynapower, was adequate for the previous string related testing but would not be adequate for this experiment without additional work on the control and feedback circuits governing power regulation. This is an area where problems were previously experienced. The maximum output voltage (40 V) of one supply is not adequate to ramp the six magnet string proposed. This limitation can be overcome by placing three of these supplies in series, using one as a master and two as slave supplies with the proper control electronics. These control circuits do not yet exist and will have to be developed or purchased from the power supply manufacturer. This does not present any technical risk but represents work to be done and modifications to existing equipment. The specific requirements for the power system will depend on the final string configuration (load inductance) and the ramp rate chosen. If the host laboratory has a single power supply designed to power superconducting magnets with current and voltage output values require here, then that supply could be used.

A ramp generator and control hardware/software will have to be developed if the power supply (CECAR) system used at the ASST cannot be modified to provide the ramp control necessary or it is not cost effective to modify it.

4.6 Quench Protection System

The power supply and quench protection system must function together as an integrated system. The quench protection system is required to protect the magnets from possible damage that would result from an uncontrolled quench in the string. A quench occurs in a superconducting magnet when some portion of the superconducting cable or bus transitions from the superconducting to resistive state. If no action is taken, the quenching area would heat, its temperature would increase and the quench zone would grow. The energy from the power system and the non quenching magnets would continue to be dissipated in the quench zone and result in temperature which could damage the superconducting cable or magnet. In the ASST, the quench protection system monitored half coil voltage taps and calculated the resistive voltages (i.e. non inductive component which would be present during ramping) present during powered operations. The threshold for declaring a quench was set at values between 0.5 V and 1.0 V during different running periods. The quench protection system (QPS) responded to a quench by firing the heater firing units (HFU) into the protective strip heaters in each magnet in a quench protection unit (a quarter cell or three dipoles), phasing back the power supply to zero and inserting the dump resistor into the circuit. The quench protection heaters in each magnet served to drive the entire magnet coil resistive as soon after firing as possible by their design. This allowed the energy to be dissipated over a larger volume of superconductor and resulted in a lower over all coil temperature being reached. When the voltage drop across the magnet protection unit reach a few volts, the passive bypass diodes turned on and allowed current from the non quenching magnets to bypass the protection unit that quenched. The dump resistor in the power circuit was used to dissipate the energy stored in the non quenching magnets.

For this experiment there are at least two options to provide for the quench protection of the magnets. The present ASST QPM system could be used as it was configured for the half cell testing program with a few modifications. (The half cell contained five dipoles and one

quadrupole). The console displays would have to be changed to reflect six dipoles and the parameter tables for declaring a quench modified. (The proposed circuit for this experiment is essentially, the half cell circuit.) The major change required is the replacement of the passive diode stack with QPM controlled SCR's. This is necessary because of the large inductive voltages that develop across the string during the high current ramp required by this experiment. Due to a lack of documentation on the software for this system, using may not be cost effective. Also, the ASST QPM was designed for accelerator operations and if far more sophisticated than needed for this experiment.

A simpler and very cost effective alternative is to use analog circuits which compare voltages measured across balanced inductive load segments. For example, comparing the voltages across two half coils of a magnet with each other. The idea is that the inductive components will be the same for the same inductive load. If one of the circuits being compared develops a resistive voltage component, the comparator will detect the imbalance and signal that a quench is in progress. The quench in progress signal is then used to fire the HFU for the protection heaters in the magnets, turn on the bypass SCR's, insert the dump resistor in the circuit (i.e. fire the dump switch) and phase back the power supply. These analog circuits exist as modules called quench detection circuits (QDC's) and have been in use at FNAL for sometime. The first string test using 40 mm SSC prototype dipoles, conducted at ER at FNAL, used the QDC's as a back up to the QPM system under development. An updated design of the FNAL QDC circuit exists and the parts necessary to build ten modules existed at the SSCL but were never assembled. With this style of quench protection system, a data acquisition system capable of recording the voltages on the magnets for later analysis is necessary to determine the cause of the quench. (This was part of the ASST QPS.) The basic electronic modules for such a system were used in the ER testing and are part of the ASST equipment inventory.

Fig. 4.4 is a scheme for the power supplies and quench protection system. Adequate technical knowledge on quench protection for the proposed magnet string exists and there are no anticipated technical problems which are not solvable with existing technology.

4.7. Optics and Magnet String Interface

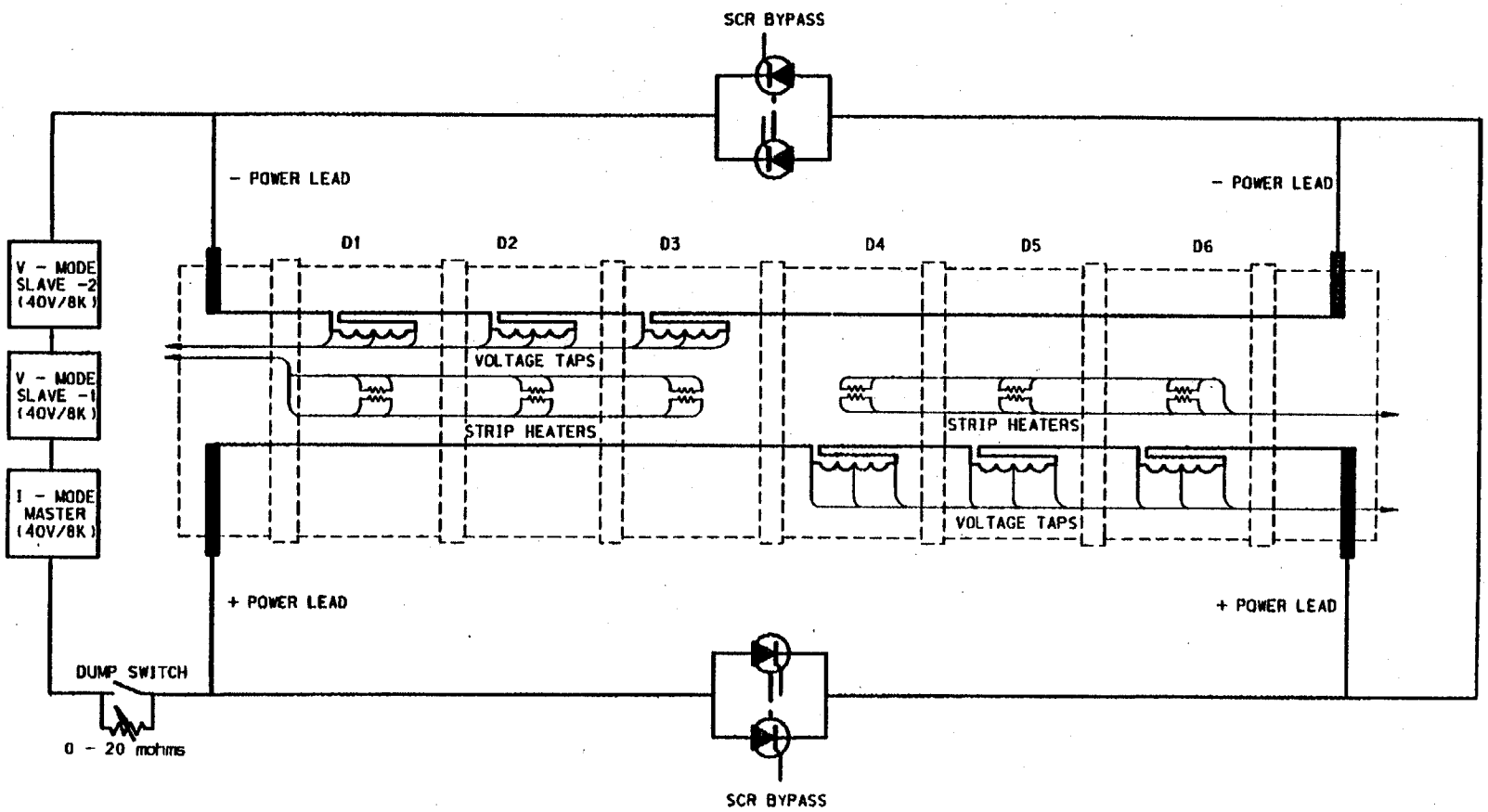

Fig. 4.4 The power supplies and quench protection schematic for the six-magnet string.

4.7.1 Beam Tube System

The beam tube installed in the ASST style magnets has an ID of 42 ± 0.14 mm. This has been verified for each magnet by passing a 41.02 mm ball through the beam tube to check for obstructions. There is no curve or sagitta in the ASST magnets. However, the cold masses are known to have some sag associated with them and the beam tube position can vary within the 50 mm aperture of the dipole. The amount of this sag needs to be measured prior to installation in this experiments string in order to adjust the survey and alignment to provide for the maximum clear aperture from end to end.

The ultimate vacuum attainable in the beam tube has serious consequences to this experiment. The impact of the Cotton- Mouton effect (discussed in Section 7.1) means that the vacuum in the beam tube may need to be better than 10^{-12} torr. Because of the as yet unknown impact of scattered laser light on the photodesorption of H_2 in the beam tube, and in order to provide the best vacuum, a beam tube vacuum pump out port will be provided at each interconnect region. This pump out port module will be inserted into the beam tube circuit in the interconnect and may also provide for baffling to reduce scattered light. This is subject to further investigation.

This experiment will need several high precision residual gas analyzers which can measure gas concentrations down to 1 ppm to monitor the beam tube vacuum. Several of these exist in the ASST equipment inventory at the SSCL.

4.7.2 Optical Access to Magnet Bore

The magnet string feed and end cans provide for the interface between the power and cryogenic systems to the magnets. In this experiment, the optical interface to the magnet beam tube (magnetic field region) will be through the feed and end cans. The beam tube is continuous through both devices and terminates at a flange on the back side. The beam tube has an 80K heat intercept to minimize heat transfer from the outside to the 4K magnet system. This interface needs to be defined further once the optics vacuum interface is defined.

4.7.3 Magnet Mounting System

The present magnet stands used at the ASST are not acceptable for this experiment and must be replaced. The SSCL has developed two designs which could have been used in the Collider machine. Either of these designs could be used for this experiment or an alternative developed. The basic requirement is that a straight line reference be established through the magnet bore and that each magnet is aligned along this reference to maximize the clear aperture of the beam tube for the optical system while maintaining the magnetic field alignment required. The desired minimum clear aperture is 38 mm. An unknown requirement on the mounting system at this time is the level of vibration isolation that must be provided. This is somewhat site specific but also depends on the mechanical response of the magnet system to external vibrations. Data are available on this from collider related studies but the impact of vibrations on this test is much different from the impact on an accelerator. This is subject to further study once a site is selected for this test.

4.8 Technical Risks and Mitigation

Each of the magnets selected for use in this experiment have been subjected to single magnet testing at some point over the past 4 years. In addition, some have been used in the ASST magnet string and their integrated system behavior is known. Whenever a new magnet string is assembled, a commissioning process is required to insure that all protective systems are operational and that the systems required for normal operation do function as expected. It is during this commissioning testing period that the operational envelope of this magnet string will be determined. That is, can this system be operated at 3.8 K, and ramped between 1000 A and 6000 A at a rate of 100 A/s continuously for several days at a time. This needs to be accomplished within the first two years of this effort in order to impact the design of the interferometer systems. Some information on the magnet operating envelope will be gained from additional single magnet testing at an early part of this project. During the string commissioning a number of system related tests need to be done. These include; vibration studies to determine the noise background, beam tube motion studies as it relates to light scattering, beam tube vacuum studies and more precise measurement of the thermal load to the cryogenic systems.

4.9 Modifications to the Magnet System

As discussed earlier, the interconnect region will be modified to provide for a beam tube vacuum pumpout port at each interconnect. As a contingency for providing additional cooling of the liquid helium circuit, the interconnect region between magnets 3 and 4 will be lengthened 1 meter to provide space to install a liquid helium recooler if required. The need for a recooler (100 W capacity) in this position will be known after the commissioning tests. The 1 meter extension is not a problem and is a low cost item. The most difficult part of the extension will be the extension of the power bus by the 1 meter since it will involve an additional splice joint. The power system for this experiment requires the inductive load be balanced between the supply and return buses. The magnets presently come in two versions. In one version, the inductive load is on the supply bus and in the other version, the inductive load is on the return bus. In the ASST, a cross over splice was developed to change one type into the other. This worked for the ASST but will not work here since the splice also changed the direction of the magnetic field in the magnet. For this experiment it may be necessary to remove the end dome from the magnet and change the internal bus wiring to convert a magnet from on type to another. If a magnet is modified in this manner, safety requirements dictate that it be put through a cold single magnet testing process to verify proper operation prior to installation in the string.

4.10 References

[1] T. Jaffery "Test Results of Post ASST design 50mm SSC Model Dipoles", presented at MSIM, SSCL Internal Tech. Note TS-SSC 92-076.

[2] M. Wake, "Ramp Rate Behavior of SSC Magnets" June 1993, SSC Technical Note MD-MKA-0-93-007

[3] T. Jaffery et al. "Test Results of Post-ASST design Fermilab-Built 1.5meter, SSC Collider Model Dipoles", IEEE Trans. Appl. Superconductivity, **2**, 666 (March 1993). 2:666

[4] T. S. Jaffery, M. Wake and W. Kinney, "Automated Methods of Field Harmoncis Extraction and Processing for The Magnets in Superconducting Super Collider", presented in International Measurement Technology Conference, Hamamatsu, Japan, May10-12, 1994.

[5] J. Strait et al.,"Mechanical Design of 2D Cross-section of the SSC Collider Dipole Magnet", IEEE Particle Accelerator Conference, San Francisco, CA, May 6-9 1991. **4**, 2176.

[6] E.G. Pewitt ed. "50 mm Collider Dipole Magnet Requirements and Specifications" Fermilab 16 Aug 1991.

[7] M. Wake, et al., "Mechanical Behavior of Fermilab/General Dynamics Built 15 m SSC Collider Dipoles", IISSC Supercollider 4, 1992.

[8] T. Ogitsu et al."Mechanical Performance of 5 cm Aperture, 15 m Long SSC Dipole Magnet Prototypes" IEEE Trans. Applied Superconductivity, **2**, 686 (March, 1993).

5. VACUUM SYSTEM

The vacuum system for the interferometer consists of three regions. The first is the magnet bore region. The second region consists of the two optical chambers at the end which house the interferometer mirrors and the optics for birefringence and polarization rotation measurements. The third region is the differentially pumped sections between the optical chambers and the magnet bore. Several considerations are important for the design of the vacuum system. The residual gas in the magnet bore can produce magnetic birefringence and rotation through the Cotton-Mouton effect and the Faraday effect, respectively. Therefore achieving ultra low vacuum in the magnet beam tube is one of the most critical concerns of the experiment. The requirement of very low scattered laser light necessitates careful consideration of the design and materials for a liner and baffles within the vacuum tube in the bore region. Light traps and additional baffles in the interconnecting region between the magnets and in the interface of the magnet string to the optical chambers are also needed. Vibration isolation of the optics and active control of the motion of the interferometer mirrors impact the vacuum in the optical chambers. Shielding the optics from background magnetic fields must also be achieved. Since the three regions have quite different vacuum requirements, each will be discussed separately.

5.1 Magnet bore region

The magnet region is cryopumped by the cold bore of the superconducting magnets. At 4.2 K the only gases remaining should be H_2 and He. Because this region has a large magnetic field, these gases could provide a systematic source of error in the optical birefringence and rotation measurements through the Cotton-Mouton (CM) effect, and to a lesser extent, through the Faraday effect. A birefringence at the shot noise limit, $\Delta n_{shot}=7\times10^{-25}$ can arise through the CM effect from a H_2 density of 2×10^6 molecules/cm^3 (8×10^{-13} torr partial pressure) within the bore tube of the magnets. Thus we take this as the design pressure for the magnet region. Although the starting base pressure in the beam tube can be better than this at 4.2 K [1], the base pressure may degrade in a short period of time due to the photodesorption of H_2 by scattered laser light and outgassing from the warmer parts of the vacuum system. The CM effect, the Faraday effect,

and the troublesome H_2 problem are discussed in detail in Section 7.1.1. The conclusions from that section are that the vacuum capability, as the ASST magnet string now stands, is far from adequate. The ASST magnets were prototype magnets and were never meant to go into an accelerator. Therefor the bore was neither heat treated nor coated. It will be necessary to add pumps in the interconnect region between the magnets to pump out some of the released gas molecules. In addition, a liner with cryosorbing material is needed to control the H_2 density. The liner also acts as a light absorber to reduce multiple scattering of light.

A larger bore (at least 10 cm in diameter) vacuum tube, containing a Ti sublimation pump and a residual gas analyzer, is to be installed in the interconnects between the dipole magnets. In this section a portion of the gases generated in the cold bore region will be pumped away and the constituents of the residual gas will be analyzed. Another important role of the large bore tube is to allow light baffles to be placed at properly designed angles so that the pump section acts as a light trap. Our design philosophy is to direct as much of the scattered light as possible into the interconnect regions between the magnets. There the magnetic field is low, absorption of stray light can be efficient on blackened surfaces, and the pumping speed is high. In this way the release of H_2 molecules within the magnet bore regions can be minimized.

5.2 Optical chambers

The vacuum requirement for the optical chambers is not as stringent as for the magnet bore region. Since the magnetic field will be shielded to a very low value in these regions, the CM and Faraday effects are not a concern. A vacuum of $\leq 10^{-7}$ torr should be adequate to keep the interferometer mirrors clean enough to maintain their low losses and to avoid significant coupling of acoustic perturbations through the residual gas in the chamber .

Each optical chamber will have a 48" diameter by 36" high UHV vacuum chamber, divided into two sections so that the top portion can be raised to allow easy access to adjustments of the optics housed inside the chamber. This chamber will be anchored to earth. The seismic vibration isolation in these chambers will be patterned after the mounting system of the LIGO (Laser Interferometer Gravitational-wave Observatory) project. As illustrated in Fig. 5.1, all the

birefringence and rotation measuring optics are mounted on an inertial platform which is vibrationally isolated within the vacuum from a set of four support beams. The support beam are in turn isolated from the ground by stacks of rubber/steel plate isolation mounts (Fig. 5.1). Soft bellows provide the vacuum seal around the support beams. This passive isolation arrangement ensures that rapid ground motion is not transmitted to the optics and the interferometer mirrors attached to the inertial platform. Each interferometer mirror will be suspended from a platform with a means for active control of the mirror's axial and tilt positions. The laser beam enters the vacuum chamber through an optical fiber. It is desirable to have no optical windows between the interferometer mirrors in order to minimize loss and scattering in the high-finesse interferometer cavity.

The optical chambers will be pumped out initially with a turbopump. The operating pressure will be maintained with vibration-free ion and Ti-sputter pumps. Even with the large number of optical components and associated servo control wiring, a pressure of $\leq 10^{-7}$ torr should be readily achievable in the optical chambers. With specially designed optical components, such as electro-optic and acousto-optic modulators, Faraday rotators, optical mounts and translation stages, and by paying attention to the choice of material for wiring and vibration isolation platforms, it is not unreasonable to expect that a vacuum of 10^{-9} torr can be achieved. The extensive experience of the LIGO project is this area will be an advantage.

5.3 Differentially pumped regions

A transition region must be provided between the room temperature optical chambers at 10^{-7} to 10^{-9} torr and the ultra-high vacuum region ($\leq 10^{-12}$ torr) of the magnet cold bore. This will be provided by a series of differentially pumped sections. The primary concern is molecules which travel down the center of the bore on ballistic trajectories. The mirrors serve as obstacles, blocking the direct paths of gas molecules from the optical chambers to the bore. The gases generated in the interface region will be pumped by small ion pumps and large area getters from Ti sublimation pumps or other materials. The proper design and performance of this transition region is critical to the success of the experiment.

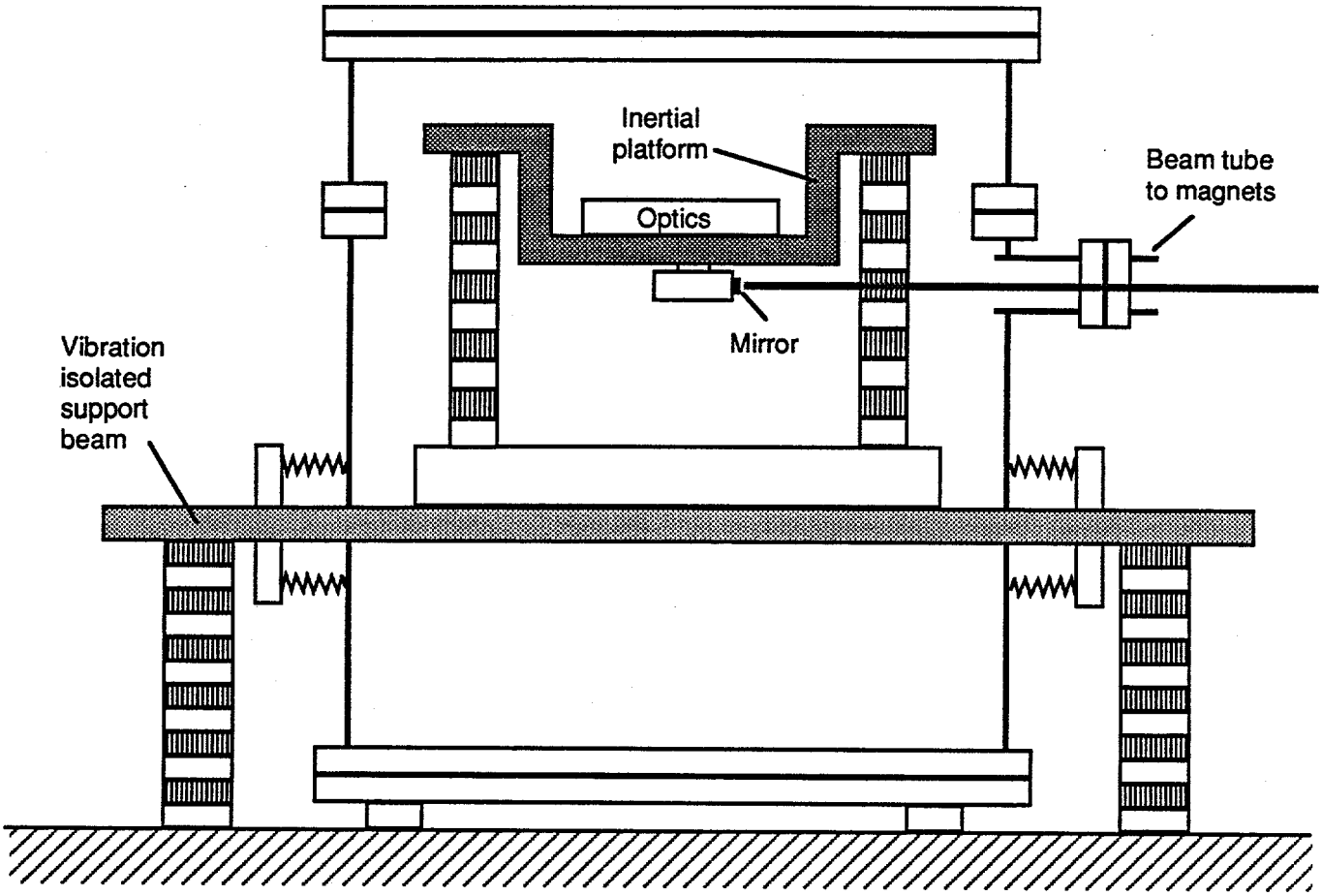

Figure 5.1 Proposed seismic vibration scheme for the optical platforms at each end of the magnet string.

5.4 References

[1]. William Turner, private communication.

6. FACILITIES AND ENVIRONMENTAL CONTROLS

6.1 Space and environment requirements

6.1.1 Magnet string enclosure

A building 110 m long, at least 3.1 m wide and 3.1 m in height is required to house the string of six 15 m SSC dipole magnets with cans and interconnects. Ground vibration noises from compressors, machinery, traffic, and site activities should not exceed more than twice of that of a "quiet" laboratory environment (Fig. 7.3). The temperature in the string enclosure needs to be maintained to better than ± 3 °C. There is no requirement on the cleanliness of the air in the string enclosure.

6.1.2 Optics laboratories

The optics laboratories will be located at each end of the string enclosure building. They house the large vacuum optical chambers, the optics and/or the laser, and associated electronics for control and detection. The input side optics lab will be referred to as # 1 and the output side optics lab as #2. These two labs have different space requirements. Lab #1 will be the primary laboratory for the experiment. A clean room is needed in Lab #1 for optics assembly and inspection.

Lab #1

Floor space:	Minimum 1000 ft^2, at least 25 ft wide, with a 6 ft by 8 ft clean room.
Height:	At least 12 ft high, with a 1 ton crane and crane rail over the vacuum chamber.
Temperature stability:	± 0.5 °C in the area of the optics vacuum chamber, ±2 °C over the remainder of the lab.
Dust specifications:	Clean room: Class 10 Remainder of Lab: approx. Class 10,000.

Lab #2

Floor space:	Min. 500 ft^2, at least 25 ft wide.
Height:	At least 12 ft high, with a 1- ton crane and crane rail over the vacuum

chamber.

Temperature stability: ± 0.5 °C in the area of the optics vacuum chamber, ±2 °C over the remainder of the lab.

Dust specifications: approx. Class 10,000.

6.2. Cryogenics requirements

Nominal He flow of 100 gm/s, at an inlet temperature of 3.8 K and pressure of 4 atm. is required. Lower flow rate and/or higher (4.35 K) inlet temperature may be acceptable, but may result in degradation of ramp rate performance. He gas at 20 K and LN_2 at 80 K are needed for maintaining the 80 K and 20 K shields of the magnets, respectively. Amounts needed are typically from boil-off.

7. IMPORTANT SYSTEMATIC EFFECTS AND THEIR MITIGATION

In Section 3.7, the shot-noise limited performance of the system is calculated. However, systematic effects will clearly affect the measurements. In this section we will analyze the two most important systematic effects, i.e. the residual gas and seismic effects, their contribution to the system noise, and possible mitigation.

7.1 Effects of residual gas

7.1.1. Cotton-Mouton effect

In a strong magnetic field, isotropic substances show a birefringence when light is propagated through them in a direction perpendicular to the magnetic field. This phenomenon is known as the Cotton-Mouton (CM) effect [1]. Experimentally, it is found that the difference in the index of refraction for light polarized parallel and perpendicular to the magnetic field direction is:

$$\Delta n \equiv n_{\parallel} - n_{\perp} = C\lambda B^2 \qquad (7.1)$$

where C is the CM constant, λ is the wavelength of light, and B is the magnetic field. In a gas, the CM constant varies with the gas density and the temperature. For a diatomic molecule, the dependence is $C \propto \rho/T$, where ρ is the gas density, and T is the temperature. The 1/T dependence is due to the thermal agitation of the partially aligned induced dipoles. For gases such as helium, in which the "molecules" are spherical, the Cotton-Mouton constant depends only on ρ.

The Cotton-Mouton effect introduces a magnetic birefringence signal which, for a given gas density, is indistinguishable from the desired QED and possible axion signals. This is a very troublesome aspect, and we consider it to be the most serious of the systematic effects. In principle one can go to as low a gas density as is possible to minimize the CM effect. The SSC magnets have a cold bore at 4.2 K, so that almost all gases except He and H_2 will be cryopumped away. This cold bore is a mixed blessing. On the one hand, it is an extremely efficient pumping

surface so that the gas density is low. Recent measurements from CEBAF [2] showed that the density is less than 10^6 molecules/cm^3, corresponding to a pressure of 5×10^{-13} torr at 4.2 K. On the other hand, the low temperature in the bore may increase the CM constant significantly. Thus we need to evaluate the density limits allowed for He and H_2, and to consider the mechanism of H_2 production in the beam pipe.

Experimentally measured values for the Cotton-Mouton constant at 0°C and 1 atm are: $C(He) = (3.5 \pm 0.7) \times 10^{-20}$ G^{-2} cm^{-1} with 514.5 nm light [3], and $C(H_2) = (1.9 \pm 2.3) \times 10^{-18}$ G^{-2} cm^{-1} with 546.1 nm light [1]. The calculated value for $C(H_2)$, based on measured electric polarizability and the anisotropy of magnetic susceptibility of H_2, is 1.3×10^{-18} G^{-2} cm^{-1} [1]. We will use the calculated value for H_2 in our estimate, since the experimental result is inconclusive.

The Δn contribution from the CM effect must be kept below the projected experimental shot noise limited sensitivity. For our proposed 0.5 % QED experiment, $\Delta n < 7 \times 10^{-25}$ for an effective B^2 of 35 T^2. For room temperature, the allowed H_2 concentration is $\rho(H_2) < 7.7 \times 10^7$ cm^{-3}. This corresponds to a room-temperature partial pressure of 2×10^{-9} torr. Converting the CM constants for He and H_2 to 4 K, and using a wavelength of 532 nm, the densities of the two gases should be ρ (He) $< 4.2 \times 10^7$ cm^{-3}, and ρ (H_2) $< 1.1 \times 10^6$ cm^{-3}. Corresponding partial pressures for He and H_2 are 1.8×10^{-11} torr and 5×10^{-13} torr, respectively, and the pressure values are for 4.2 K. The He does not present a problem unless there is a leak. On the other hand, H_2 is continuously generated in the vacuum system. One source is from outgassing of the stainless steel surfaces in the room-temperature vacuum end chambers, and the other is from photodesorption as scattered laser light strikes the wall of the cold bore.

The first problem, i.e., outgassing from the room temperature walls, can be mitigated by maintaining an ultra high vacuum $\leq 5 \times 10^{-11}$ torr in the differentially pumped region adjacent to the cold bore. This pressure is within the capability of current UHV technology using Ti sublimation pumps. These will be placed immediately at the two ends of the magnet string to shield the cold bore from the H_2 generated in the warm region. Several different pumping stages will allow operation of the mirror and optics chambers in the comfortable ~ 10^{-7} torr domain.

The photodesorption of H_2 can be a serious problem. This is a problem of real concern for the next generation of large accelerators where significant intensities of synchrotron radiation will be present in the cold bore of superconducting magnets. In our case we are not worried about the heat generated because the photon energy is low. Rather, we are concerned about the density of H_2 in the gas phase. Studies had been carried out for cold beam tube photodesorption effect for the SSCL 20 TeV Collider, at a synchrotron radiation critical energy of 284 eV [4]. Room temperature photodesorption measurements have been performed at CERN for synchrotron radiation having critical energies from 12.4 eV to 284 eV [5]. These studies showed that even though the photon energy is only 2.33 eV in the proposed experiment, photodesorption effect is likely to be important and should not be neglected.

As an estimate we use the measured results and the model calculation of Ref. 4 for 284 eV photons. This will likely be an over-estimate of the effect for 2.33 eV photons. The results of the model calculations of H_2 density versus photon exposure, based on measurements in a 4.2 K cryosorbing beam tube, are shown in Fig. 7.1. The top plot (Fig. 7.1a) is for photodesorbed H_2 with an average velocity corresponding to 4 K. The bottom plot (Fig. 7.1b) is for average velocity corresponding to ~ room temperature, because there is some evidence that H_2 comes off the surface with that velocity. The range of these velocities has enormously different consequences for the vacuum requirement. For case (a), there are no surprises. The photodesorption of physisorbed H_2 (component (2) in the figure) will be the dominant contributing factor. If the H_2 density is to be $< 10^6$ /cm^3, the total exposure allowed is about 6 x 10^{17} photon/m for the Cotton-Mouton effect to become detrimental.

The total amount of scattered laser light per mirror for a 5 kW intracavity circulating power and 5 ppm loss on each mirror is 6.7×10^{16} photons/s. If this power is absorbed uniformly throughout the magnet bore, the photon flux from scattering from both mirrors is 1.5×10^{15} photons/s/m. This means that for 4.2 K H_2, we have a run times of 8 minutes before the H_2 density becomes intolerable for a 0.5% QED experiment, and then it will be necessary to warm up the bore to pump out the hydrogen. This is certainly unacceptable. Solutions to mitigate the photodesorption of hydrogen in the cold bore region will be described shortly.

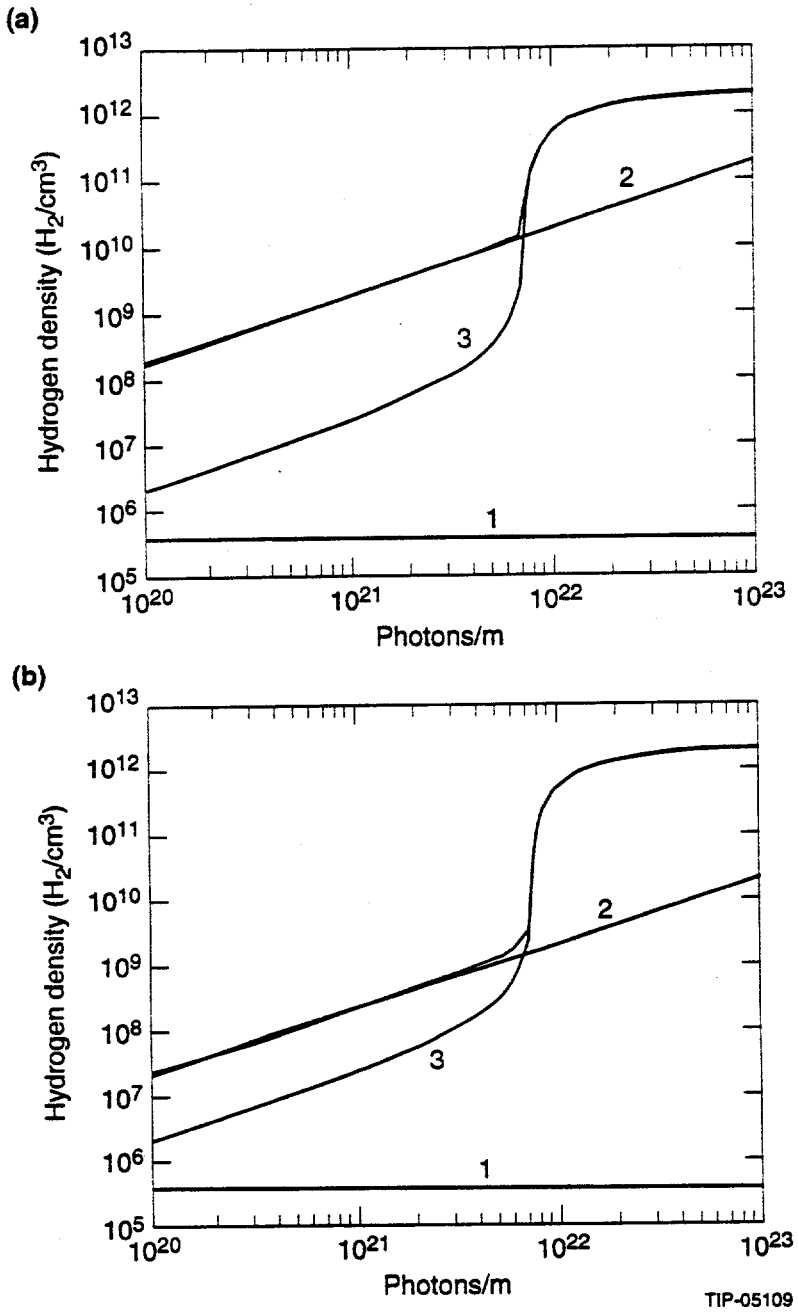

Fig. 7.1 Model calculations of H_2 density versus photon exposure in a cryosorbing beam tube; (a) v = 2.1 x 10^4 cm/s and (b) v = 1.8 x 10^5 cm/s. The three density components shown are (1) photodesorption of tightly bound H_2, (2) photodesorption of physisorbed H_2 and (3) the H_2 isotherm. From Ref. 4

On the other hand, suppose the photodesorbed H_2 moves with room temperature thermal velocity. Since the mean free path is basically the dimensions of the vacuum system, these "hot" H_2 molecules will contribute to the CM effect as if they were in a room temperature environment. We now have the best of two worlds. Extrapolating Fig. 7.1(b) to the allowable (room temperature) density value of 7.7×10^7 /cm^3, the photon exposure becomes 2×10^{21} /s/m, and the run time increases to 15 days!

Because the two results are so vastly different in their impact to the experiment, the velocity distribution of photodesorbed H_2 by 2 eV laser light should be measured. Laser spectroscopic techniques, such as two photon or Raman spectroscopy, can be used to measure the velocity distribution unambiguously. This measurement can either be done by this group or other groups in the laser/surface science community. Since at this stage we are unsure of the extent of the Cotton-Mouton "damage", we have listed mitigation for the worst case scenario:

1. Insert Ti sublimation pumps in the inter-connect region between the dipole magnets to help pump out some of the desorbed hydrogen. Place residual gas analyzer (RGA) at same location to analyze the gas content of the bore. This does not completely solve the H_2 problem. One motivation is for having RGA's throughout the magnet bore region. If the pressure of the H_2 rises, we expect to see an increase in the birefringence signal. It is then possible to correlate the increase of the signal with the increase of the H_2 density measured by the RGAs. Another motivation for putting in a pumping section in between the magnets is that it will help to mitigate the scattered light problem.

2. Design baffles and light traps so that the scattered light is absorbed in the interconnect pumping regions or in the end feed can region where the magnetic field is low. Pumps will be used to straddle these regions to prevent H_2 from diffusing into the cold bore regions.

3. Use a liner material in the cold bore [6]. The liner is a coaxial perforated tube fitting inside the magnet bore tube and serves two functions: The physisorbed molecules accumulate behind the liner and stay out of view of the photons. The surface morphology of the liner can be shaped (for example, by grooving) to reduce phase noise due to scattered light. Note that in

this case there is no need to worry about beam instabilities as in a particle accelerator, so that a liner can be designed with sufficient number of holes to ensure that the equilibrium H_2 density is kept below 10^6 /cm^3. A partial liner could be formed by sections of high purity graphite which serves the dual purpose as a distributed light absorber and in-situ cryopump of H_2.

4. The ASST magnets were prototype magnets used for testing and not for actual usage in an accelerator. Therefore the beam tube was not heat-treated or plated. A combination of N_2 and Ar 10% O_2 glow discharges should be run along the magnet bore prior to cool down to clean the surface of the stainless steel. Studies indicate that this combination appears to be the most effective method in reducing photodesorption and enhance the lifetime between warmups of the magnet [7].

The implementation of the steps above should allow the lifetime between warmups to be increased to a more reasonable length of time. Note that photodesorption is only important when the Fabry-Perot cavity is actually in resonance. It is not important during most of the testing and setup studies.

7.1.2. Faraday effect

When linearly polarized light propagates through a material in the presence of a magnetic field, there is a rotation of the plane of polarization when the magnetic field has a component along the light propagation direction. This effect is known as the Faraday effect. The angle of rotation of the polarization is given by

$$\epsilon = VlB \qquad (7.2)$$

where V is the Verdet constant of the material, l is the length and B is the magnetic field. The Faraday effect will affect the axion measurements but not the QED measurements. Again we will consider H_2 in the cold bore of the magnet. The Verdet constant depends linearly on the gas density. At 0°C and 1 atm, the Verdet constant for H_2 with 578 nm light is $(6.2\pm0.9)\times10^{-6}$

min/cm-G [7]. For an H_2 density of 10^6 /cm^3, the Verdet constant is 6.7×10^{-21} rad/m-G. Therefore the B field component along the magnet bore should be less than 500 G to keep the Faraday rotation below 3×10^{-16} rad.

Since the Faraday effect is linear in the magnetic field, the rotation changes sign when the magnetic field direction is reversed. Therefore the longitudinal fringe fields due to the ends of the magnets would cancel out in a first approximation, so would symmetric sags in the magnet cold mass. Any residual Faraday rotation can be studied by reversing the direction of the magnetic field. In the SSC magnet string, this can be accomplished in several ways. One can use a switching power supply where the current direction is changed in the supply, or external switches can be set up to do the same task. A third way is simply to reverse the power leads to the feed can. However, if the switching needs to be done often, then the first two methods are better.

7.1.3 Photon-Axion Phase Matching

It has been suggested that adding a gas in the magnetic field region may help to improve the axion detection sensitivity [9-11]. Here we look at this topic in more detail. The optical birefringence and rotation generated by photon-axion scattering in a magnetic field are coherent processes, like frequency doubling or mixing in nonlinear optical materials. Thus the signal produced is large as long as $\Delta k\, l = (k_\gamma - k_a)\, l < \pi$, where l is the length of the magnetic field, and oscillates with decreasing amplitude for $\Delta k\, l > \pi$, see Fig. 2.4. For the optical photon in vacuum, $k_\gamma = \omega_\gamma$. On the other hand, the axions follow a dispersion relationship of the form

$$k^2 = \omega^2 - m^2 \qquad (7.3)$$

relevant for massive particles. Thus $k_a < \omega_a$. For visible photons ($\omega_\gamma \approx 2$ eV), the relation $\Delta k l < \pi$ imposes a limit on high sensitivity searches for axions of $m_a < 1.6\times10^{-4}$ eV. This is in fact the mass at which the peak in the curve for birefringence occurs and is also the knee of the flat region for optical rotation in Fig. 2.4.

Since $\omega_a = \omega_\gamma$ in the case of a static magnetic field, phase matching of the photon and axions beams can only occur if $k_\gamma < \omega_\gamma$. In a medium this can only occur if the index of refraction is less than 1. There are two important optical regimes where index $n < 1$: (i) on the high frequency side near an optical transition in the gas, the so-called anomalous dispersion region and (ii) when the photon energy is sufficiently far above all the resonances of the gas, so that the index of refraction is slowly rising and approaching 1.

It was pointed out by Raffelt and Stodolsky [9] and by Van Bibber et al. [10] that in searches for solar axions in the keV range, photon-axion coherence may be maintained over long distances by filling the interaction region with a gas such as helium. Since in those experiments the photon energy is far above the highest resonance (ionization energy) of the buffer gas, condition (ii) is satisfied in He. In a recent paper, R. Stroynowski and A. R. Zhitnitsky suggested that He can also be used with photons of 1.17 eV ($\lambda = 1.06$ μm) to maintain a photon axion coherence in magnetic birefringence and rotation experiments [11]. Unfortunately this suggestion is erroneous because neither condition (i) nor (ii) is satisfied for gases which could be used in the experiment.

To see this point more clearly, we start from Maxwell's equations and solve for the dielectric constant $\varepsilon(\omega)$ of a simple substance such as a gas, as a function of the incident photon frequency ω. [12]. We note that the index of refraction n is related to the dielectric constant by $n^2 = \varepsilon$. The dielectric constant is given by

$$\varepsilon(\omega) = 1 + \frac{4\pi N e^2}{m} \sum_j \frac{f_j}{\omega_j^2 - \omega^2 - i\omega\Gamma_j} \qquad (7.4)$$

where N is the density of the gas, and the summation is over all allowed electric dipole (E1) transitions, with ω_j the resonance frequency and Γ_j the width of the jth transition. The oscillator strength f_j is of order unity.

In general, Γ_j is small compared to ω_j , so that $\varepsilon(\omega)$ is approximately real for most frequencies. Away from resonances, the factor $(\omega_j^2 - \omega^2)$ is positive for $\omega < \omega_j$ and negative for $\omega > \omega_j$. Thus at low photon energies, below the smallest transition frequency, the dielectric constant, and hence the index of refraction, is always positive.

For very high photon frequencies, $\omega >> \omega_j$, the dielectric constant takes on the form

$$\varepsilon(\omega) \approx 1 - \left(\frac{4\pi Ne^2}{m}\right)\frac{1}{\omega^2} = 1 - \frac{\omega_p^2}{\omega^2} \qquad (7.5)$$

where $\omega_p = (4\pi Ne^2/m)^{1/2}$ is known as the plasma frequency. In this case the photons follow a dispersion relation of the form given by equation 1, where the role of m is played by the plasma frequency.

For He, the lowest transition from the ground state is the 1^1S_0 to 2^1P_1 transition at 59.14 nm (21.3 eV), and the ionization energy is (24.6 eV). Therefore for the keV x ray photons considered by Van Bibber et al., helium has a dielectric constant less than 1, and photon-axion mixing resonance can occur. On the other hand, visible and infrared photons have energies on the order of a few eV, so the dielectric constant is always greater than 1. As a result, *photon-axion phase matching is not possible in the visible and infrared region for He.* The wrong conclusion of Stroynowski and Zhitnitsky comes about because they have applied the results derived for x rays to the infrared case.

The measured index of refraction of He in the visible region follows the dispersion formula [13]

$$n = 1 + 3.48\times10^{-5}\left(1 + \frac{2.3\cdot10^{-5}}{\lambda^2}\right) \qquad (7.6)$$

where the wavelength λ is measured in Angstroms. The experimental result further confirms that the dielectric constant is indeed larger than 1 and phase matching can occur.

It is possible to find other gases of which the index of refraction is less than 1 in specific

regions of the visible or infrared. For example, most alkali (Na, Li, etc.) and alkaline earth (Ca, Ba, etc.) atoms have discrete visible transitions, and molecules such as I_2 have transitions every 10 GHz or so throughout the whole visible regions. It is possible to select laser frequencies to produce negative dispersion for these gases. Unfortunately in the cold bore of the superconducting magnet, the only gases that can survive the cryopumping are He and low density of H_2. Neither of these are suitable for the laser interferometer because their lowest resonance frequencies are in the VUV region.

7.2 Effect of Seismic Motion on Scattered Light

Light hitting a mirror may be scattered out of the main beam of the interferometer. This scattered beam may in turn make its way back into the beam by reflection or scattering off the walls or baffles of the surrounding beam pipes. The scattered beams travel a different path length relative to the main beam and contribute a phase shift to the main beam signal. The scattering phase shift oscillates as the beam pipe is moved from seismic effects and acoustic perturbations. Thus the scattered light contributes a phase noise which can severely degrade the system performance of the interferometer.

The scattered light problem of the proposed interferometer is similar in its difficulty to that encountered in the laser interferometer for gravitational wave detection (LIGO project [14]). Many of the results [15] that are calculated for the LIGO project are directly applicable here. Because of the small bore of the SSC magnets (diameter ~ 4 cm), the stray light scattering is a particularly troublesome problem in the proposed interferometer, and its solution will require the same care that is afforded the LIGO.

7.2.1. Reflection from Pipe Walls

A process for scattered light to recombine into the main beam mode is for the main beam mode light to be scattered from one mirror. The scattered light then travels down the pipe, reflects at least once off the pipe walls, reaches the other mirror, and scatters back into the main beam. Since the reflectivity of the pipe walls are large only at grazing angles of incidence,

baffles are generally used to force the light-beam to reflect off at a large light-beam pipe angle, so that in general the light will have to undergo many reflections as it travels from one end of the pipe to the other. The larger the number of reflections, the more likely the light will be scattered away and be absorbed by the walls.

Ideally the walls and baffles should be deliberately blackened to lower the reflectivity and increase light absorption. The bore of the SSC magnets is made of unpolished stainless steel. One solution to decrease the reflectivity is to introduce a liner or sleeve into the bore. The material and surface topology of the liner would be chosen so that the liner becomes a distributed light baffle throughout the bore. The liner also serves to reduce the photodesorption of H_2 in the cold bore - a topic that is important for the Cotton-Mouton effect discussed in Section 7.1.1.

7.2.2. Motion of Beam Tube

An unavoidable source of vibration for the beam pipe is due to seismic effects. The amount of seismic motion is site dependent and the actual value must be measured. Nevertheless it is possible to obtain an estimate of the effect of ground noise. Fig. 7.2 shows the spectral density of power of the vertical seismic displacements measured at the SSC site [16]. At frequencies above 100 Hz, the vertical displacement has an approximately $1/f^2$ dependence. The displacement levels off somewhat between 1 - 100 Hz, and increases below 1 Hz due to the microseismic peak. At 1 Hz, the vertical motion at the SSC site is ~ 3×10^{-9} m/$\sqrt{\text{Hz}}$. This type of displacement is fairly typical of a laboratory [17], see Fig. 7.3. Although no horizontal displacement data of the SSC site are available to us, we expect that the horizontal motion is about the same order of magnitude [18].

Analysis from LIGO shows that the phase noise is mainly due to the back scattering from the first set of baffles [15]. The sensitivity limit due to horizontal motion is expressed in terms of the square root of the spectral density of noise h(f), in units of "strain per root Hz". For our experiment, $h(f) = \Delta L/L = \Delta n/n$. The noise is [15, 19]

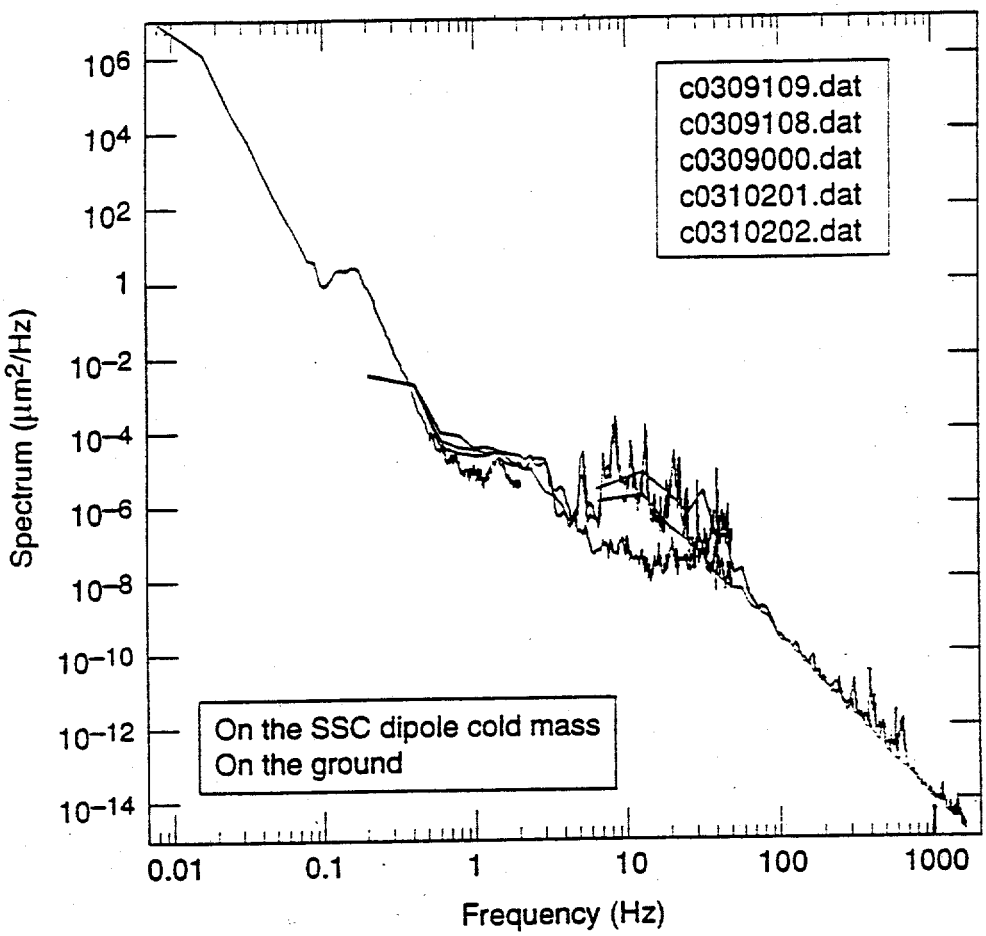

Fig. 7.2 Measured spectral density of power of vertical vibrations in a very broad frequency band of 0.07-1720 Hz at the SSC site. From Ref. 16.

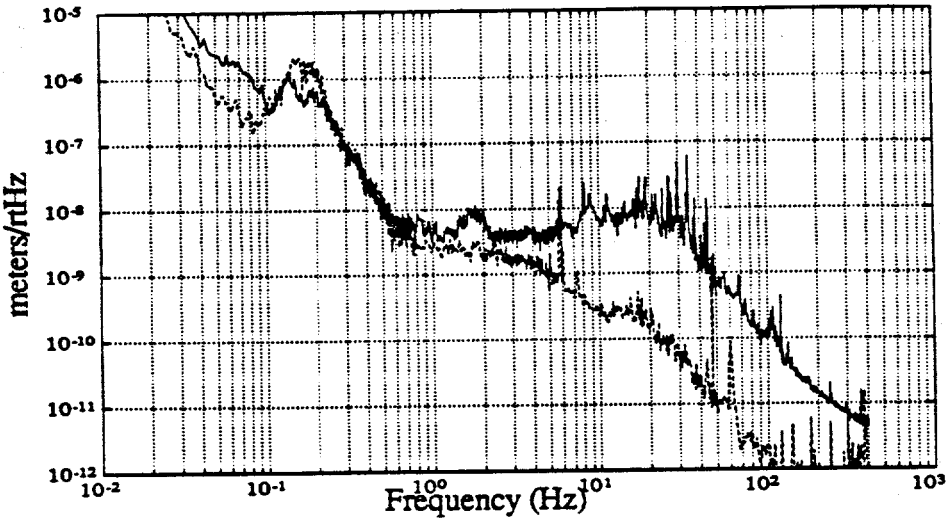

Fig. 7.3 Measured spectral density of amplitude of vertical seismic motion. Solid curve is lab # B042 of JILA at the Univ. of Colorado, Boulder. Dashed curve is Building 8 of NIST, Boulder. This is considered to be a "quiet site".

$$h(f) \approx 4\alpha \sqrt{\ln\left(\frac{L}{l_1}\right)} \frac{\lambda}{Y} \sqrt{\frac{d\sigma}{dA d\Omega}} \frac{\xi(f)}{L} \qquad (7.7)$$

The above equation assumes that the scattering probability of main-beam light from an interferometer mirror into unit solid angle around a direction that makes an angle θ with the normal of the mirror follows the form $dP/d\Omega = \alpha/\theta^2$. For our interferometer geometry and a 5 ppm loss mirror, $\alpha \approx 7.7\times10^{-8}$. L is the length of the cavity (110 m), l_1 is the distance from the mirror to the first set of baffles (10 m), λ is the wavelength (532 nm), and Y is the distance from the center of the main beam to the nearest baffle edge, $Y \geq 1$ cm. $d\sigma/dAd\Omega$ is the scattering probability from the baffle surfaces, and is ~ 10^{-2} for most wall materials. $\xi(f)$ is the square root of the spectral density of fluctuational displacements of a typical point on a typical baffle. For an estimate we will assume that the beam pipe and baffles are sufficiently well-anchored so that $\xi(f)$ is on the order of the seismic noise.

Vertical motion of the beam pipe can also introduce noise into the system. If $\xi(f)$ is now the square root of the spectral density of vertical displacements, the noise is estimated to be [15]

$$h(f) \approx 4\alpha \sqrt{\ln\left(\frac{L}{l_1}\right)} \frac{\lambda}{l_1} \sqrt{\frac{d\sigma}{dA d\Omega}} \frac{\xi(f)}{L} \qquad (7.8)$$

The noise contribution to the sensitivity of the interferometer due to a $\xi(f)$ of 3×10^{-9} m /$\sqrt{}$Hz is

Horizontal motion:	$\leq 7 \times 10^{-23}$ /$\sqrt{}$Hz
Vertical motion:	$\leq 7 \times 10^{-26}$ /$\sqrt{}$Hz

The horizontal motion contributes a noise that is a factor of 3 less than the shot-noise limit of the proposed interferometer, and is potentially a serious problem. The vertical motion can be neglected safely.

It is highly desirable if one can increase the frequency of modulation for the detected signal. For example, choosing f = 100 Hz will alleviate the problems associated with ground motion. However, this conflicts with the long storage time of the high finesse Fabry-Perot cavity.

However a compromise between finesse and modulation frequency should be possible, especially by using an asymmetric cavity in which the finesse is lower without sacrificing the sensitivity.

7.2.3. Recommendations Regarding Scattering

The calculations above show that scattered light can be a potentially dangerous limiting factor for the proposed experiment. Very carefully designed baffles are definitely needed to suppress as much as possible the scattered light from recombining into the main beam mode. A problem here is the smallness of the SSC magnet bore diameter. There is not enough room to put in baffles of the right height for stray light suppression. A baffle height of at most 0.9 cm can be used in order not to introduce diffraction losses that are comparable to the mirror losses into the Gaussian beam mode of the propagating laser. As a first design, the first set of baffles would be placed at a distance of 10 m from the mirrors. Ideally, subsequent baffles should be placed at the anchor point of each magnet. This is to ensure that the motion of the baffles is controlled by the ground alone, and not by other effects such as ramping of the magnetic field. Again this may not be possible. The use of a liner as a distributed light scatterer/absorber looks promising and warrants serious considerations.

The above calculations are at best an educated guess of what the scattering noise may be. We have not included the scattering due to the flexure motion of the interferometer, and we have not considered the diffraction aided reflection off the baffle edges. Therefore it is imperative that a numerical analysis of the stray light problems in the interferometer be carried out as early as possible. Programs such as APART and GUERAP could be employed to determine the phase noise that will be introduced due to ground or other motions. These Monte-Carlo programs will also allow for optimization of baffle or liner and light trap placements/configurations. As input to the numerical simulations, it will be necessary to know the vertical and horizontal seismic motions of the experimental site, the effect of magnet ramping, and the bidirectional scattering functions of the beam pipe and possible liner/light trap materials. This would argue for setting up the full 6-magnet string in the experimental site as soon as possible, to allow these parameters to be investigated. We have explored the possibility of doing such a calculation with BRO, Inc. in Tuscon, Arizona. The cost of a numerical calculation is on the order of $40,000. The high

cost is associated with the extremely small phase signal that we are detecting, and the need to calculate the two polarizations separately.

7.3 References

[1]. A. D. Buckingham, W. H. Prichard and D. H. Whiffen, Trans. Faraday Soc. (London) **63**, 34 (1967).

[2]. William Turner, private communication.

[3]. R. Cameron, et al., Phys. Lett. A **157**, 125 (1991).

[4]. V. Anashin et al., "Cold beam tube photodesorption and related experiments for the SSCL 20 TeV proton collider", SSCL Preprint-533, (March, 1994).

[5]. J. Gómez-Goñi, O. Gröbner and A. G. Mathewson, "Comparison of photodesorption yields using synchrotron radiation of low critical energies for stainless steel, copper and electrodeposited copper surfaces", to be published.

[6]. W. C. Turner, "Dynamic vacuum in the beam tube of the SSCL collider - cold beam tube and liner options", SSCL-preprint-404, (May 1993).

[7]. T. Kobari and H. J. Halama, J. Vac. Sci. Tech. **5**, 2355 (1987).

[8]. *American Institute of Physics Handbook*, ed. Dwight E. Gray (McGraw Hill, 1957), p **6**-91.

[9]. G. Raffelt and L. Stodolsky, Phys. Rev. D**37**, 1237 (1988).

[10]. K. Van Bibber, et al., Phys. Rev. D **39**, 2089 (1989)

[11]. R. Stryonowski and A. R. Zhitnitsky, "Axion search with optical technique", preprint SMU-HEP-94-12.

[12]. J. D. Jackson, *Classical Electrodynamics* (Wiley, New York, 1975), 2nd ed., p. 285.

[13]. M. Born and E. Wolf, *Principles of Optics*, (Pergamon Press, 1975) 5th ed., p.95.

[14]. A. Abramovici et al., Science **256**, 325 (1992).

[15] Kip. S. Thorn, "Light scattering and proposed baffle configuration for the LIGO", January 1989, report #36 of list of 3/1/89.

[16]. V. V. Parkhomchuk, V. D. Shiltsev and H. J. Weaver, "Measurements of ground motion and SSC dipole vibrations", SSCL-preprint-624 (June 1993).

[17]. David B. Newell, "Six degree of freedom active vibration isolation at 1 Hz and above",

Ph. S. thesis, Univ. of Colorado, Boulder (1994).

[18]. D. C. Agnew, "Strainmeters and tiltmeters", Rev. Geophys. **24**, p.579-624 (1986).

[19]. Kip S. Thorn, private communication.

8. EVALUATION OF PROJECT RISKS AND RISK MITIGATION

8.1 Technical Risks

The technical risks associated with this experiment along with their proposed mitigation have been discussed in detail in the previous technical sections. The technical risk areas are summarized below. The numbers in parenthesis refer to the sections in which the risks are discussed.

Vacuum system

Risks

Current magnet vacuum capability is inadequate for this experiment. (4.7.1)

Beam tube vacuum degrades due to scattered light photodesorption of H_2 from the walls, leading to low operating cycle time between magnet warmups (7.1.1).

Design of differential pumping to interface the optical chamber at pressure ~10^{-7} torr to the beam tube area at pressure of $\leq 10^{-12}$ torr (5.3)

Mitigation (4.10, 5.1, 7.7.1, 7.2)

Add pump out ports in the interconnect region of the magnets.

Use a liner to reduce photodesorption of physisorbed H_2 and as a distributed light baffle. to cut down the scattered light.

Use cryosorber in the liner to help in pumping.

Several stages of differentially pumped sections.

Scatterered light

Risks

Scattered light related to seismic motion introduces phase noise into the detected signal and degrades optical system measurement capability. (7.2)

Scattered light causes photodesorption of H_2, thus degrading the beam pipe vacuum. (7.1.1)

Mitigation (7.2.3)

Careful design and placement of baffle and light traps.

Use liner in the beam tube as distributed absorber.

Use magnet interconnect pump out regions as light traps.

Clean environment to maintain the low loss of the mirrors. (3.1)

Perform Monte Carlo simulations for the system to properly evaluate the effect of beam pipe motion and to optimize baffle/light trap/absorber configuration.

Residual gas

Risks

directly related to the quality of vacuum.

The Cotton-Mouton effect has a magnetically induced birefringence with the same signature as the desired signal. (7.1.1)

Mitigation

Obtain as good a vacuum as possible in the beam tube region. Same risk mitigation as the vacuum system.

Optical system

Risks

Birefringence measurement at the 0.5% QED level requires unprecedented technical requirements in frequency metrology. (3.4)

Motion of interferometer mirrors from seismic excitations prevents initial lockup of cavity. (3.4)

Mitigation

Employ passive vibration isolation and active control of the mirror motion (3.3, 3.4, 5.2)

Proposed new scheme of birefringence measurement technique. (3.4).

Proof of principle experiment is now under way (3.5).

Magnet system

Risks (discussed in section 4)

Experiment requires ≥ 100 A/s ramp rate.

Quench current dependence of ramping a full string of magnets has not been investigated.

Motion of beam tube as a result of changing magnetic field impacts scattered light.

Power system and quench detection system need to be reconfigured.

Mitigation

Evaluate single magnet performance to select "good" magnets for the experiment. (4.2)

Upgrade power supply and quench detection system to allow ramping. (4.5, 4.6)

Assemble string for full system test to define operational envelop ASAP.

8.2 Site Associated Risks

The major risk to this project is one that the collaboration cannot control even after funding for this experiment has been secured. That risk is whether or not the Texas site for this experiment will exist as an operating facility or laboratory throughout the five year course of the proposed experiment. The proposed ASST site will be turned over to Texas (TNRLC) to do whatever the state sees fit. It was hoped that the various EOI's would provide some level of operating funds to enable Texas to maintain some form of laboratory at the old SSCL site. However, it is extremely naive to believe that this funding can fully support the infrastructure and personnel needed to form the core of an R & D laboratory without significant funding from Texas, at least in the initial five year period. As of yet, there has been no evidence that this will be forth coming. DOE has made it clear that a new national laboratory, with DOE as the primary funding agency, with any mission, will not be established at the SSCL site in the foreseeable future. The collaboration has to assume that the cryogenic refrigerator and associated systems will be maintained and operated and that those services can be purchased at the cost estimate provided by TNRLC at this point. This is a very high risk assumption. Should the State of Texas guarantee funding support to maintain the ASST and refrigerator facilities along with funding for a core group of technical personnel, then this risk factor is reduced. The remaining costs associated with this effort can be directly controlled by the collaboration since they are

either non service related, or other suppliers of the service (i.e. engineering, trades, technician and machine shop facilities, for example) are available in the immediate area or can be provided by the home institutions of the collaborators.

This site associated risk impacts schedule, total project cost and at the worst, whether the experiment can be carried to conclusion. To mitigate this risk, the collaboration has looked at other sites were this experiment can be conducted, assuming the necessary ASST equipment is available and can be transferred to the host laboratory. The primary candidate for a host laboratory for this experiment other than Texas, is Fermi National Accelerator Laboratory. There is no doubt that FNAL will exist in five years as a DOE funded laboratory who's primary mission is high energy and accelerator physics. FNAL has the infrastructure to support all magnet related aspects of this experiment. Many of the systems used at the ASST are enhancements to designs that originated at FNAL and the personnel necessary to modify and maintain these systems are on staff. This translates into an increased chance of efficiently utilizing already existing assets as opposed to replacing them or not using them at all.

9. MANAGEMENT PLAN FOR THE EXPERIMENT

The organizational structure envisioned for this experiment is fairly standard in the High Energy Physics scientific community. The collaborators who have proposed the experiment control the scientific objectives of the experiment, operate the experiment and provide the basic management of the funds and the project in general. The role of the principle investigator is to lead the collaboration and to arbitrate any internal disagreements as pertaining to the experiment. If a consensus within the collaboration cannot be reached on an issue, the principle investigator has the final decision which is binding on the collaboration. Given that most collaborators in this experiment have home institutions which are different from the host laboratory where this experiment will be conducted, there is a need for a site based group to manage the construction, installation and operation of the experiment at the host laboratory. This group is lead by the project manager, who is a member of the collaboration and in general is an employee of the host laboratory during the experiment. The project manager takes direction from the principle investigator in regards to the experiment and has the responsibility for the site based operations which includes the integration and coordination of the resources offered by the host laboratory. For this experiment, the core group is anticipated to be comprised of the project manager (scientist), an engineering physicist, a lead technician (senior engineering associate) and a technician.

The control of resources and funding obligations of all parties will be negotiated with the host laboratory and defined by a formal "letter of intent". This document will spell out in detail what resources the host laboratory will provide to the collaboration during the lifetime of the experiment. It will also detail what contributions the home institutions of each collaborator will make to the experiment in terms of equipment, labor and funds to the host laboratory. In the case of this experiment, it is anticipated that the cost of the optics and optics support systems will be provided by the university collaborators through grants to the university from the DOE HEP program or through other agencies (see section 12). The host laboratory will be expected to provide the support required to provide the magnet string, its support systems and the operational support. (This case is most probable for the Fermilab option.) If this type of cost sharing is not feasible, and it becomes the responsibility of the collaboration to provide full funding, then the

principle investigator (or as delegated to the on site project manager) shall have complete control over and responsibility for, all funds allocated to the host laboratory. (This case is most probable for the TNRLC host option.)

10. SCHEDULE OF EXPERIMENT

10.1 Introduction

There are a large number of unknowns concerning the proposal evaluation and recommendation process, the possible funding sources, and the undefined nature of the organization which will survive at the former SSCL site, which make any realistic, detailed schedule impossible to assemble at this time. The following schedule, listing key decision points and milestones, is a best estimate and assumes that the required funding and personnel will be available when needed.

The proposed duration of the project is five years. In order to complete the project in that time, most of the equipment cost for the optical and vacuum systems must be invested in the first year. The only really significant "show stopper" in the project is the possible existence of signals correlated with the magnet ramping from sources that we cannot anticipate at this time or cannot fully mitigate. Unfortunately, a test of this show stopper requires the full magnet string, laser, and 110 m interferometer. These items are not scheduled to be installed together until the third year. Since there is considerable experience in the LIGO project, the accelerator community, and in our collaboration on the other problems such as vibration isolation, laser stabilization, cavity locking, scattered light, and residual gas, we expect these areas to be only hurdles rather than impassable barriers.

Consequently we see no point in this particular situation for adopting a conservative strategy in which initial investments are small until all "show stoppers" are investigated in a test apparatus. Such a plan with a long series of intermediate steps would only lengthen the project and provide little extra protection from risks. Our plan is based on a direct attack on all major problems, including the design and construction of the optical, vacuum and vibration isolation system from early in the project. The only major intermediate steps we will be taking are (1) a series of tests with single magnets to find the optimum parameters of operation, and (2) extensive experience with a 3 meter Fabry-Perot interferometer at Colorado State/Colorado Universities before attempting to install a 110 m interferometer on the magnet string. Note the

latter is not simple a small step. The 3 meter interferometer requires almost all the proposed optical, vacuum and vibration isolation systems to be constructed and installed.

The first two years of effort are aimed at installing and testing the magnet string, designing and implementing a vibration isolation system and a method for scattered light reduction, and gaining experience with and perfecting the proposed optical system using a high-finesse cavity of intermediate length. The remaining three years are devoted to final assembly of the 110 m interferometer on the string and the actual measurements of the experiment.

10.2 Yearly milestones

Prior to project:

Select host laboratory site for the experiment.

Negotiate a "letter of intent" agreement with the host laboratory.

Develop a site specific cost estimate and schedule.

Apply for funding from appropriate sources.

Define equipment (SSCL assets) to be transferred to collaboration.

Year 1:

Disassemble ASST string and string supporting systems.

Transport equipment to host site (if other than TNRLC).

Assemble site based core group of personnel at the host laboratory.

Conduct single magnet testing to determine the operating parameters

Conduct beam tube vacuum experiments with laser light (part of single magnet testing) to determine H_2 photo desorption rates.

Initiate study to reduce scattered light in the beam tube from the mirrors.

Begin facility modifications for the experiment.

Define the vacuum system for beam tube and interferometer

Define vibration isolation for the laser interferometer.

Determine light scattering reduction requirements and method.

Determine effect of laser power and magnetic field on birefringence of the mirrors.

Begin construction of large optical vacuum chambers and 3 m test interferometer.

Conduct initial performance evaluation of electro-optic birefringence measurement scheme.

Investigate performance of lock/servo electronics and suspended mirror control system.

Year 2:

Facility modifications complete. (1Q)

Install magnet string and string support systems in the test facility. (2Q)

Measure clear optical aperture of the magnet string.

Commission string systems and magnet string for operation. (3Q)

Conduct initial string testing to define operations envelope. (4Q)

Measure the vibration environment of the string facility during magnet operation.

Determine if recooler option is necessary, if yes, begin fabrication of recooler.

Commission 3 meter interferometer.

Test vibration isolation, stray light, locking, using the 3 meter interferometer.

Conduct check out of data acquisition system for interferometer.

Determine the optical noise characteristics of the 3 meter interferometer.

Measure effect of laser power and magnetic field on birefringence of mirrors.

Build an enclosure for optics at string facility.

Year 3:

Install 110 meter interferometer and interface to magnet string.

Install recooler in string if needed.

Investigate H_2 levels in the magnet bore tube and the effect of scattered light.

Test vibration isolation, stray light, and locking of the 110 meter interferometer.

Determine the optical noise characteristics of the 3 meter interferometer.

Confirm performance of laser beam pointing control system.

Year 4:

Begin initial experimental program using magnets and interferometer.

Study systematic noise sources and noise reduction techniques.

Measure initial QED signal.

Define any modifications to experimental setup.

Make any necessary equipment modifications.

Year 5:

Make precision measurement of QED effect.

Conduct axion search.

Define any future plans for experiment

10.3 Timely allocation of SSCL resources

In order to make this schedule possible, DOE should be ready at the time the proposals are evaluated and a decision is made on the technical merit and feasibility of the experiment to allocate equipment resources from the SSCL assets that are required for the proposals and assign those assets to the collaboration. At that time the collaboration should decide on the host laboratory. DOE should provide what minimum funding is necessary to transfer the equipment assets to the host laboratory for the experiment and to the home institutions of the collaborators if the equipment is required there for preliminary testing. Without this minimum commitment by DOE, it is very likely that the some fraction of the SSCL assets will lost to this and other proposals.

11. ESTIMATED COSTS

11.1 Basis for cost estimates

The initial intent of this feasibility study was to study the use of the SSCL assets at the original site of the laboratory. The cost estimate presented here is a zeroth order estimate due to the large uncertainty of what equipment and personnel will be available at the Texas site and what type of organization, if any, will exist there. The "Texas" costs are based on a cost model developed by TNRLC personnel (D. Hatfield, W. Robinson and G. Mulholland) supporting the JPL proposal on this topic. The costs have been scaled to reflect the estimated needs of this group's efforts. The cost of the optics and optics related research have been developed by the Colorado State collaborators. It is assumed that all assets associated with the Accelerator Systems String Test (ASST) operations (along with certain other SSCL assets) will be available (at no cost) for use in this experiment and without restriction on it's use. This equipment includes all dipole magnets, magnet interconnect parts, superconducting magnet cable, sensors used in the magnets, power supplies, quench protection electronics, cryogenic feed and end cans, magnet stands, magnet transport equipment, test equipment, vacuum system equipment, the data acquisition and control systems as installed in the ASST control room trailer (T-5) and other related items. Also assumed is that the physical facility will be provided rent free during the five year course of this test along with adequate office space for non laboratory (i.e. the collaborators) personnel that will run and operate this experiment. It is expected that a detailed cost estimate will be available only after a "letter of understanding" has been negotiated between this collaboration and the host laboratory for this experiment.

A second cost estimate discussion is presented as an appendix to this proposal based on conducting this experiment at Fermi National Accelerator Laboratory. This scenario offers interesting possibilities to make use of the SSCL assets to support multiple high energy physics and accelerator physics projects in coordination with conducting this experiment. The shared cost possibilities result in a significant cost reduction to this experiment and maximizes the use of ASST related assets.

11.2. Site independent costs

11.2.1 Equipment costs - optical and vacuum systems (All costs in K$)

A. Optical interferometer:

1. Optical components

Item	Number	Unit cost	Item cost
Nd:YAG laser with doubling	1	45	45
Optical spectrum analyzer	1	6	6
Polarizing beam splitter	7	0.5	4
Electro-optic modulator	3	5	15
Acousto-optic modulator	3	1	3
KDP AM modulator	1	5	5
Polarizer	5	0.5	3
Half wave plate	6	2	12
Faraday rotator	5	3	15
Pockels cell switch	1	3	3
Photodiodes	6	0.5	3
Iodine cell	1	1	1
Prestabilization cavity	1	20	20
Spatial filters	2	4	8
Plane mirrors	20	0.5	10
Interferometer mirrors	10	1.4	14
Quad diodes	4	0.2	1
Miscellaneous optics			20
Total cost of optical equipment for interferometer:			187

2. Optical mounting hardware

Item	Number	Unit cost	Item cost
Optical table	3	15	45
Optical mounts	35	0.3	11
Interferometer mirror tilt control	2	5	10
Remote rotation stages	22	1	22
Remote steering and translation stages	30	3	90
Miscellaneous mounting hardware			20
Total cost of mounting hardware for interferometer:			198

3. Electronic components

Item	Number	Unit cost	Item cost
Signal analyzer	1	28	28
Low freq. Fourier analyzer	1	15	15
Digital storage oscilloscope	2	20	40
Digital synthesizer	2	3	6
Frequency counter	2	5	10
Locking electronics parts			100
Interfometer mirror tilt control electronics	2	5	10
Remote steering drivers	6	1.8	11
Laser power meter	1	1.2	1
Demodulator	5	0.5	3
Mixer	5	0.2	1
30 MHz VCO	1	0.4	0
x4 multiplier	1	1	1
Amplifier	3	0.3	1
Misc. monitoring electronics			5
PC Computer	1	3	3
Data acquisition modules	2	3	6
Total cost of electronic equipment for interferometer:			241
Total cost of interferometer equipment			**625**

B. Vacuum chambers for each end of the optical interferometer:

Item	Number	Unit cost	Item cost
Vacuum chamber	2	40	80
Ion pump 1000 l/s	2	22	44
Turbopump 1500 l/s	2	25	50
Ion pump 110 l/s	4	10	40
Ti sublimation pump	6	3	18
Residual gas analyzer	4	15	60
Valves 10 inch	4	6	24
Valves 6 inch	4	3	12
Feedthroughs	24	0.5	12
Windows	20	1	20
Bellows	16	2	32
Miscellaneous			40
Total cost of vacuum chamber parts			**432**

C. Vibration isolation

Item	Number	Unit cost	Item cost
Inertial platform for optics	2	50	100
External vibration isolation	2	10	20
Internal vibration isolation	2	10	20
Total cost of vibration isolation parts			**140**

D. Prototyping and test apparatus:

Item	Number	Unit cost	Item cost
Vacuum apparatus			20
Misc. mounting hardware			10
Misc. optics			10
Total cost of prototyping and test apparatus			**40**

E. Miscellaneous materials and supplies	5 years	20/year	**100**
F. Clean room facility			**100**

G. Technician support: mechanical

Assembly & testing of vacuum chambers	2 man-yr.	50	100
Assembly & testing of vibration isolation	2 man-yr.	50	100
Total technician support, mechanical assembly			**200**

H. Technician support: electrical

Design and assy. of locking electronics (NIST)	2 man yr.	80	160
Total technician support, electrical assembly			**160**

I. Engineering design	Scattered light baffle design	**50**

J. Project management

P. Kraushaar $70K/year + 18.4% fringe + 45% indirect + 4% inflation	5 years	70	**651**

SUMMARY OF OPTICAL AND VACUUM EQUIPMENT COSTS

A. Optical interferometer	625
B. Vacuum chambers	432
C. Vibration isolation	140
D. Research apparatus	40
E. Misc. materials and supplies	100
F. Clean room facility	100
G. Technician support: mechanical	200
H. Technician support: electrical	160
I. Engineering design	50
J. Project management	651
TOTAL OPTICAL AND VACUUM EQUIPMENT COSTS	2498

11.2.2 Operating costs - optical system development

11.2.2.1 Colorado State University (All costs in K$)

A. Personnel (in man-months)	Year 1	Year 2	Year 3	Year 4	Year 5	Total	Total cost w/ benefits
1. Senior Personnel							
S. A. Lee	2	2	2	2	2	10	90
W. M. Fairbank, Jr	2	2	2	2	2	10	90
W. Toki	0	0	0	0	0	0	0
2. Postdoctoral (2)	24	24	24	24	24	120	385
3. Graduate student (3)	36	36	36	36	36	180	253

Unit costs:
Senior personnel $7K/mo. + 18.4% fringe + 4% inflation
Postdoctoral $2.5K0/mo. + 18.4% fringe + 4% inflation
Graduate student $1.3K/mo. + 4% inflation

TOTAL PERSONNEL 819

B. Travel							
Man-trips (1 week each)	10	10	20	25	35	100	
Unit cost: $1.2K						**TOTAL TRAVEL**	120
C. Graduate tuition (sem.)	6	6	6	6	6	30	
Unit cost: $1.2K/semester (average)						**TOTAL TUITION**	36
D. Miscellaneous (Xerox, phone, publ., supplies, etc.)	15	15	15	15	15	75	
Unit cost: $15K/year						**TOTAL MISC.**	75

TOTAL DIRECT COSTS	1050
INDIRECT COSTS [45% of (direct-tuition)]	456
TOTAL PROJECT COSTS	1506
(Average yearly cost:	301)

11.2.2.2 JILA/Colorado (All costs in K$)

A. Personnel (in man-months)	Year 1	Year 2	Year 3	Year 4	Year 5	Total	Total cost w/ benefits
1. Senior Personnel J. Hall	3	2	1	1	1	8	85
2. Postdoctoral (1)	12	12	12	12	12	60	255
3. Graduate student (1)	12	12	12	12	12	60	84

Unit costs:

Senior personnel	$10K/mo.+ 4% inflation (fringe included in indirect)
Postdoctoral	$3.3K/mo. + 18.7% fringe + 4% inflation
Graduate student	$1.3K/mo. + 4% inflation

B. Travel Man-trips (1 week each)	6	6	6	6	6	30	
Unit cost: $1.2K						**TOTAL TRAVEL**	**36**
C. Graduate tuition (sem.)	2	2	2	2	2	10	
Unit cost: $1.2K/semester						**TOTAL TUITION**	**12**
D. Miscellaneous (Xerox, phone, publ., supplies, etc.)	20	20	20	20	20	100	
Unit cost: $20K/year						**TOTAL MISC.**	**100**
						TOTAL DIRECT COST	**572**
						INDIRECT COST [49% of (direct-Sr. Pers.) + 150% of Sr. Personnel]	**366**
						TOTAL PROJECT COST	**937**
						(Average yearly cost:	**187)**

Site operations for string and refrigerator	M & S ($K)	EE (mm)	ME (mm)	CS(mm)	ET (mm)	MT (mm)	PM (mm)	Notes
Site modifications								
Building enclosure for optics	$100						0.0	Need requirements
Complete site LCW system	$10		0.5	1.0	1.0	0.5	0.4	Required for power supplies (check w/ Jun Floresca)
Install LCW piping to power supplies	$30						0.0	(check with Rex Trekell)
Site mods subtotal	**$140**	**0.0**	**0.5**	**1.0**	**1.0**	**0.5**	**0.4**	
String construction								
System design activities		2.0	2.0	2.0	2.0	2.0	1.3	System level drawings and documentation efforts
Disassemble string	$10					12.0	1.5	Remove current string from building enclosure
Design & procure magnet stands	$60		1.0				0.1	Three-point mount with stands
Install & align stands	$5					0.5	0.1	
Transform feed can back to end can	$5		2.0			3.0	0.6	End can was modified to support SPR testing
Modify magnets for Upper or Lower bus	$10	1.0	1.0			3.0	0.6	Modify up to three magnets
Install cables and wiring in niche & enclosure	$30					10.0	1.3	
Extended Interconnect	$10		0.5			0.5	0.1	One meter extension in middle of string
Add Pump out to Interconnects	$21		1.0			2.0	0.4	Mod. to Interconnect for beam vacuum pumpout
Pre Installation Magnet QA	$6					2.0	0.3	Survey beam tube, electrical check
Install Six Magnet String	$21					24.0	3.0	M&S Includes interconnect replacement parts
Align Magnet String	$1					1.5	0.2	Assumes host site has survey crew
String construction subtotal	**$179**	**3.0**	**7.5**	**2.0**	**2.0**	**60.5**	**9.4**	
Site modifications & construction total	**$319**	**3.0**	**8.0**	**3.0**	**3.0**	**61.0**	**9.8**	

Refrigerator operations cost	M & S (K)	Time (wks)	Engr (mm)	Cryo techs (mm)	
Single magnet testing (yr. 1)	$84	8.0	1.8	5.5	Includes cooldown, commissioning, and testing 2 magnets
Six magnet string testing (yr. 2)	$175	11.0	2.5	7.6	3 wk n2 + 1 wk cooldown +8 wk initial testing
Six magnet string testing (yr. 4)	$233	14.0	3.2	9.7	3 wk n2 + 1 wk cooldown +2 wk comm.+ 8 wk test
Six magnet string testing (yr. 5)	$233	14.0	3.2	9.7	3 wk n2 + 1 wk cooldown +2 wk comm.+ 8 wk test
Total Refrigerator Operations	**$725**	**47.0**	**10.8**	**32.5**	

Single magnet testing activities	M & S ($K)	EE (mm)	ME (mm)	CS(mm)	ET (mm)	MT (mm)	PM (mm)	Notes
Power supplies							0.0	
Controls & diagnostics		4.0		6.0	3.0		1.6	
Ramp generator	$20	3.0		6.0	3.0		1.5	Need to determine ramp parameters via testing
Develop compensation loops for high ramp rates	$20	2.0			2.0		0.5	Dependent on required ramp parameters
Power supply system commissioning	$20	5.0		6.0	2.0	2.0	1.9	Operate into short circuit & resistive loads
Power supplies subtotal	**$60**	**14.0**	**0.0**	**18.0**	**10.0**	**2.0**	**5.5**	
Quench protection								
Develop quench protection instrumentation	$5	1.0			1.0		0.3	Algorithms must be developed and reviewed
Controls and diagnostics system		2.0		2.0			0.5	System must pass diagnostic tests before permit is issued
Install & check-out HFUs (for two magnets)	$2	1.0			1.0		0.3	Majority of system is installed and operational
Quench protection system commissioning		1.0		2.0	1.0		0.5	Conducted during 2 magnet test
Quench protection subtotal	**$7**	**5.0**	**0.0**	**4.0**	**3.0**	**0.0**	**1.5**	
Controls								
Cryo control valves	$5	0.5	0.5	1.0		1.0	0.4	Notify cryo system of quench condition
Temperature & pressure (calibration costs)	$5	0.5	0.5	0.5	0.5	1.0	0.4	C:Gl, Pt, & KPY transducers
Transient measurements	$60	1.0		1.0	1.0		0.4	Use Tek 11801B with LabViews on SUN
Interface to refrigerator	$5		1.0			1.0	0.3	Obtain permit to energize string
Controls subtotal	**$75**	**2.0**	**2.0**	**2.5**	**1.5**	**3.0**	**1.4**	
Single magnet testing								
Install magnet DCATBD#1	$2				1.0	1.0	0.3	
Complete test stand interface	$5	1.0	2.0	2.0	1.0	2.0	1.0	Complete endcan interface & cable runs
Commission test stand with magnet	$2	0.5		0.5	0.5	0.5	0.3	Need several quenches at various currents & ramp rates
Perform 45 runs as listed in Table 8 (1 day/run)	$2	3.0			1.0	1.0	0.6	Need to factor in labor and materials for cryo
Remove magnet DCATBD#1						1.0	0.1	
Install magnet DCATBD#2	$2				1.0	1.0	0.3	
Commission test stand with magnet	$2	0.5		0.5	0.5	0.5	0.3	Need several quenches at various currents & ramp rates
Perform 45 runs as listed in Table 8 (1 day/run)	$2	3.0			1.0	1.0	0.6	Need to factor in labor and materials for cryo
Remove magnet DCATBD#2						1.0	0.1	
Single magnet testing subtotal	**$17**	**8.0**	**2.0**	**3.0**	**6.0**	**9.0**	**3.5**	
Single magnet integration & testing total	**$159**	**29.0**	**4.0**	**27.5**	**20.5**	**14.0**	**11.9**	

Six magnet integration & test activities	M & S ($K)	EE (mm)	ME (mm)	CS(mm)	ET (mm)	MT (mm)	PM (mm)	Notes
Power supplies (total of three power supplies)							0.0	
Install power supplies	$20		1.0		2.0	2.0	0.6	LCW & AC power listed seperately
Design and install bus work	$30	2.0	2.0		2.0	2.0	1.0	Install 3 power supplies in series configuration
Install ac power for power supplies		1.0	2.0				0.4	Contract work
Controls & diagnostics		4.0		6.0	3.0		1.6	
Ramp generator	$20	3.0		6.0	3.0		1.5	Need to determine ramp parameters via testing
Design compensation loops	$20	4.0			3.0		0.9	Dependent on required ramp parameters
Power supply system commissioning	$20	5.0		6.0	2.0	2.0	1.9	Operate into short circuit & resistive loads
Power supplies subtotal	**$110**	**19.0**	**5.0**	**18.0**	**15.0**	**6.0**	**7.9**	
Quench protection								
Develop quench protection instrumentation	$10	1.0			1.0		0.3	Algorithms must be developed and reviewed
Controls and diagnostics system		1.0		2.0			0.4	System must pass diagnostic tests before permit is issued
Install bypass SCRs	$8	1.0	1.0			1.0	0.4	Need SCR enclosure and heat sink design
Install & check-out HFUs	$6	1.0			1.0		0.3	Majority of system is installed and operational
Quench protection system commissioning		1.0		1.0	1.0		0.4	Conducted during 2 magnet test
Quench protection subtotal	**$24**	**5.0**	**1.0**	**3.0**	**3.0**	**1.0**	**1.6**	
Controls								
Cryo control valves	$20	2.0	2.0	2.0		2.0	1.0	Notify cryo system of quench condition
Recooler operation	$10	1.0	1.0	1.0		1.0	0.5	Closed loop control
Optics interface (TBD)							0.0	
Temperature & pressure	$6	1.0	1.0	1.0	1.0	1.0	0.6	System support for > 100 channels
Transient measurements	$5	1.0		1.0	1.0		0.4	Quench analysis and system "snapshot" capability
Interface to refrigerator			0.5			1.0	0.2	Obtain permit to energize string
Controls subtotal	**$41**	**5.0**	**4.5**	**5.0**	**2.0**	**5.0**	**2.7**	
Total for Six magnet integration & testing	**$175**	**29.0**	**10.5**	**26.0**	**20.0**	**12.0**	**12.2**	

Program cost estimate	M & S ($K)	EE (mm)	ME (mm)	CS(mm)	ET (mm)	MT (mm)	PM (mm)	Notes
Item								
Site mods & string construction	$319	3.0	8.0	3.0	3.0	61.0	9.8	
Total Refrigerator Operations	$725		10.8			32.5		
Single magnet testing & integration	$159	29.0	4.0	27.5	20.5	14.0	11.9	
Six magnet testing & integration	$175	29.0	10.5	26.0	20.0	12.0	12.2	
subtotal	$1,378	61.0	33.3	56.5	43.5	119.5	33.8	
Project management activities								
Miscellaneous supplies (@0.01*labor)	$13							
Procurement							13.2	Manpower-estimate based on M & S
Design review activities		2.5	1.4	2.4	1.8	5.0	1.4	Estimate of 2 man weeks/man year
Travel	$249							Travel estimate of one trip/man month @ $1k/trip
Project management activities subtotal	$262	2.5	1.4	2.4	1.8	5.0	14.7	
Total	$1,640	63.5	34.7	58.9	45.3	124.5	48.5	

Man years effort	29.0	FTE
Manpower rate/man month (used by TNRLC) =	$7,083	
Manpower cost @ $7,083/mm	$2,659	K
15% contingency (M & S + manpower)	$645	K
Project cost estimate, first 5 years	$4,944	K

He Refrigeration Operating Costs, $/week				
Item (notes)	LN Cooldown (6)	Energy Saver (7)	Standby (8)	Full (9)
LN consumption (1)	4,500	2,000	2,500	3,000
GHe consumption (2)	750	1,500	1,500	1,500
Electric Power (3)	1,920	7,763	10,935	14,107
Makeup water (4)	78	314	442	571
Consumption $/wk	7,248	11,577	15,377	19,178
Staff (5) (5a)	941	4,326	4,326	4,326
Grand Total $/wk	8,188	15,904	19,704	23,504
Grand Total $/day	1,170	2,272	2,815	3,358
Grand Total $/month	35,093	68,158	84,445	100,732

Notes.

1. Based on the measured comsumption of the ASST run experience. Includes a modest (ASST like) LN shield provision.
2. Extrapolated to steady state running from the ASST run experience.
3. Based on the connected and spinning compressor and tower motor hp and a $0.053/kWh rate. Inculdes I/A, tower pump and fan.
4. Actual; @ $0.00283/gallon, and 20 gpm (assumed and scaled). Researching flow, chem. (costs to include chem., etc.).
5. Steady state, four man crew (see 5a) @ $16/hr, with an independently applied 47% total load and a 22% shift premium.
5a. The Cooldown has a staff cost of a manweek/wk, w/o premium.
6. Operating the CCWP @ 50 g/s and NO COLD RETURN. For Warmup delete LN cost.
7. One set of compressors secured.
8. One set of compressors fully loaded, one set spinning unloaded.
9. Both compressor sets fully loaded.

11.4 Summary of Project Costs

A. Equipment - optical and vacuum systems	**2498**
$2448K total	
B. Operating costs - optical system development (CSU)	**1506**
Average yearly cost $301K	
C. Operating costs - optical system development (JILA/CU)	**937**
Average yearly cost $187K	
D. Magnet and operating costs (SSCL)	**4944**
(possible site differences)	
TOTAL ESTIMATED PROJECT COST	**9885**

12. FUNDING PLAN

Due to the settlement made between the DOE and the state of Texas concerning the assets of SSCL, our picture of the anticipated funding source has changed since the initiation of the project. The background research and development efforts in laser stabilization, frequency metrology and optical interferometry which make the proposed experiment technically feasible are a result of more than two decades of support from the National Institute of Technology, the National Science Foundation, and the Department of Defense (ONR and AFOSR). Under the current funding climate, it will be unrealistic to expect that there will be significant "new" funding forthcoming from these agencies for the proposed experiment. Therefore, the cost of this experiment will most likely be coming from DOE or other sources. Nevertheless, we believe that a dialogue with these agencies are useful because of the cross-disciplinary nature of the proposed experiment. We plan to solicit funding from DOE, the host laboratory, NSF (~$100 K/yr for individual investigators) and NIST (Precision Measurement Grants, $150 K total).

APPENDIX: COST IMPACTS OF THE FERMILAB SITE OPTION

Two sites have been investigated as possible host laboratories for this experiment, TNRLC or Texas and Fermilab. The risks associated with the TNRLC site have already been discussed in section 8.2 and a crude cost estimate based on using that site was presented in section 11.2. In this section, we will look at the economic impact to the overall project cost of using FNAL as the host laboratory as compared with Texas. It should be noted that this discussion will pertain only to magnet systems costs. The costs associated with the optical interferometer are site independent (except for vibration isolation which may differ from site to site but will be assumed equal here as far as the cost to mitigate.)

Fermilab is an operating accelerator based, high energy physics laboratory with all the necessary infrastructure in place to support this experiment. The original string test of early SSC prototypes dipoles was done at the Fermilab ER string test site. This site has since been modified for use with other magnets but the key resources of power and cryogenics are in place. The present ASST control room trailer and equipment could be moved to FNAL and utilized. The building which would house this experiment would have to be lengthened and enlarged. A very preliminary cost estimate is about $500K to $600K to accomplish this. This increase to the project cost is offset by savings in other areas, most notably, cryogenic operations. This experiment presents a small heat load to the overall cryogenic system used to cool the Tevatron. Therefore, by operating this experiment during scheduled accelerator operations, it becomes a parasitic function (cryogenically) at little or no cost. ($3K/week of operations for LN_2 and He would probably be an over estimate for consumable costs.) At the TNRLC site, refrigerator operation costs for this program would be approximately $1363K for 47 weeks of operation..

Fermilab still has in operation a single magnet test stand that was used to test the ASST magnets after construction (at FNAL) but prior to shipment to the SSCL. There is a desire to do some residual testing on ASST style dipoles at FNAL as part of an on going magnet R&D effort there. The single magnet testing that this experiment requires can be done as part of that testing program. Many of the magnets required for this experiment are of interest to the FNAL magnet R&D testing program. Costs associated with this would be limited to cost of time on the

test stand. The TNRLC based estimate is roughly $900K for this part of the program due to work associated with establishing the single magnet test stands in the string area.

The ER site at FNAL has a power supply that is adequate for the needs of this experiment currently installed and being used to test other magnets. This is an R&D supply can be expected to remain at the ER site. If it can be dedicated to this experiment, then the costs associated with using the ASST type power supplies are eliminated. (approximately $500K based on TNRLC estimate) ER also has adequate low conductivity water (LCW) available. If the three ASST type Dynapower DC supplies are required, then an approximate $30K upgrade to the AC power to ER would have to be made.

For the quench protection and power supply ramp control, the QPM and CECAR systems, respectively, used at the ASST are the next generation of the TECAR and QPM systems used at FNAL. The equipment assets of the ASST could be directly applied to this experiment although the sophistication of the QPM is not required for this experiment. As described in the magnet section, simple analog quench detection circuits (QDC's) can be used to provide the required detection. These were developed at FNAL and a second generation of that circuit was to be used as a back up at the ASST. The parts exist to build ten of these modules but the assembly was never done. One advantage to using the more sophisticated QPM from the ASST in this experiment is that it provides FNAL with a test bed for future quench protection development efforts.

Personnel costs are folded into the TNRLC estimates and by eliminating certain total costs from that estimate, an under estimation may result on personnel. The collaboration would expect to have an on site core group dedicated to this experiment through out the five year period. This group would be composed of the Project Manager (Scientist), an Engineering Physicist, a Lead Technician (Senior Engineering Associate) and a technician. Additional technical and engineering support for the various systems would be drawn from the FNAL on an as needed basis to support the various magnet related systems. During data taking periods, this core group in addition to collaboration members would constitute the operations staff.

The option of conducting this experiment at FNAL provides some interesting alternatives for risk and project cost reductions. The area where DOE must make a decision is on the transfer of ASST related assets. It is therefore important that a decision on the host laboratory for this experiment be made very early to allow a more detailed site specific cost estimate to be made and to allow for the transfer of key equipment before that equipment is lost to this experiment.

Summary of Cost Savings at FNAL

The following summarizes the possible savings of selecting FNAL as the host laboratory. These estimates are based on sharing the resources and combining testing need of this experiment with ongoing programs at FNAL. Preliminary and informal discussions with FNAL staff indicate that this is possible.

1.	**Facilities modifications at ER** (Lengthen and enlarge site for string)	**-600 K**
2.	**Cryogenic operations** (Based on 47 weeks of operation: FNAL M & S estimate, 141K, no labor TNRLC M & S plus labor 1363 K)	**1222 K**
3.	**Power supply system** (Assumes use of present setup at ER)	**500 K**
4.	**Single magnet testing program** (To define operating envelope. Assumes EOI testing is part of FNAL planned testing program)	**900 K**
	TOTAL PROJECT SAVINGS AT FNAL	**2022 K**